

TWO-DIMENSIONAL AXIAL-AZIMUTHAL (Z - θ) SIMULATION OF
CROSS-FIELD ELECTRON TRANSPORT IN A HALL THRUSTER
PLASMA DISCHARGE

A DISSERTATION
SUBMITTED TO THE DEPARTMENT OF MECHANICAL
ENGINEERING
AND THE COMMITTEE ON GRADUATE STUDIES
OF STANFORD UNIVERSITY
IN PARTIAL FULFILLMENT OF THE REQUIREMENTS
FOR THE DEGREE OF
DOCTOR OF PHILOSOPHY

Cheryl Meilin Lam
August 2015

© 2015 by Cheryl Meilin Lam. All Rights Reserved.

Re-distributed by Stanford University under license with the author.



This work is licensed under a Creative Commons Attribution-Noncommercial 3.0 United States License.

<http://creativecommons.org/licenses/by-nc/3.0/us/>

This dissertation is online at: <http://purl.stanford.edu/zx064tb7256>

I certify that I have read this dissertation and that, in my opinion, it is fully adequate in scope and quality as a dissertation for the degree of Doctor of Philosophy.

Mark Cappelli, Primary Adviser

I certify that I have read this dissertation and that, in my opinion, it is fully adequate in scope and quality as a dissertation for the degree of Doctor of Philosophy.

Matthias Ihme

I certify that I have read this dissertation and that, in my opinion, it is fully adequate in scope and quality as a dissertation for the degree of Doctor of Philosophy.

Javier Urzay Lobo

Approved for the Stanford University Committee on Graduate Studies.

Patricia J. Gumport, Vice Provost for Graduate Education

This signature page was generated electronically upon submission of this dissertation in electronic format. An original signed hard copy of the signature page is on file in University Archives.

Abstract

The Hall thruster (or Hall effect thruster) is an electric propulsion device used for space flight applications. Despite its use as a deployed production technology, much of the underlying plasma physics which governs thruster behavior and performance is not well understood. Specifically, laboratory experiments indicate an anomalously high electron mobility in the direction perpendicular to the magnetic field, which exceeds that predicted by classical theory. Predicting this so-called anomalous electron transport remains a key research challenge. One possible mechanism for the generation of super-classical electron transport is the interaction of correlated quasi-coherent fluctuations in the plasma properties. Instabilities in the plasma can lead to quasi-coherent wave fluctuations in the electric potential, electron number density, and electron velocities; if these fluctuations are appropriately correlated, they can serve to either enhance or reduce electron transport across the magnetic field. In this work, we use numerical simulations as a tool to characterize axial and azimuthal fluctuations in the plasma discharge properties and study their impact on cross-field electron transport.

We employ a two-dimensional axial-azimuthal (z - θ) model to simulate an annular Hall thruster discharge. We use a hybrid fluid-Particle-In-Cell approach in which the positive ion (Xe^+) and neutral (Xe) species are modeled using a Particle-In-Cell (PIC) treatment and the electrons are modeled as a fluid continuum. The ion and neutral species are modeled as discrete collisionless superparticles; due to their large mass and consequently large Larmor radius, we neglect the magnetic field effect on the ions. For the electron fluid, we include the first three moments of the Boltzmann equation to obtain 2D continuity and momentum equations, using the drift-diffusion approximation, and a quasi-1D energy equation. The

PIC and fluid treatments are coupled by assuming space charge neutrality, or quasineutrality, between the ions and electrons.

We chose a simulated thruster model geometry and operating conditions to enable comparisons to experimental measurements of the Stanford Hall Thruster (SHT) laboratory discharge. The simulated thruster channel is 8 cm long, with an outer diameter of 9.4 cm; we include the full azimuth throughout the simulated domain, which includes the entire channel length and the near-plume. Using a non-uniform spatial resolution of 3 mm - 10 mm and maximum time step of 10 ns, we can achieve a simulated time of extent on the order of milliseconds, using a single PC processor core for a wall clock time of several days.

We present results for a representative simulated low voltage operating condition. Simulated plasma properties are compared to experimental measurements of the plasma properties and the effective electron mobility. We further analyze the simulated data to characterize predicted axial and azimuthal fluctuations in the electric potential, electron number density, and electron velocities. We consider the simulated wave fluctuations in the context of linearized fluid theory models for specific dispersive propagation modes, as we attempt to characterize their impact on the effective axial electron transport for various axial regions within the thruster discharge.

For the simulated time and spatial scales presented here, correlated fluctuations appear to enhance electron transport in some regions of the discharge and inhibit electron transport in others. In the mid-channel region, where we believe gradients in the electron density and magnetic field may contribute to gradient-driven waves, we observe enhancement of the electron mobility beyond classical mobility values. Near the channel exit plane, however, we observe a distinct electron transport barrier, similar to that observed in experimental measurements. Just upstream of the channel exit plane, correlated fluctuations in the electron number density and the axial electron velocity appear to generate negative current which opposes the positive bulk discharge current; in this region, we believe the axial shear in the electron velocity may play a role in disrupting fluctuations and reducing electron transport. In both cases, it is clear that simulated wave fluctuations impact axial electron transport.

Even in regions of observed transport enhancement, however, the simulated fluctuation-driven transport does not fully account for the experimentally-observed super-classical mobility. We believe that an additional transport mechanism – perhaps electron wall scattering or higher frequency, shorter wavelength fluctuations – is necessary to account for the experimentally-observed electron mobility. Towards this end, we present results for additional simulations which include an artificially enhanced electron collision frequency; these simulations show improved agreement with experimental results and confirm the need to include additional physical mechanisms for anomalous electron transport. Finally, suggestions for future work are included.

Acknowledgements

A great number of people have supported, encouraged, and helped me make it through this (hopefully) final academic accomplishment. I attempt to briefly mention some of them here and apologize in advance to those I have forgotten to include.

I will start by thanking my adviser Mark Cappelli. Mark is my doctoral research adviser; however, during my time at (and even in between) Stanford, he has been much more than that. I first met Mark when I was an impressionable 18-year-old undeclared freshman undergrad; over the many years I have known Mark, I have learned a great deal from him – not just about research and academics, but also about many of the other important things in life. Mark has been a key figure in my academic and professional development, offering guidance over the years, and leading by example, both in his intellectual pursuits and, more generally, in life.

The next person I must thank is Eduardo Fernandez – without whom the work presented here would not have existed. I am deeply indebted to Eduardo – for his research contributions, including the original z - θ code upon which this work is based, and for his investment of time and attention during my doctoral study. For much of my PhD study, Eduardo has served as a second research adviser – providing guidance, stimulating intellectual discussion, detailed and critical reviews of my work, and challenging, thoughtful questions. On top of that, Eduardo is incredibly kind, generous, and gracious, and I feel fortunate to have gotten the opportunity to work with and learn from him.

I would like to thank the members of my reading committee, Prof. Matthias Ihme and Dr. Javier Urzay, for their time and valuable input during this process, as well as the other members of my defense committee, Profs. Reggie Mitchell and Sigrid Close. I would also like to mention the late Bill Reynolds – who, along with my father, was responsible

for piquing my interest in engineering and, more specifically, the ME Thermosciences at Stanford; Bill is also the one who first introduced me to Mark – so, he indirectly help put me on the path towards this PhD. I mention my father who, after cramming in all he could learn during his 9 months in the MS ME program at Stanford, has shared with me his enduring love for the university and the ME department especially. As I was growing up and getting my undergraduate degree at Stanford, my dad spoke so reverently of the Stanford ME (then Building 500) PhD; I never imagined that I would end up pursuing such a thing – however, it seems that his influence may have been stronger than either of us suspected, and I would like to think I have made him proud.

Thanks to all of the SPPL (Cappelli lab) family. I am grateful to Nicolas Gascon – for his guidance, expertise, and friendship over the years and his support and wisdom especially during this last stretch of the PhD process. Special thanks also to: Eunsun Cha – who has been my dissertation and simulation buddy; the SPPL simulation crew – Michelle Scharfe, Aaron Knoll, and Chris Young; Sasha – for getting me through quals; and many others over the years – Scott, Nathan, David, Flavio, Andrew, Ben (who set up our awesome workhorse simulation computer!) and everyone else.

I would like to to thank and acknowledge Sandia National Laboratories for their funding support. Also, special thanks to my manager Rena Zurn and others who have helped in various ways at various stages of the PhD process: Scott Hutchinson, Elaine Yang, Gary Templet, Dan Fonte, Bill Ballard, Marty Pilch, Rich Schiek, and Mary Gonazles. Thanks also to former Sandians (and fellow PhD women): Teresa Ko, Genetha Gray, and Monica Martinez-Canales.

Thanks to my family – my nurturing parents, Dr. sister, and extended family (including Poulsens and Zwiebels) – especially my cousin Amanda who ended up in grad school at the same time! Thanks to my incredible friends, who are like my second family, for your concern, support and encouragement. Speical mentions: my bestie Mariel (could not have done this without you!); , the taskmaster Hoop; the historian Alex Orquiza, my one PhD buddy from my high school days; my friend-therapist and life coach Naomi; and my closest friends and cheerleaders – Ray, Elia, Peter, Crystal, Sha, Amanda, Helen, Walter, Marilyn, Andy, Sprog, Matteo, Pam, and David. Thanks also to my professional support team: Drs. Kathy Lee and Tamara Cagney. Finally, my love and thanks to Adam – for his

most valiant efforts to keep me sane, motivated, happy and well loved even during the most crazy-making times.

Contents

Abstract	iv
Acknowledgements	vii
1 Introduction	1
1.1 Hall Thruster	1
1.2 Motivation	2
1.3 Research Objective	4
2 Hall Thruster Simulations	5
2.1 Purpose	5
2.2 Challenges	6
2.3 Simulation Approaches	7
2.4 Relevant Prior Work	8
2.4.1 2D Radial-Axial (r - z)	8
2.4.2 2D Axial-Azimuthal (z - θ)	9
2.4.3 3D (x - y - z or r - z - θ)	10
2.5 Relevance of Described Research	11
3 Hybrid Fluid-PIC Axial-Azimuthal (z-θ) Model	13
3.1 Model Geometry and Computational Domain	13
3.2 Key Assumptions	17
3.3 Neutral Gas	18
3.4 Ions	20

3.5	Electron Fluid	23
3.5.1	Continuity (Species and Current Conservation)	24
3.5.2	Momentum Conservation	25
3.5.3	Energy Conservation	28
3.5.4	System Closure and Solution for Fluid Equations	32
3.5.4.1	System of Governing Equations	32
3.5.4.2	Electric Potential	33
3.5.4.3	Reduced System of Equations for Numerical Solution	33
3.5.5	Summary of Fluid Equations for Numerical Solution	35
4	Numerical Solution Method	38
4.1	Hybrid Fluid-PIC Approach	38
4.1.1	Particle-In-Cell Approach	38
4.1.2	Coupled Fluid-PIC Treatment	44
4.2	Simulation Process (Numerical Solution Algorithm)	45
4.2.1	Particle Motion	45
4.2.2	Ionization	47
4.2.3	Neutral Injection	48
4.2.4	PIC Interpolation and Smoothing	49
4.2.5	Time Advancement of Electron Temperature	50
4.2.6	Iterative Solution for Electric Potential	52
4.3	Numerical Considerations	55
4.3.1	Time Step	55
4.3.2	Spatial Resolution	57
4.3.3	Number of Simulated Particles (Validity of PIC Approach)	57
4.3.4	Computational Expense	59
4.4	Boundary Conditions	60
5	Simulation Results	62
5.1	Simulation Conditions	62
5.1.1	Thruster Operating Condition	62
5.1.2	Simulation Parameters	63

5.1.3	Initial Conditions	65
5.2	Plasma Properties	65
5.2.1	Initial Transient Behavior	65
5.2.2	Quasi-steady Operation	70
5.3	Discharge Current	74
5.4	Electron Transport	82
6	Discussion	88
6.1	Fluctuation-Induced Transport	88
6.1.1	Premise	88
6.1.2	Simulated Waves	90
6.1.2.1	Azimuthal (θ) Grid Refinement	91
6.1.2.2	Time Step Sampling (Undersampling of Simulated Time)	91
6.2	Analysis of Simulated Waves	95
6.2.1	Near Anode ($z \leq 0.01$ m)	98
6.2.2	Mid-channel ($0.02 \text{ m} \leq z \leq 0.06 \text{ m}$)	100
6.2.3	Near Exit Plane ($0.07 \text{ m} \leq z \leq 0.08 \text{ m}$)	102
6.2.4	Outside Channel ($z > 0.08 \text{ m}$)	107
6.3	Summary	109
7	Enhanced Collision Frequency (Additional Results)	111
7.1	Electron Mobility Enhancement due to Wall Interactions	111
7.2	Enhanced Collision Frequency	112
7.2.1	Model Implementation	113
7.2.2	Effect of Collision Frequency Enhancement (v_{add})	113
7.3	Simulation Results for $v_{add} = 10^7 \text{ s}^{-1}$	116
7.3.1	Simulation Conditions	117
7.3.2	Plasma Properties	117
7.3.2.1	Initial Transient Behavior	117
7.3.2.2	Quasi-steady Operation	122
7.3.3	Discharge Current	126
7.3.4	Electron Transport	129

7.4	Summary	133
8	Conclusion	136
8.1	Research Summary	136
8.2	Suggestions for Future Work	137
A	Particle Velocity Distribution Sampling	139
A.1	Implementation	139
A.1.1	Distribution Inversion (Sampling)	139
A.1.2	Projection onto z - θ Plane	140
A.2	Velocity Distributions	141
A.2.1	Initial Conditions	141
A.2.2	Neutral Injection	143
B	Analysis of Dispersive Wave Behavior	144
B.1	Analysis of Simulated Data	145
B.2	Comparison to Linearized Fluid Theory	147
B.2.1	Linearized Model Approach	147
B.2.2	Frias Model ($0.02 \text{ m} \leq z \leq 0.06 \text{ m}$)	149
B.2.3	Thomas Model ($0.07 \text{ m} \leq z \leq 0.08 \text{ m}$)	149
B.3	Summary	153
	Bibliography	154

List of Tables

5.1	Simulated operating condition	63
5.2	Summary of simulation parameters	64
7.1	Simulated operating condition for enhanced collision frequency simulation	117
7.2	Summary of simulation parameters for enhanced collision frequency simulation	118
B.1	Summary of relevant plasma property values at $z \simeq 0.04$ m	150
B.2	Summary of dispersive wave modes predicted by Frias model for $-50 \text{ m}^{-1} \leq k_{\theta}/2\pi \leq 50 \text{ m}^{-1}$	150
B.3	Summary of relevant plasma property values at $z \simeq 0.078$ m	151
B.4	Summary of dispersive wave modes predicted by Thomas model for $-50 \text{ m}^{-1} \leq k_{\theta}/2\pi \leq 50 \text{ m}^{-1}$	151

List of Figures

1.1	Schematic of coaxial (annular channel) Hall thruster. Image reproduced from Thomas (2006).	2
3.1	Schematic of the Stanford Hall Thruster (SHT) laboratory discharge geometry.	14
3.2	2D axial-azimuthal (z - θ) computational domain.	15
3.3	Axial variation of simulated and experimentally-measured magnetic field for Stanford Hall Thruster (SHT). Laboratory measurements of the total magnetic field strength and radial magnetic field were taken at the radial midpoint of the SHT channel $r_{mid} = 4.1$ cm.	16
4.1	Generalized illustration of PIC interpolation.	39
4.2	Simulation process flowchart.	46
4.3	Typical spatial resolution.	58
5.1	Electron temperature $T_e(z)$ at various times t	66
5.2	Electric potential $\phi(z)$ at various times t . (Shown relative to experimentally-measured potential $\phi(z = 0.12) = 30V$.)	66
5.3	Axial electric field, axial ion velocity, neutral number density, and axial neutral velocity at various times t	67
5.4	Electron number density profile and time history, shown on logarithmic scale.	69
5.5	Time-averaged electric potential, electron temperature, axial ion velocity and axial neutral velocity profiles, compared with experimentally-measured values.	71

5.6	Time-averaged neutral number density profile $\bar{n}_n(z)$ compared with experimentally-measured values.	72
5.7	Time-averaged electron number density profile $\bar{n}_e(z)$ compared with experimentally-measured values.	72
5.8	Fluctuating nature of electron number density during quasi-steady-state operation.	74
5.9	Discharge current $I_D(z)$ at various times t	76
5.10	Time history of discharge current $I_D(t)$ at axial location $z = 0.078$ m (just upstream of the exit plane).	77
5.11	Comparison of time-averaged ion and electron current contributions to total discharge current.	78
5.12	Time history of ion and electron current contributions to total discharge current during quasi-steady operation ($t \geq 1200 \mu\text{s}$).	78
5.13	Time snapshot of ion and electron current contributions to total discharge current.	79
5.14	Comparison of axial current conservation with axial grid refinement.	81
5.15	Time-averaged simulated axial electron mobility $\bar{\mu}(z)$ compared to experimentally-measured values. Simulated classical mobility terms $\bar{\mu}_{\text{classical}}$ and $\bar{\mu}_{\perp}$ are shown for reference.	85
5.16	Comparison of time-averaged ion, electron, and anomalous electron current contributions to total discharge current.	85
5.17	Time snapshot of ion, electron, and anomalous electron current contributions to total discharge current.	87
6.1	Time history of electron number density $n_e(t)$ and axial electron velocity $u_{ez}(t)$, shown for $t = 1600 \mu\text{s} - 1800 \mu\text{s}$ at $z \simeq 0.043$ m.	89
6.2	Representative time snapshots of axial and azimuthal variation in plasma properties.	92
6.3	Comparison of representative time snapshots of electron number density $n_e(z, \theta)$ and axial electron velocity $u_{ez}(z, \theta)$ with azimuthal grid refinement.	93

6.4	Time snapshot of anomalous contribution to electron current with azimuthal grid refinement.	94
6.5	Comparison of time-averaged simulated axial electron mobility $\bar{\mu}(z)$ with azimuthal grid refinement. Experimentally-measured values and simulated classical mobility terms $\bar{\mu}_{classical}$ and $\bar{\mu}_{\perp}$ are shown for reference.	94
6.6	Axial variation of axial and azimuthal wave characteristics for axial electron velocity u_{ez} . Analysis performed for $t = 1600 \mu s - 1800 \mu s$ with $\Delta\theta = 2\pi/100$, sampled at $T_{samp} = 1 \mu s$ ($f_{max} = \frac{1}{2}f_{Nyq} = 250$ kHz).	96
6.7	Axial streak plots at azimuthal location $\theta = 0$, shown for time duration $t = 1600 \mu s - 1800 \mu s$ with $\Delta\theta = 2\pi/100$	97
6.8	Azimuthal streak plots at axial location $z \simeq 0.005$ m (near anode), shown for time duration $t = 1600 \mu s - 1800 \mu s$ with $\Delta\theta = 2\pi/100$	99
6.9	Azimuthal streak plot of axial electron velocity u_{ez} at axial location $z \simeq 0.04$ m (mid-channel), shown for time duration $t = 1600 \mu s - 1800 \mu s$ with $\Delta\theta = 2\pi/100$	101
6.10	Simulated dispersive wave propagation at $z \simeq 0.04$ m. Analysis performed for $t = 1600 \mu s - 1800 \mu s$ with $\Delta\theta = 2\pi/100$, sampled at $T_{samp} = 1 \mu s$ ($f_{max} = \frac{1}{2}f_{Nyq} = 250$ kHz).	101
6.11	Simulated dispersive wave propagation at $z \simeq 0.079$ m. Analysis performed for $t = 1600 \mu s - 1800 \mu s$ with $\Delta\theta = 2\pi/100$, sampled at $T_{samp} = 1 \mu s$ ($f_{max} = \frac{1}{2}f_{Nyq} = 250$ kHz).	103
6.12	Simulated dispersive wave propagation at $z \simeq 0.079$ m. Analysis performed for $t = 1600 \mu s - 1602 \mu s$ with $\Delta\theta = 2\pi/50$, sampled at $T_{samp} = 10$ ns ($f_{max} = \frac{1}{2}f_{Nyq} = 25$ MHz).	103
6.13	Azimuthal streak plots of axial electron velocity u_{ez} at axial location $z = 0.078$ m (just upstream of exit plane), shown for various time durations with $\Delta\theta = 2\pi/100$	104
6.14	Effect of axial shear on anomalous electron transport. Axial profiles have been time averaged over the interval $t = 1600 \mu s - 1800$ for simulation with $\Delta\theta = 2\pi/100$	105

6.15	Azimuthal streak plots of axial electron velocity u_{ez} at axial location $z \simeq 0.10$ m (outside channel), shown for various time durations with $\Delta\theta = 2\pi/100$.	108
7.1	Comparison of simulation results for various values $v_{add} = 10^6 \text{ s}^{-1} - 10^8 \text{ s}^{-1}$.	115
7.2	Electron temperature $T_e(z)$ at various times t .	119
7.3	Electric potential $\phi(z)$ at various times t . (Shown relative to experimentally-measured potential $\phi(z = 0.12) = 30\text{V}$.)	119
7.4	Axial electric field, axial ion velocity, neutral number density, and axial neutral velocity at various times t .	120
7.5	Electron number density profile and time history, shown on logarithmic scale.	121
7.6	Time-averaged electric potential, electron temperature, axial ion velocity and axial neutral velocity profiles, compared with experimentally-measured values.	123
7.7	Time-averaged neutral number density profile $\bar{n}_n(z)$ compared with experimentally-measured values.	124
7.8	Time-averaged electron number density profile $\bar{n}_e(z)$ compared with experimentally-measured values.	124
7.9	Fluctuating nature of electron number density during quasi-steady-state operation.	126
7.10	Time history of discharge current $I_D(t)$ at axial location $z = 0.078$ m (just upstream of the exit plane).	127
7.11	Comparison of time-averaged ion and electron current contributions to total discharge current.	128
7.12	Time history of ion and electron current contributions to total discharge current during quasi-steady operation ($t \geq 500 \mu\text{s}$).	128
7.13	Comparison of representative time snapshots of electron number density $n_e(z, \theta)$ and axial electron velocity $u_{ez}(z, \theta)$ with azimuthal grid refinement.	130
7.14	Comparison of time-averaged ion, electron, and anomalous electron current contributions to total discharge current.	131
7.15	Time snapshot of ion, electron, and anomalous electron current contributions to total discharge current.	131

7.16	Time-averaged simulated axial electron mobility $\bar{\mu}(z)$ compared to experimentally-measured values. Simulated classical mobility terms $\bar{\mu}_{classical}$ and $\bar{\mu}_{\perp}$ are shown for reference.	132
7.17	Comparison of simulated wave structure in axial electron velocity $u_{ez}(z, \theta)$, shown for grid with 40 points in $z \times 100$ points in θ	134
7.18	Comparison of time-averaged simulated axial electron mobility $\bar{\mu}(z)$. Experimentally-measured values and simulated classical mobility terms $\bar{\mu}_{classical}$ and $\bar{\mu}_{\perp}$ are shown for reference.	134
A.1	Velocity projection in r - θ plane.	140
A.2	Sampled velocity distributions for ion particle initial conditions.	142
A.3	Sampled velocity distributions for neutral particle initial conditions.	142
A.4	Sampled velocity distribution functions for injected neutral particles.	143
B.1	Dispersion map (c) is assembled from individual probe pair analyses (shown in a and b) at axial locations z	146

Chapter 1

Introduction

1.1 Hall Thruster

The Hall thruster is an electric propulsion device developed for space flight (spacecraft) applications, which has demonstrated high thrust efficiencies. Deployed as a production technology for satellite station-keeping since the 1970s and late-1990s, by Russia and the U.S., respectively (Choueiri, 2004; Goebel and Katz, 2008), it is particularly useful for high specific impulse (i.e., high thrust to propellant mass consumption ratio) applications and high-efficiency (i.e., high rocket jet propulsive power to electrical power consumption ratio) low-thrust operations. Today, research continues towards design optimization and performance enhancements; topics of present interest include improved thrust efficiency, prevention and mitigation of lifetime-limiting erosion effects, and investigations into alternative propellants.

Figure 1.1 is a three-dimensional (3D) schematic of a typical stationary plasma thruster (SPT) variant Hall thruster. The device generates thrust by accelerating heavy (positively-charged) ionized particles through an imposed electric potential. A typical Hall thruster geometry is comprised of an annular channel with an imposed primarily-radial magnetic field, created by electromagnets, and an axial electric field, created by an anode located at the base of the channel and an external cathode. The imposed magnetic and electric fields induce an azimuthal Hall current (the effect for which the thruster is named), which traps electrons creating a high-collisionality (high-ionization) zone and strong electric field just

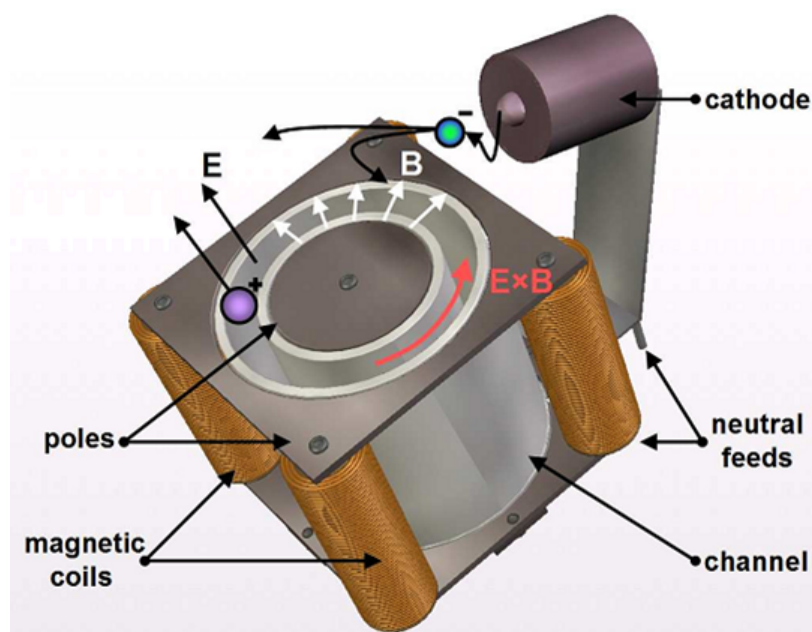


Figure 1.1: Schematic of coaxial (annular channel) Hall thruster. Image reproduced from Thomas (2006).

inside the thruster channel near the exit plane of the thruster. Heavy neutral gas particles (e.g., Xe) are introduced at the anode; as they move through the channel, these neutral particles are ionized by collisions with electrons, particularly in the high electron density region, or high-ionization zone, near the exit plane. The ionized particles are then accelerated across the electric potential, by the axial electric field, until they are ejected from the thruster channel; the ejected mass of the ionized particles, which are moving at high velocity (in the axial direction) due to their acceleration by the axial electric field, results in a net thrust, i.e., rocket propulsion.

1.2 Motivation

Although the Hall thruster is a deployed production technology, much of the underlying plasma physics which governs particle interactions, electron transport, and the ion acceleration process is not well understood. The study of Hall thruster discharges continues to be

an active research topic, and numerical simulations play an important role in ongoing research in this field. Numerical models of the Hall thruster plasma discharge enable a more detailed understanding of fundamental plasma physics, including particle interactions and certain experimentally-observed macro-scale phenomena which are not well described by classical theory. Specific phenomena of interest include electron transport and the semi-random plasma density and current fluctuations which can contribute to enhanced electron transport. Numerical simulations also provide a further means for investigating design improvements and varied operational conditions; such computational experiments serve as an alternative to physical laboratory experiments for predicting and optimizing thruster design and operation.

There is a significant body of existing work focused on Hall thruster simulations, which will be discussed in Chap. 2. One of the remaining challenges in simulating a Hall thruster discharge is accurately characterizing and predicting the so-called anomalous electron transport. The possibility of anomalously high electron mobility across the magnetic field has been experimentally documented since the early years of Hall thruster development (Janes and Lowder, 1966; Meezan et al., 2001). The mechanism leading to this anomalous mobility remains as one of the key challenges in Hall thruster research. A lack of understanding about what generates anomalous mobility in some regions of the flow, while the mobility is very near classical in other regions, has curtailed the usefulness of certain simulations, particularly those that do not resolve the azimuthal (θ) direction (Fernandez et al., 1998; Fife, 1999; Hagelaar et al., 2002). Some theories attribute the anomalously high cross-field electron mobility to quasi-coherent fluctuations resulting from instabilities within the plasma (Janes and Lowder, 1966; Fife, 1999). There is also recent experimental evidence of coherent azimuthally-propagating fluctuations which may contribute to the observed enhanced cross-field transport (Meezan et al., 2001; Knoll, 2010; Ellison et al., 2012). Numerical simulations, particularly those that resolve the azimuthal direction, provide a useful complement to laboratory experiments in understanding how such fluctuations may be related to electron transport and mobility.

1.3 Research Objective

The objective of our research is to use a numerical model to predict and characterize azimuthal fluctuations in a Hall thruster discharge and study the impact of these fluctuations on the electron transport process. Using numerical simulations to resolve the azimuthal electron dynamics, we focus on understanding the role played by fluctuations, particularly those that propagate with components perpendicular to both the applied electric (\mathbf{E}) and magnetic (\mathbf{B}) fields. Where possible, we compare the simulated fluctuations with experimentally-observed phenomena. By analyzing the various physical mechanisms that contribute to the simulated electron transport, we can estimate the effect of certain azimuthal fluctuations on the bulk electron transport.

Chapter 2

Hall Thruster Simulations

In this chapter, we discuss the motivation for continued research and development of improved Hall thruster simulations. We highlight the remaining challenges, in both characterizing the relevant physics and implementing robust computationally-efficient simulations. We summarize relevant prior research efforts in the field and discuss the relevance of the work described in this dissertation.

2.1 Purpose

The purpose of numerical study, i.e., simulations, of Hall thrusters is two-fold.

First, we can use simulations to predict thruster performance and operational behavior under varied operating conditions. Numerical simulations can be used to predict the effect of specific design changes or design optimizations, informing and complementing laboratory experiments; an example is the recent use of numerical simulations to investigate the efficacy of novel alternative propellant fuels (Cha et al., 2009). Simulations have been used to predict the performance, e.g., power, thrust, and efficiency, of various thruster configurations (e.g., Fife, 1999; Bouchoule et al., 2004; Parra et al., 2006; Scharfe et al., 2008), and study practical phenomena, such as predicted thruster lifetime as limited by erosion effects (Sommier et al., 2007).

Second, and more broadly, numerical simulations can be used to perform computational experiments which supplement laboratory experiments. Numerical simulations can

provide a more detailed description and investigation of underlying physical processes in the plasma discharge. While certain physical phenomena, especially at small spatial scales and in certain regions of the thruster discharge, can be difficult to characterize or measure experimentally, simulations provide a wealth of computational data and can be easily adjusted to provide additional detail, such as increased time or spatial resolution, as needed. In a manner analogous to laboratory experiments, we can use numerical simulations to test a hypothesis and measure the effect of simulated conditions on specific physical processes.

2.2 Challenges

There are a number of challenges in developing and performing robust predictive simulations of a Hall thruster plasma.

The primary challenge in developing an accurate Hall thruster model is adequately describing the underlying non-linear coupled physics which governs the plasma discharge. There is a complicated interaction between the magnetic field, the electric fields, and a fluctuating plasma comprised of high-velocity ions and electrons. The plasma behavior can vary significantly between different regions of the thruster, and capturing the transient behavior requires resolving and predicting oscillations in both space and time. There are a number of simultaneous physical processes (some of which cannot be well-characterized microscopically or experimentally) that must be adequately modeled. In many cases, we resort to macro-scale and sometimes empirically-derived models to represent phenomena which cannot otherwise be efficiently or effectively modeled; examples include ionization and wall interactions (e.g., reflections or conductivity at the thruster channel walls). A particular challenge, already mentioned in Chap. 1, is predicting the cross-field electron transport, i.e., the electron transport in the direction perpendicular to the magnetic field; various mobility models have been employed to account for this effect (Fife, 1999; Hagelaar et al., 2002; Barral et al., 2003; Scharfe, 2009; Cha et al., 2015). In all cases, we make certain simplifying assumptions in formulating the numerical model. The key is to include the necessary physics for modeling the phenomena of interest, accounting for neglected effects or approximations as needed and maintaining an awareness of the model's strengths and deficiencies.

The practical, and sometimes limiting, constraint in performing Hall thruster simulations is the computational expense. While continuing advances in computing power and parallel architectures have enabled faster, larger simulations, there is still some practical limit to the computational expense, which correspondingly limits the scope of calculations in either time extent, spatial resolution, or detail in the modeling approach. Based on the simulation objectives, one must make judicious choices in the modeling approach and simulation parameters, e.g., time and spatial resolution, accordingly.

2.3 Simulation Approaches

There are three distinct simulation approaches in common use for Hall thruster and, more generally, plasma simulations. In this section, we will briefly describe each approach and highlight their respective key assumptions, advantages and challenges.

The first approach is the kinetic, or particle simulation, approach. The premise is that all relevant species in the plasma, or ionized gas, discharge are modeled as discrete particles. The particle motion is typically governed by the electric and magnetic fields, and there are various means of resolving the particles' motion more or less finely (e.g., resolving the detailed electron gyromotion versus tracking only the guiding center motion). Since modeling each physical particle in even a low-density plasma would be extremely computationally expensive, some type of mass or density weighting is typically used; a single superparticle, or macroparticle, is used to represent a larger collection of particles (Buneman, 1959; Dawson, 1962). To further reduce computational expense, the Particle-In-Cell (PIC) method was developed (Dawson, 1983; Birdsall and Langdon, 2005). Instead of simulating and calculating all forces and particle interactions using a pair-wise or particle-by-particle approach, under the PIC treatment, certain system properties and interactions, e.g., forces, are evaluated only at a limited set of grid points, which greatly reduces the computational expense. We will describe the PIC approach in greater detail in Sect. 4.1.1. Even with the PIC method, kinetic simulations, especially in three dimensions (3D), can be extremely computationally expensive.

An alternative to the kinetic approach is the fluid continuum treatment. As in computational fluid dynamics, this approach requires that the plasma be sufficiently collisional

for the continuum approximation to be valid. The fluid treatment is further predicated upon the assumption of a Maxwellian distribution, or local thermal equilibrium, for each of the modeled species. The fluid equations are typically derived by taking moments of the Boltzmann equation. Fluid simulations can be less computationally expensive than kinetic simulations; however, the computational expense is driven by the time and spatial resolution of the simulation and the efficiency of the solution method.

The final approach is the so-called hybrid fluid-PIC approach. Under the hybrid treatment, some portion of the plasma is modeled by a fluid continuum treatment, while the rest is modeled using a kinetic PIC treatment. Due to their small mass and consequently faster timescales (which enable more rapid equilibration to a Maxwellian state), the electron species are often modeled using the fluid treatment. Depending on the simulation objectives, the fluid treatment may not be a valid representation for the heavy ion or neutral species; instead, the PIC approach is used for these remaining species. The computational expense for the hybrid approach is typically greater than that for a comparable fully fluid treatment, but less than that for a fully kinetic PIC approach.

2.4 Relevant Prior Work

There exists a significant body of prior work focused on numerical simulations of Hall thruster discharges. Early simulations (e.g., Lentz, 1990), were performed in one dimension (1D), typically in the axial (z) direction, under limited computational resources; since then, the range of Hall thruster simulations has proliferated, with varied simulation approaches and computational domains now employed. Here, we will discuss only the most recent efforts which are most directly relevant to the work described in this dissertation.

2.4.1 2D Radial-Axial (r - z)

Over the past 20 years, there have been a number of two-dimensional (2D) simulations formulated in the radial-axial (r - z) coordinate system. The most directly relevant is the work started at MIT by Lentz (1990) and Fife (1995; 1999), then continued, with a distinct

implementation but similar approach, at the Stanford Plasma Physics Laboratory by Fernandez et al. (1998), Scharfe (2009), and, most recently, Cha (2015). These simulations use a hybrid fluid-PIC approach, similar to that employed for the work in this dissertation; the r - z simulations typically model the full annular channel width $W = r_{outer} - r_{inner}$ in r and the full axial extent of the Hall thruster discharge, starting at the anode plane and extending past the thruster exit plane into the near plume, in z . Additional hybrid fluid-PIC r - z simulations developed during this time include work by Hagelaar et al. (2002), Bareilles et al. (2004), and Koo and Boyd (2004); further extensions to Fife's original work include the work of Parra et al. (2006) and Hofer et al. (2006; 2010). Most recently, Cha developed an improved electron mobility model (Cha et al., 2015) and used these simulations to study the use of alternative propellant gases, in lieu of the typical Xe fuel (Cha et al., 2009). Aside from the discrepancy in the computational domains (coordinate formulations), the work of Scharfe and Cha is most closely analogous to the work described in this dissertation.

In all cases, the primary challenge in these r - z simulations has been the effective modeling of the so-called anomalous cross-field electron mobility. Because these r - z models do not treat the azimuthal (θ) direction, they must use some other means to account for the azimuthal dynamics and any resulting enhancement to the axial electron mobility. Complicated theoretical and computational models (e.g., Scharfe, 2009; Cha, 2015) have been developed to account for the super-classical electron mobility (i.e., mobility beyond that predicted by the classical theory and relevant r - z dynamics); in many cases, the electron mobility model must be tuned, i.e., empirically fit by adjusting model parameters, for each operating condition.

2.4.2 2D Axial-Azimuthal (z - θ)

In an attempt to address this shortcoming of the r - z simulations and develop a more sound basis for the electron transport description, 2D simulations were formulated in the axial-azimuthal (z - θ) coordinate system. The primary purpose of these simulations is to simulate azimuthal fluctuations in plasma properties, specifically the electron density and electron velocities, and study their effect on the electron mobility in the directions perpendicular to the magnetic field, particularly the z -direction.

Knoll developed a 2D z - θ simulation using a fully fluid approach in which all species (electron, ions, and neutrals) are modeled using a fluid continuum treatment (Knoll, 2010). Knoll's work enabled the simulation and study of high-frequency, short-wavelength disturbances in a discharge similar to that modeled in this dissertation. However, the approach is predicated on the validity of the fluid continuum treatment for all species, and, with the given implementation, which focused on resolving relatively small length and time scales, and available computing power, the time extent of simulations is limited to approximately $10 \mu\text{s}$ of simulated time.

Adam and Garrigues have performed kinetic simulations (employing PIC electrons and ions with a neutral fluid background) in the z - θ coordinate system (Adam et al., 2004; Garrigues and Coche, 2013); however, due to the computational expense of the kinetic approach, certain compromises must be made to make such simulations computationally tractable. These simulations have a truncated (partial) azimuthal extent, which can introduce artificial periodicity in the azimuthal direction. To reduce the computational expense associated with resolving the length and time scales of interest, they also employ certain artificial scaling techniques, such as scaling the length and time scales by a permittivity scaling factor in lieu of using the physical free space permittivity ϵ_0 (Garrigues and Coche, 2013).

The work described in this dissertation is an attempt to address the theoretical and computational gap between these two extremes; the hybrid fluid-PIC approach represents a practical compromise in computational expense between the fully fluid and fully kinetic treatments. Building upon similar model implementations for r - z simulations (Fernandez et al., 1998; Scharfe, 2009), we have developed a complementary z - θ hybrid fluid-PIC model.

2.4.3 3D (x - y - z or r - z - θ)

More recently, enabled by advances in computational capability, a number of three-dimensional (3D) kinetic simulations have been developed, e.g. by Taccogna et al. (2013) and Matyash et al. (2013). To reduce computational expense, present 3D simulations either limit the extent of the computational domain, e.g., to a partial azimuthal (Taccogna

et al., 2013) or minimal axial extent (Oudini et al., 2013), or employ an artificial geometric scaling (Taccogna et al., 2013; Matyash et al., 2013). In the case of these 3D simulations, the primary challenge and present limiting factor is the computational expense; even with state-of-the-art computational capability and parallelization, relevant 3D simulations are extremely computationally expensive; typical wall clock time for relevant simulations, focused on resolving high-frequency, short-wavelength phenomena, is 20 days on 4 processors for a simulated time extent of $24 \mu\text{s}$ (Matyash et al., 2013).

2.5 Relevance of Described Research

As discussed in Sect. 2.4.2, the primary purpose of 2D axial-azimuthal simulations is to provide a means for studying azimuthal fluctuations and their impact on electron transport. In this dissertation, we describe the development of a 2D axial-azimuthal (z - θ) hybrid-fluid PIC model which is used to characterize cross-field azimuthal fluctuations in a discharge similar to that modeled by Scharfe (2009) and Knoll (2010). The model described here has two key distinguishing features which enable simulations that complement and augment the existing body of work.

The first distinguishing feature is the extent of the computational domain. We model a full size Hall thruster discharge; the model geometry, which will be further described in Chap. 3, is based on that of a full size laboratory prototype Hall thruster. The axial extent of the computational domain includes the entire length of the thruster, starting from the anode plane and extending past the exit plane into the near plume region; in the azimuthal direction, the computational domain includes the full azimuth, which prevents the introduction of any artificial periodicity (as can occur when periodic boundary conditions are employed with a truncated partial azimuth computational domain). The model does not employ any artificial scaling in the geometry or time scales or any other parameters. As far as we know, complemented by the work of Knoll (2010), these simulations (Lam et al., 2009) are among the first z - θ -resolved simulations of an entire thruster, including the full length of the thruster channel and the full azimuth, that are performed without ad hoc artificial scaling of the physical scales (as is often done in fully kinetic PIC simulations).

The second distinguishing feature is the available time extent of these simulations. The computational efficiency of the hybrid fluid-PIC approach enables simulations on the order of 1 ms of simulated time, using modest computational resources; typical wall clock time for a 1 ms simulation, using the time step and spatial grid described in Chap. 4, is approximately 4-5 days on a single processor. The time extent of these simulations enables the observation and study of low- to mid-frequency fluctuations in the range of approximately 10 kHz to 10 MHz; such fluctuations in this lower frequency range cannot be accessed by other comparable 2D (z - θ) and 3D simulations, which, due to their focus on finer time and spatial scales, are limited to shorter simulated time extents on the order of 1-10 μ s.

Chapter 3

Hybrid Fluid-PIC Axial-Azimuthal (z - θ) Model

The model described and developed here follows from previous efforts (Fernandez et al., 1998; Fife, 1999; Scharfe et al., 2006; Scharfe, 2009) to develop similar hybrid fluid-PIC models in the two-dimensional (2D) radial-axial (r - z) domain. The initial axial-azimuthal (z - θ) model was developed by Fernandez (Fernandez et al., 2005) and is similar to the previous radial-axial (r - z) models developed by Fife, Scharfe and Fernandez. We have since extended and improved the initial z - θ model to include additional physical phenomena and enhance numerical stability.

We employ a hybrid Fluid-PIC approach for the z - θ model. The heavy species, Xe and Xe^+ , are modeled using a Particle-In-Cell (PIC) treatment, while the electrons are treated as a two-dimensional (2D) fluid continuum. The PIC and fluid treatments are coupled by assuming space charge neutrality or quasineutrality.

3.1 Model Geometry and Computational Domain

The geometry simulated is that of a laboratory Hall discharge, known as the Stanford Hall thruster (SHT), for which a considerable amount of experimental data has been gathered (Hargus, 2001; Meezan et al., 2001; Meezan, 2002).

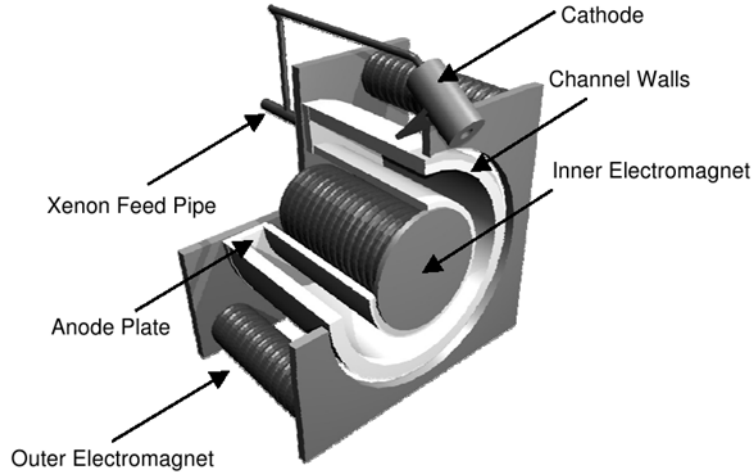


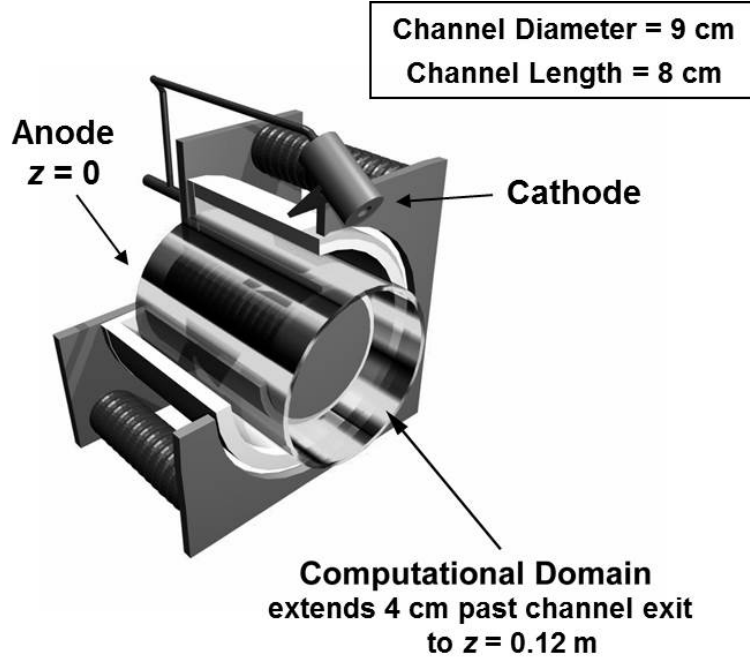
Figure 3.1: Schematic of the Stanford Hall Thruster (SHT) laboratory discharge geometry.

The SHT is comprised of two coaxial alumina (Al_2O_3) tubes which form the annular thruster channel as shown in Fig. 3.1. The simulated channel has an outer diameter of 9.4 cm and an inner diameter 7 cm which gives a radial channel width of 1.2 cm. The axial channel length is approximately 8 cm.

A magnetic circuit, comprised of inner and outer magnetic coils and plates, provides a primarily radial magnetic field as shown in Fig 3.3. The anode plane is located at the closed end of the thruster channel. A hollow cathode is located outside of the thruster channel, approximately 2 cm downstream of the thruster exit plane. The voltage applied between the anode and cathode creates the primarily axial electric field within the thruster channel.

The neutral propellant xenon (Xe) gas is supplied at a total mass flow rate of 2.3 mg/s via holes in the anode plate and via the hollow cathode. The SHT discharge was operated over a range of applied voltages between 100 V and 250 V. Hargus (2001) and Meezan (2002) describe the SHT geometry, operation, and laboratory measurements in greater detail.

The 2D computational domain is constructed in the axial-azimuthal (z - θ) plane starting, in the z -direction, at the anode plane and extending beyond the exit plane into the discharge plume; in the θ -direction, we include the full azimuth (0 to 2π radians), as shown in Fig. 3.2. With the exception of the radial magnetic field effect (i.e., the effect of the radial

Figure 3.2: 2D axial-azimuthal (z - θ) computational domain.

magnetic field on charged particle motion in the z - and θ -directions), radial dynamics, such as radial forces and radial motion, are not modeled; instead, we consider the radial midpoint of the channel $r_{\text{mid}} = 4.1$ cm. The domain can be thought of as the projection of the three-dimensional (actual) physical geometry onto the z - θ plane located at $r_{\text{mid}} = 4.1$ cm.

While the computational domain is 2D in z - θ , we consider the cross-sectional thruster area and are interested in extensive properties, such as total current or flux through the simulated thruster. In this context, we can consider the 2D z - θ domain to be three-dimensional with unit length in the r -direction and unit cross-sectional area in the r - z plane. The cross-sectional area of interest in the r - z plane, per the SHT geometry, is

$$A_{\text{sect}} = \pi(r_{\text{outer}}^2 - r_{\text{inner}}^2) \simeq 31 \text{ cm}^2 = 0.0031 \text{ m}^2 \quad (3.1)$$

where $r_{\text{outer}} = 4.7$ cm and $r_{\text{inner}} = 3.5$ cm are the outer and inner radii of the thruster channel, respectively. We consider any transverse simulated quantities, e.g., electron current flux perpendicular to the in the z -direction (i.e., perpendicular to the θ -direction or the r - θ

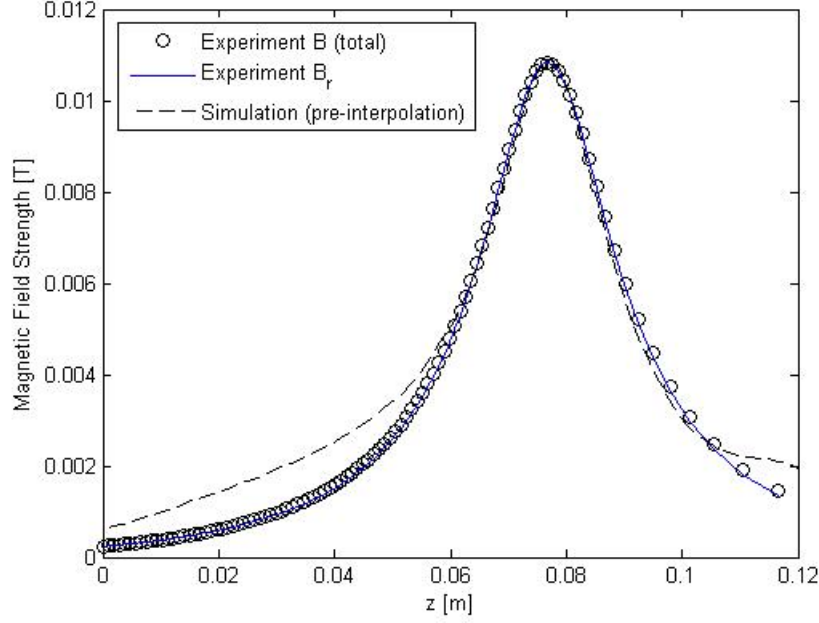


Figure 3.3: Axial variation of simulated and experimentally-measured magnetic field for Stanford Hall Thruster (SHT). Laboratory measurements of the total magnetic field strength and radial magnetic field were taken at the radial midpoint of the SHT channel $r_{mid} = 4.1$ cm.

plane) , to be on a per unit area basis; the per unit area quantity must thus be multiplied by the thruster (domain) cross-sectional area $A_{sect} = 31 \text{ cm}^2$ to obtain the corresponding extensive property for the thruster (i.e., for the physical 3D geometry).

In the model, the imposed constant magnetic field is based on experimental measurements of the predominantly radial magnetic field strength. The magnetic field strength measurements were taken at the midway (mid-channel) radial location $r_{mid} = 4.1$ cm for various locations along the SHT z -axis. Figure 3.3 shows both the experimentally-measured and simulated magnetic field strength. The measured magnetic field strength peaks at a value of approximately $B_r = 0.011$ T just upstream of the channel exit. Note that for the experimentally-measured magnetic field, the radial component of the magnetic field B_r is nearly equivalent to the total magnetic field strength; hence, the magnetic field is predominantly radial. In the model, we take the magnetic field to be purely radial. Figure 3.3 shows the magnetic field strength profile $B_r(z)$ used to initialize the simulation. The

simulated magnetic field strength curve $B_r(z)$ is specified at a set of 71 equally-spaced z -locations throughout the domain ($0 \leq z \leq 0.12$ m); a linear interpolation is then used to find the magnetic field strength at the z -locations specified by the, sometimes nonuniform, computational grid. The imposed interpolated magnetic field profile is taken to be constant in time. The simulated axial electric field is imposed by a constant positive voltage (relative to 0 V) applied at the anode.

We orient the coordinate system such that the positive z -direction corresponds to the direction of positive axial electric field. The anode plane is located at $z = 0$. The channel exit is at approximately $z = 0.08$ m and the domain extends approximately 4 cm past the exit plane to $z = 0.12$ m. We treat the magnetic field as purely radial which leads to an $\mathbf{E} \times \mathbf{B}$ drift velocity in the purely azimuthal direction. We orient the coordinate system such that the $\mathbf{E} \times \mathbf{B}$ drift velocity is in the positive θ -direction, i.e., $\mathbf{B} = B_r \hat{r}$, \mathbf{E} is primarily in the positive z -direction ($\mathbf{E} \simeq E_z \hat{z}$), and $\hat{\theta} = \hat{z} \times \hat{r}$. While we focus here on simulations of the SHT, the model can be adapted to simulate other thruster geometries, especially those of similar geometric scale.

3.2 Key Assumptions

We assume space charge neutrality, or quasineutrality, throughout the computational domain. This quasineutrality assumption is consistent with modeling large-scale phenomena since the Debye length of the typical Hall thruster plasma is smaller than the length scales of interest (Fife, 1999; Chouieri, 2001). The Debye length

$$\lambda_D = \sqrt{\frac{\epsilon_0 k_B T_e}{e^2 n_e}} \quad (3.2)$$

where $\epsilon_0 = 8.85 \times 10^{-12}$ F/m is the free space permittivity, $k_B = 1.38 \times 10^{-23}$ m²kg s⁻²K⁻¹ is the Boltzmann constant, and $e = 1.6 \times 10^{-19}$ C is the elemental electron charge, indicates the length scale over which charge, or Debye, shielding occurs. At length scales smaller than the Debye length, significant space charge separation can be observed; however, for length scales greater than the Debye length, the plasma appears electrically neutral due to the plasma, or Debye, shielding effect. For typical SHT operation, the maximum Debye

length, based on typical values for the plasma density $n_e \sim 10^{17} - 10^{18} \text{ m}^{-3}$ and electron temperature $T_e \sim 3\text{-}18 \text{ eV}$, is approximately $\lambda_D \simeq 0.1 \text{ mm}$; this maximum Debye length is much smaller than the thruster length scales of interest and the spatial resolution of the computational grid used for the electron fluid and PIC calculations. Hence, for the length scales of interest (and at the resolution of the computational grid), the space charge is effectively zero, and we can assume that the ion and electron number densities are equal. The enforcement of quasineutrality allows us to couple the ion particle (PIC) and electron fluid model treatments. As will be described in Chap. 4, we calculate the ion number density via the PIC treatment; per quasineutrality, we take the electron number density to be equal to the ion number density or, more generally, the plasma number density.

As previously mentioned, we assume the magnetic field is purely radial. At each z -location, we impose a magnetic field strength based on experimental measurements of the magnetic field strength as shown in Fig. 3.3. We assume that the interpolated time-constant magnetic field acts only in the radial direction. In reality, the magnetic field has some component in the z - and θ -directions; however, based on the magnetic field measurements shown in Fig. 3.3, we assume that the non-radial components are small compared to the radial field strength and can thus be neglected. The electron fluid dynamics are subject to the magnetic field. Due to their relatively large mass and consequently large Larmor radius (which will be further discussed in Sect. 3.4), we treat the ion particles as non-magnetized.

As will be described in Sect. 3.5, we assume the electron temperature to be axisymmetric in θ and therefore one-dimensional (1D) in z . We expect that the azimuthal variation in the electron temperature is small compared to the axial variation, i.e., $\frac{\partial T_e}{\partial \theta} \ll \frac{\partial T_e}{\partial z}$. At each z -location, we make the simplifying assumption that the azimuthal variation in the electron temperature is negligible; we take the electron temperature to be constant in θ which results in a 1D electron temperature distribution that varies only in z .

3.3 Neutral Gas

Atomic xenon (Xe) comprises the neutral propellant background gas. Neutral Xe atoms are modeled as collisionless discrete superparticles. The neutral particles are initialized, either per the simulation initial conditions or when injected from the anode plane, with

initial positions and velocities in z and θ . Each neutral particle's trajectory is determined by its initial velocity (in z and θ) as there is no external applied force to alter the particle's velocity. The particle advances in either the positive z - or negative z -direction until it exits the computational domain at either the upstream (anode plane at $z = 0$) or downstream ($z = 0.12$ m) domain boundary.

Collisions between particles, i.e., between two neutrals or between a neutral and an ion, are not modeled. Based on a rigid sphere collision model (Vicenti and Kruger, 1965) with a peak neutral number density $n_n = 10^{20} \text{ m}^{-3}$, the typical mean free path for collisions between two neutrals $\lambda_{mfp,nn} \gtrsim 4 \text{ cm}$. The minimum mean free path $\lambda_{mfp,nn} = 4 \text{ cm}$ is comparable to the thruster channel length and azimuthal extent; based on this calculated minimum mean free path, a neutral would likely undergo a maximum of 3-5 collisions with another neutral in the course of traversing the entire computational domain. In regions where the neutral density is lower, $\lambda_{mfp,nn}$ is even larger, and collisions between neutrals are less likely (i.e., less frequent). The maximum ion number density is typically two to three orders of magnitude smaller than the peak neutral number density; furthermore, the ions are quickly accelerated out of the thruster channel and the corresponding computational domain by the strong axial electric field. The mean free path for collisions between an ion and a neutral is correspondingly greater than that for neutral-neutral collisions, i.e., $\lambda_{mfp,in} > \lambda_{mfp,nn}$. Consequently, we neglect both neutral-ion and neutral-neutral collisions. Since there are no radial dynamics, particle collisions with the inner and outer radial walls of the thruster channel are not modeled. Particle collisions with the anode ($z = 0$) plane wall are not modeled; neutral particles exit the domain and are removed from the simulation if they cross the anode ($z = 0$) plane. Since we do not explicitly model particle collisions with the channel walls and we neglect particle-to-particle collisions, we consider the particles to be collisionless.

Neutral particles are continuously injected into the domain from the anode ($z = 0$) plane according to the prescribed mass flow rate of 2.3 mg/s. Each injected neutral particle enters the domain at a randomized θ location; on average, the particles are injected uniformly in θ across the anode ($z = 0$) plane. Particles injected at the anode enter the computational domain with a positive initial z -velocity, which is sampled from a one-way Maxwellian flux distribution, shown in Fig. A.4a, based on an anode temperature $T_{anode} = 650\text{K}$ with a

mean (bulk) neutral injection velocity $v_0 = 300$ m/s; while these parameters for the velocity distribution were not directly experimentally measured, the discharge does not appear to be particularly sensitive to the anode temperature. The injected particles then advance in the positive z -direction until they exit the computational domain at the downstream ($z = 0.12$ m) domain boundary. The injected particle's initial θ -velocity can be positive or negative; it is determined by projecting the particle's sampled speed in the r - θ plane onto the $\hat{\theta}$ -direction, accounting for the particle's θ -position, as described in Appendix A. The particle's speed in the r - θ plane is sampled from a 2D Maxwellian speed distribution, based on the anode temperature $T_{anode} = 650$ K.

3.4 Ions

Neutral Xe ions are ionized to form Xe^+ ions. In the model, we include only singly-charged (or singly-ionized) Xe^+ ions; doubly-charged Xe^{++} and other more highly-ionized ions are not included.

We assume that Xe^+ ions are created only by electron-neutral collisions. Similarly to Fife (1999), we expect that, for the electron temperatures of interest, the number of doubly-charged Xe^{++} ions (created by $\text{Xe}^+ \rightarrow \text{Xe}^{++}$ ionization and direct $\text{Xe} \rightarrow \text{Xe}^{++}$ ionization, via electron- Xe^+ and electron-neutral collisions, respectively) is negligible compared to the number of Xe^+ ions; hence, the presence of Xe^{++} ions is neglected. For more highly-ionized ions, we expect that their ionization (i.e., creation) rates will be even lower than that for Xe^{++} ions, so they too can justifiably be neglected. Fife (1999) provides further discussion of the relative prevalence of the various positive ion species and their corresponding ionization (creation) rates.

The singly-charged Xe^+ ions are modeled as discrete superparticles. Typically, charged particle motion is governed by the Lorentz force, in this case,

$$\mathbf{F}_{\text{Lorentz}} = m_i \mathbf{a}_i = q_i (\mathbf{E} + \mathbf{v}_i \times \mathbf{B}) \quad (3.3)$$

Typical ion velocities (e.g., as measured in laboratory experiments) vary with axial position within the range of ~ 100 m/s - 15,000 m/s. We consider the Larmor radius, or ion gyroradius, due to the magnetic field contribution to the Lorentz force

$$r_{Larmor} = \frac{m_i v_{\perp}}{q_i B} \quad (3.4)$$

where v_{\perp} is the velocity in the direction perpendicular to the magnitude (in this case, either the particle's z - or θ -velocity). The Larmor radius indicates the effect of the magnetic field on the charged particle motion; specifically, it is the radius of curvature associated with particle gyromotion due to the magnetic field. For the range of ion z - and θ -velocities and magnetic field strength values here, we find that the Larmor radius is much larger than the thruster length scales of interest. An ion moving at a typical velocity of $v_{\perp} = 10,000$ m/s in the region of near peak magnetic field strength $B_r = 0.01$ T, near the thruster exit plane, will have an approximate Larmor radius $r_{Larmor} \simeq 140$ cm. Further upstream in the thruster channel (toward the anode plane), ions move more slowly and the magnetic field is weaker; an ion with a typical velocity $v_{\perp} = 100$ m/s subject to a magnetic field strength $B_r = 0.001$ T will have an approximate Larmor radius $r_{Larmor} \simeq 14$ cm. Compared to the thruster channel length (8 cm) and azimuthal extent (at the midway radial location $r_{mid} = 4.1$ cm, the length scale of the z - θ plane is $2\pi r_{mid} \simeq 26$ cm), the Larmor radius values are much larger than the thruster length scales of interest. Due to the relatively large ion mass, and consequently large Larmor radius relative to the thruster length scales of interest, we neglect the effect of the magnetic field on the ion motion and consider the ion particles to be non-magnetized.

The ion particle motion is thus governed by only the locally-computed electric field. Since we consider only singly-charged Xe^+ ions, the ion charge is equivalent to the elemental electron charge $e = 1.6 \times 10^{-19}$ C. The ion acceleration is determined by the ion mass $m_i = m_{\text{Xe}^+}$ subject to the simplified (non-magnetized) Lorentz force:

$$\mathbf{a}_i = \frac{e}{m_i} \mathbf{E} \quad (3.5)$$

which gives the ion particle velocities

$$v_z = \frac{e}{m_i} \int E_z dt \quad (3.6a)$$

$$v_\theta = \frac{e}{m_i} \int E_\theta dt \quad (3.6b)$$

and position

$$z = \int v_z dt \quad (3.7a)$$

$$\theta = \int v_\theta dt \quad (3.7b)$$

Each ion particle moves through the computational domain until it exits the computational domain at either the upstream (anode plane at $z = 0$) or downstream ($z = 0.12$ m) domain boundary.

As in the case of the neutral particles, collisions between particles, i.e., between two ions or between an ion and a neutral, are not modeled. As discussed in Sect. 3.3, we expect the mean free path for collisions between an ion and a neutral $\lambda_{mfp,in}$ to be greater than the relevant thruster and computational domain length scales. We expect the mean free path for collisions between two ions to be even greater than than for ion-neutral collisions, i.e., $\lambda_{mfp,ii} \gg \lambda_{mfp,in} \gg \lambda_{mfp,nn}$, since the maximum ion number density is typically several orders of magnitude smaller than the neutral number density. We thus justifiably neglect ion-neutral and ion-ion particle collisions. Ion particle collisions with the thruster channel walls, including the inner and outer radial walls and the anode plane, are also neglected. At the anode plane, the ion particles are treated in the same way as the neutral particles; ion particles exit the domain and are removed from the simulation if they cross the anode ($z = 0$) plane. In general, we neglect radial particle motion and dynamics; hence, in this 2D model, there is no mechanism by which the ion particles can collide with the the inner and outer radial thruster walls. We thus consider the particles to be collisionless. Similarly to Fife (1999), we neglect ion-neutral momentum and charge exchange; these effects are not expected to be significant within the computational domain.

The singly-charged Xe^+ ions are created by ionizing neutral Xe atoms according to the local electron-neutral impact ionization rate. We use the ionization rate model described by Ahedo et al. (2001)

$$\dot{n}_e = n_n n_e \sqrt{\frac{8k_B T_e}{\pi m_e}} \sigma_{i0} \left(1 + \frac{T_e E_i}{(T_e + E_i)^2} \right) \exp \left\{ -\frac{E_i}{T_e} \right\} \quad (3.8)$$

where n_n and n_e are the neutral and electron number densities, respectively, T_e is the electron temperature, $k_B = 1.38 \times 10^{-23} \text{ m}^2 \text{ kg s}^{-2} \text{ K}^{-1}$ is the Boltzmann constant, $m_e = 9.1 \times 10^{-31} \text{ kg}$ is the elemental electron mass, $\sigma_{i0} = 5 \times 10^{-20} \text{ m}^2$ is a constant (with units of collision cross section or area), and $E_i = 12.13 \text{ eV}$ (or 140,757 K) is the first ionization energy for Xe. The ionization rate depends non-linearly on electron temperature; it is determined from an analytical expression developed to fit experimental cross sections (Rapp and Englander-Golden, 1965; Mathur and Badrinathan, 1987) and assumes a Maxwellian distribution for the electrons.

3.5 Electron Fluid

We model the electrons as a 2D fluid continuum. In general, the continuum approximation is valid when the fluid is sufficiently collisional, i.e., the mean free path is much smaller than the length scales of interest. For typical SHT operation, the maximum electron mean free path is approximately $\lambda_{mfp} \simeq 1 \text{ cm}$ (based on typical values for the electron velocity $v_e \sim 10^4 \text{ m/s}$ and electron-neutral collision frequency $\nu_{en} \sim 10^6 \text{ s}^{-1}$). In a plasma, the magnetic field has a further equilibrating effect due to the charged particle gyromotion; because of their extremely small mass ($m_e \simeq 9.2 \times 10^{-31} \text{ kg}$), the electrons have a small Larmor radius on the order of $r_{Larmor} \simeq 0.01 \text{ cm}$ or less, which causes the electrons to tend towards being Maxwellian (or nearly Maxwellian) at length scales comparable to the Larmor radius. The maximum electron Larmor radius is significantly smaller than the thruster length scales of interest and the spatial resolution of the computational grid used for fluid calculations. The electron population tends to be locally Maxwellian (at sufficiently small spatial scale); hence, the fluid continuum treatment is a valid approximation, especially in the z - and θ - directions, which are perpendicular to the radial magnetic field.

We model the electron fluid by considering moments of the Boltzmann equation. The electron fluid is 2D in z and θ , and we consider the first and second moments (continuity and momentum, respectively) of the Boltzmann equation in both z and θ . We consider the third moment (energy) of the Boltzmann equation in a quasi-1D sense. We assume the electron temperature to be axisymmetric in θ and therefore one-dimensional (1D) in z ; we thus use a θ -averaged version of the electron energy equation as will be described in Sect. 3.5.3.

3.5.1 Continuity (Species and Current Conservation)

We consider the species continuity equations for the electron and ion species, respectively,

$$\frac{\partial n_e}{\partial t} + \nabla \cdot (n_e \mathbf{u}_e) = w_e \quad (3.9a)$$

$$\frac{\partial n_i}{\partial t} + \nabla \cdot (n_i \mathbf{u}_i) = w_i \quad (3.9b)$$

where n_e and n_i are the number densities, \mathbf{u}_e and \mathbf{u}_i are the macroscopic fluid velocity vectors, and w_e and w_i are the species production rates of the respective electron and ion species.

In this case, the species production rates are equivalent to the ionization rate described by Eqn. 3.8.

$$w_e = w_i = \dot{n}_e \quad (3.10)$$

We can, thus, combine Eqns. 3.9a and 3.9b (i.e., subtract Eqn. 3.9a from Eqn. 3.9b) to obtain:

$$\frac{\partial}{\partial t}(n_i - n_e) + \nabla \cdot (n_i \mathbf{u}_i - n_e \mathbf{u}_e) = 0 \quad (3.11)$$

As discussed in Sect. 3.2, we assume quasineutrality

$$n_i = n_e \quad (3.12)$$

By substituting Eqn. 3.12 into Eqn. 3.11, we obtain:

$$\nabla \cdot [n_e(\mathbf{u}_i - \mathbf{u}_e)] = 0 \quad (3.13)$$

Note that if we multiply Eqn. 3.13 by the elemental electron charge $e = 1.6 \times 10^{-19}$ C, we obtain the current continuity equation

$$\nabla \cdot \mathbf{J} = 0 \quad (3.14)$$

where

$$\mathbf{J} = e(n_i\mathbf{u}_i - n_e\mathbf{u}_e) = en_e(\mathbf{u}_i - \mathbf{u}_e) \quad (3.15)$$

is the total electrical current density.

3.5.2 Momentum Conservation

We consider the generalized electron momentum equation (e.g., from Bittencourt, 2004)

$$\begin{aligned} m_en_e \left(\frac{\partial \mathbf{u}_e}{\partial t} + \mathbf{u}_e \cdot \nabla \mathbf{u}_e \right) = & -en_e(\mathbf{E} + \mathbf{u}_e \times \mathbf{B}) - \nabla \cdot \mathbb{P}_e - m_en_e\nu_{en}(\mathbf{u}_e - \mathbf{u}_n) \\ & - m_en_e\nu_{ei}(\mathbf{u}_e - \mathbf{u}_i) - m_e w_e \mathbf{u}_e \end{aligned} \quad (3.16)$$

where $m_e = 9.1 \times 10^{-31}$ kg is the elemental electron mass, \mathbf{E} is the electric field vector, \mathbf{B} is the magnetic field vector, \mathbb{P}_e is the electron pressure tensor, ν_{en} and ν_{ei} are the respective electron-neutral and electron ion collision frequencies, and $w_e = \dot{n}_e$ is the ionization rate (or electron species production rate). The left-hand side of Eqn.3.16 is equivalent the the substantive, or material, derivative $\frac{D\mathbf{u}_e}{Dt}$ of the electron velocity; the right-hand side includes terms for the Lorentz force, the electron pressure, the collisional drag due to electron-neutral and electron-ion collisions, and the impulsive drag associated with newly produced electrons. We then make a number of simplifying assumptions:

1. We neglect the inertial term $\frac{D\mathbf{u}_e}{Dt} = \frac{\partial \mathbf{u}_e}{\partial t} + \mathbf{u}_e \cdot \nabla \mathbf{u}_e$ on the left-hand side of Eqn. 3.16. Due to the small electron mass, $m_e n_e \frac{\partial \mathbf{u}_e}{\partial t} \simeq 0$; we further expect that $\nabla \mathbf{u}_e \ll (v_{en} + v_{ei})$. The result is that the left-hand side of Eqn. 3.16 $m_e n_e \left(\frac{\partial \mathbf{u}_e}{\partial t} + \mathbf{u}_e \cdot \nabla \mathbf{u}_e \right) \simeq 0$.
2. We assume that the neutrals and ions are effectively stationary relative to the electron fluid (for the continuum timescales of interest). Specifically, we assume that the macroscopic neutral and ion velocities are small compared to the electron velocity, i.e., $\mathbf{u}_n \ll \mathbf{u}_e$ and $\mathbf{u}_i \ll \mathbf{u}_e$; the result is that we can neglect the respective neutral and ion velocities, i.e., $\mathbf{u}_n \simeq 0$ and $\mathbf{u}_i \simeq 0$, in the third and fourth terms, respectively, on the right-hand side of Eqn. 3.16.
3. We assume that the electron pressure is isotropic and that it obeys the ideal gas law. Under these assumptions, the electron pressure tensor \mathbb{P}_e reduces to a scalar value $p_e = nk_B T_e$, where $k_B = 1.38 \times 10^{-23} \text{m}^2 \text{kgs}^{-2} \text{K}^{-1}$ is the Boltzmann constant and T_e is the electron temperature.
4. We consider a single total collision frequency $\nu_e = \nu_{ei} + \nu_{en}$; with this substitution and based on assumption 2 above, the third and fourth terms on the right-hand side of Eqn. 3.16 collapse into a single term $m_e n_e \nu_e \mathbf{u}_e$. However, we neglect Coulomb collisions per the ionization rate treatment described in Ahedo et al. (2001), i.e., we assume $\nu_{ei} \ll \nu_{en}$ and, thus, $\nu_e \simeq \nu_{en}$.
5. We assume that the electron production rate, i.e., the ionization rate, is small compared to the number of electron (in this case, electron-neutral) collisions, i.e., $w_e \ll n_e \nu_e$; the result is that we can neglect the last term on the right-hand side of Eqn. 3.16.

Under these assumptions, Eqn. 3.16 reduces to the following simplified electron momentum equation, or the so-called drift-diffusion approximation:

$$0 = -en_e (\mathbf{E} + \mathbf{u}_e \times \mathbf{B}) - \nabla p_e - m_e n_e \nu_e \mathbf{u}_e \quad (3.17)$$

Making the substitutions $p_e = nk_B T_e$ and $\nu_e \simeq \nu_{en}$, we obtain:

$$0 = -en_e (\mathbf{E} + \mathbf{u}_e \times \mathbf{B}) - \nabla (n_e k_B T_e) - m_e n_e \nu_{en} \mathbf{u}_e \quad (3.18)$$

Since we assume the magnetic field is purely radial as discussed in Sect. 3.2, $\mathbf{B} = B_r \hat{r}$. We can write the simplified momentum equation for each of the coordinate directions, \hat{z} and $\hat{\theta}$, for our 2D coordinate system.

In the \hat{z} -direction:

$$m_e n_e v_{en} u_{ez} = -en_e E_z + en_e u_{e\theta} B_r - \frac{\partial}{\partial z} (n_e k_B T_e) \quad (3.19a)$$

In the $\hat{\theta}$ -direction:

$$m_e n_e v_{en} u_{e\theta} = -en_e E_\theta - en_e u_{ez} B_r - \frac{1}{r} \frac{\partial}{\partial \theta} (n_e k_B T_e) \quad (3.19b)$$

We consider the electron cyclotron frequency

$$\omega_{ce} = \frac{e B_r}{m_e} \quad (3.20)$$

and introduce the classical electron mobility

$$\mu_\perp = \frac{e}{m_e v_{en} \left[1 + \left(\frac{\omega_{ce}}{v_{en}} \right)^2 \right]} \quad (3.21a)$$

and the corresponding electron diffusion constant

$$D_\perp = \frac{k_B T_e}{e} \mu_\perp \quad (3.21b)$$

where

$$v_{en} = n_n \sigma_{en} \bar{c}_e = n_n \sigma_{en} \left(\frac{8 k_B T_e}{\pi m_e} \right)^{1/2} \quad (3.22)$$

is the electron-neutral collision frequency described by Ahedo et al. (2001) (and also used to calculate the ionization rate in Eqn. 3.8), assuming a constant collision cross-section $\sigma_{en} \simeq 27 \times 10^{-20} \text{ m}^2$ for Xe.

Making these substitutions, we can combine Eqns. 3.19a and 3.19b to obtain the following expressions for the electron velocity components:

$$\begin{aligned}
 u_{ez} = & -\mu_{\perp} E_z - \frac{D_{\perp}}{n_e} \frac{\partial n_e}{\partial z} - \frac{D_{\perp}}{T_e} \frac{\partial T_e}{\partial z} - \frac{1}{1 + \left(\frac{v_{en}}{\omega_{ce}}\right)^2} \frac{E_{\theta}}{B_r} \\
 & - \frac{1}{1 + \left(\frac{v_{en}}{\omega_{ce}}\right)^2} \frac{k_B T_e}{en_e B_r r} \frac{\partial n_e}{\partial \theta} - \frac{1}{1 + \left(\frac{v_{en}}{\omega_{ce}}\right)^2} \frac{k_B}{e B_r r} \frac{\partial T_e}{\partial \theta}
 \end{aligned} \tag{3.23a}$$

$$\begin{aligned}
 u_{e\theta} = & -\mu_{\perp} E_{\theta} - \frac{D_{\perp}}{n_e r} \frac{\partial n_e}{\partial \theta} - \frac{D_{\perp}}{T_e r} \frac{\partial T_e}{\partial \theta} + \frac{1}{1 + \left(\frac{v_{en}}{\omega_{ce}}\right)^2} \frac{E_z}{B_r} \\
 & + \frac{1}{1 + \left(\frac{v_{en}}{\omega_{ce}}\right)^2} \frac{k_B T_e}{en_e B_r} \frac{\partial n_e}{\partial z} + \frac{1}{1 + \left(\frac{v_{en}}{\omega_{ce}}\right)^2} \frac{k_B}{e B_r} \frac{\partial T_e}{\partial z}
 \end{aligned} \tag{3.23b}$$

To see how fluctuation-induced transport can occur, we note that the axial electron velocity u_{ez} has a fluctuating $\mathbf{E} \times \mathbf{B}$ term arising from perturbations in the azimuthal electric field E_{θ} ; likewise, azimuthal gradients $\frac{\partial n_e}{\partial \theta}$ in the electron density can affect the axial electron velocity u_{ez} . If the fluctuating plasma density is properly correlated with this fluctuating velocity, transport will result. The impact of these azimuthal fluctuations (E_{θ}) and gradients ($\frac{\partial n_e}{\partial \theta}$) comprises the so-called anomalous contribution to the axial electron velocity; a model which includes only the classical mobility μ_{\perp} and axial gradient terms ($\frac{\partial n_e}{\partial z}$ and $\frac{\partial T_e}{\partial z}$) will underpredict the axial electron velocity and the resulting axial electron transport.

3.5.3 Energy Conservation

We consider the generalized electron energy equation (e.g., from Bittencourt, 2004)

$$\frac{3}{2} n_e k_B \left(\frac{\partial T_e}{\partial t} + \mathbf{u}_e \cdot \nabla T_e \right) + (\mathbb{P}_e \cdot \nabla) \cdot \mathbf{u}_e + \nabla \cdot \mathbf{q}_e = \sum_i S_i \tag{3.24}$$

where $\sum_i S_i$ denotes all the contributing energy source and sink terms. As in Sect. 3.5.2, we assume that the electron pressure is isotropic and that it obeys the ideal gas law; under these assumptions, the electron pressure tensor \mathbb{P}_e reduces to the scalar pressure $p_e = nk_B T_e$. Making this substitution into Eqn. 3.24, we obtain:

$$\frac{3}{2}n_e k_B \frac{\partial T_e}{\partial t} = -\frac{3}{2}n_e k_B \mathbf{u}_e \cdot \nabla T_e - n_e k_B T_e \nabla \cdot \mathbf{u}_e - \nabla \cdot \mathbf{q}_e + \sum_i S_i \quad (3.25)$$

We now consider each term on the right-hand side of Eqn. 3.25. For the energy source and sink terms $\sum_i S_i$, we include Joule heating and ionization losses. We can rewrite Eqn. 3.25 as

$$\frac{3}{2}n_e k_B \frac{\partial T_e}{\partial t} = \dot{E}_{convect} + \dot{E}_{compress} + \dot{E}_{diffuse} + S_{joule} + S_{ioniz} \quad (3.26)$$

where

$$\dot{E}_{convect} = -\frac{3}{2}n_e k_B \left(u_{ez} \frac{\partial T_e}{\partial z} + \frac{u_{e\theta}}{r} \frac{\partial T_e}{\partial \theta} \right) \quad (3.27a)$$

$$\dot{E}_{compress} = -n_e k_B T_e \left(\frac{\partial u_{ez}}{\partial z} + \frac{1}{r} \frac{\partial u_{e\theta}}{\partial \theta} \right) \quad (3.27b)$$

$$\dot{E}_{diffuse} = -\nabla \cdot \mathbf{q}_e \quad (3.27c)$$

and S_{joule} and S_{ioniz} refer to Joule heating and ionization losses, respectively.

We consider the diffusive term $\dot{E}_{diffuse}$ further. We can write the heat rate \mathbf{q}_e as

$$\mathbf{q}_e = -K_{e\perp} \nabla T_e \quad (3.28)$$

where $K_{e\perp}$ is the electron thermal conductivity described in Fife (1999)

$$K_{e\perp} = \frac{5}{2} \frac{k_B^2}{e} n_e T_e \mu_{\perp} \quad (3.29)$$

Making these substitutions, we can rewrite Eqn. 3.27c as

$$\dot{E}_{diffuse} = \nabla \cdot (K_{e\perp} \nabla T_e) \quad (3.30a)$$

$$= \nabla \cdot \left(\frac{5}{2} \frac{k_B^2}{e} n_e T_e \mu_{\perp} \nabla T_e \right) \quad (3.30b)$$

We next consider the Joule heating source term. The electron Joule heating can generally be described as

$$S_{joule} = \mathbf{J}_e \cdot \mathbf{E} \quad (3.31)$$

where \mathbf{J}_e is the electron current density and \mathbf{E} is the electric field vector. We can write the electron current density as

$$\mathbf{J}_e = -en_e \mathbf{u}_e \quad (3.32)$$

We further make the approximation that

$$\mathbf{u}_e \simeq -\mu \mathbf{E} \quad (3.33)$$

where

$$\mu = \frac{e}{m_e v_e} \quad (3.34)$$

and $v_e \simeq v_{en}$ as in Sect. 3.5.2, from which we can approximate the electric field as

$$\mathbf{E} \simeq -\frac{m_e v_{en}}{e} \mathbf{u}_e \quad (3.35)$$

Substituting Eqns. 3.32 and 3.35 into Eqn. 3.31, we obtain the following expression for the Joule heating source term:

$$S_{joule} = m_e n_e v_{en} (\mathbf{u}_e \cdot \mathbf{u}_e) \quad (3.36)$$

$$= m_e n_e v_{en} (u_{ez}^2 + u_{e\theta}^2) \quad (3.37)$$

Finally, we describe the ionization loss (energy sink term) as

$$S_{ioniz} = -\gamma \dot{n}_e k_B E_i - \dot{n}_e \frac{3}{2} k_B T_e \quad (3.38)$$

where $E_i = 12.13$ eV (or 140,757 K) is the first ionization energy for Xe and γ is a multiplicative ionization cost factor. The ionization loss term accounts for the both the energy required to ionize the neutrals and the energy required for the newly created electrons to equilibrate to the local electron temperature T_e . Typically, we use ionization cost factor values $\gamma = 1.0 - 2.8$. The ionization cost factor γ is adjusted in an ad hoc manner based on the thruster operating condition; typically, higher voltage operating conditions require a higher value for the ionization cost factor γ to maintain a numerically stable electron temperature profile $T_e(z)$ that is comparable to experimentally-measured values. An alternative is the ionization cost factor model developed by Dugan and Sovie (1967); for the range of electron temperatures typically simulated, the ionization cost factor used here is comparable to that predicted by the Dugan model.

We make the simplifying assumption that the electron temperature is axisymmetric in θ . At each z -location, we assume the azimuthal variation in the electron temperature is negligible, i.e., $\frac{\partial T_e}{\partial \theta} = 0$. We take the electron temperature to be constant in θ , which results in a 1D electron temperature distribution $T_e = T_e(z, t)$ that varies only in z . Under this 1D electron temperature assumption, we can rewrite the convective and diffusive terms on the right-hand side of Eqn. 3.26. The convective term, described by Eqn. 3.27a, simplifies to

$$\dot{E}_{convect} = -\frac{3}{2} n_e k_B u_{ez} \frac{\partial T_e}{\partial z} \quad (3.39)$$

and the diffusive term, described by Eqn. 3.30b, can be written as

$$\dot{E}_{diffuse} = \frac{5}{2} \frac{k_B^2}{e} \left[\mu_{\perp} T_e \frac{\partial n_e}{\partial z} \frac{\partial T_e}{\partial z} + n_e \mu_{\perp} \left(\frac{\partial T_e}{\partial z} \right)^2 + n_e \mu_{\perp} T_e \frac{\partial^2 T_e}{\partial z^2} + n_e T_e \frac{\partial T_e}{\partial z} \frac{\partial \mu_{\perp}}{\partial z} \right] \quad (3.40)$$

3.5.4 System Closure and Solution for Fluid Equations

3.5.4.1 System of Governing Equations

We consider the current continuity, momentum, and energy equations to form a system of governing equations for the electron fluid. As in Sect. 3.5.3, we assume that electron temperature is 1D in z , i.e., $T_e = T_e(z, t)$ and $\frac{\partial T_e}{\partial \theta} = 0$, which allows us to further simplify the electron velocity expressions in Eqns. 3.23a and 3.23b. We include the current continuity equation (Eqn. 3.13), electron velocity expressions (Eqns. 3.23a-3.23b), and electron energy equation (Eqn. 3.26) to form the following system of governing equations.

$$\nabla \cdot [n_e(\mathbf{u}_i - \mathbf{u}_e)] = 0 \quad (3.41a)$$

$$\begin{aligned} u_{ez} = & -\mu_{\perp} E_z - \frac{D_{\perp}}{n_e} \frac{\partial n_e}{\partial z} - \frac{D_{\perp}}{T_e} \frac{\partial T_e}{\partial z} - \frac{1}{1 + \left(\frac{v_{en}}{\omega_{ce}}\right)^2} \frac{E_{\theta}}{B_r} \\ & - \frac{1}{1 + \left(\frac{v_{en}}{\omega_{ce}}\right)^2} \frac{k_B T_e}{en_e B_r r} \frac{\partial n_e}{\partial \theta} \end{aligned} \quad (3.41b)$$

$$\begin{aligned} u_{e\theta} = & -\mu_{\perp} E_{\theta} - \frac{D_{\perp}}{n_e r} \frac{\partial n_e}{\partial \theta} + \frac{1}{1 + \left(\frac{v_{en}}{\omega_{ce}}\right)^2} \frac{E_z}{B_r} \\ & + \frac{1}{1 + \left(\frac{v_{en}}{\omega_{ce}}\right)^2} \frac{k_B T_e}{en_e B_r} \frac{\partial n_e}{\partial z} + \frac{1}{1 + \left(\frac{v_{en}}{\omega_{ce}}\right)^2} \frac{k_B}{e B_r} \frac{\partial T_e}{\partial z} \end{aligned} \quad (3.41c)$$

$$\frac{3}{2} n_e k_B \frac{\partial T_e}{\partial t} = \dot{E}_{convect} + \dot{E}_{compress} + \dot{E}_{diffuse} + S_{joule} + S_{ioniz} \quad (3.41d)$$

where $\dot{E}_{convect}$, $\dot{E}_{compress}$, $\dot{E}_{diffuse}$, S_{joule} , and S_{ioniz} are as defined in Sect. 3.5.3.

The electron number density $n_e = n_i$ and ion velocities $\mathbf{u}_i = u_{iz}\hat{\mathbf{z}} + u_{i\theta}\hat{\boldsymbol{\theta}}$ are known (obtained) from the ion particle model, described in Sect. 3.4, and PIC treatment, which will be further described in Chap. 4. We thus have a system of 4 equations, with 5 unknowns: u_{ez} , $u_{e\theta}$, E_z , E_{θ} , and T_e .

3.5.4.2 Electric Potential

In order to achieve system closure, we must reduce the number of unknown variables. We introduce the electric potential ϕ , such that

$$\mathbf{E} = -\nabla\phi \quad (3.42)$$

For our 2D z - θ coordinate system,

$$E_z = -\frac{\partial\phi}{\partial z} \quad (3.43a)$$

$$E_\theta = -\frac{1}{r} \frac{\partial\phi}{\partial\theta} \quad (3.43b)$$

Making these substitutions into Eqns. 3.41b and 3.41c, we can reduce the number of unknowns; the result is a system of equations, with 4 unknowns: u_{ez} , $u_{e\theta}$, ϕ , and T_e .

3.5.4.3 Reduced System of Equations for Numerical Solution

We achieve system closure with the set of 4 equations and 4 unknowns. However, we can further reduce the set of equations for numerical solution to a system of 2 equations.

Using the electric potential notation, as defined by Eqns. 3.43a and 3.43b, we substitute the electron velocity expressions (Eqns. 3.41b and 3.41c) into the current continuity equation (Eqn. 3.41a). The result is a single equation that can be solved for the electric potential ϕ :

$$A_1 \frac{\partial^2 \phi}{\partial \theta^2} + A_2 \frac{\partial \phi}{\partial \theta} + A_3 \frac{\partial^2 \phi}{\partial z^2} + A_4 \frac{\partial \phi}{\partial z} + A_5 = 0 \quad (3.44)$$

where

$$A_1 = -\frac{n_e \mu_\perp}{r^2} \quad (3.45a)$$

$$A_2 = -\frac{1}{r} \left[\frac{n_e}{r} \frac{\partial \mu_\perp}{\partial \theta} + \frac{\mu_\perp}{r} \frac{\partial n_e}{\partial \theta} + \frac{1}{1 + \left(\frac{v_{en}}{\omega_{ce}} \right)^2} \frac{\partial}{\partial z} \left(\frac{n_e}{B_r} \right) + \frac{n_e}{B_r} \frac{\partial}{\partial z} \left(\frac{1}{1 + \left(\frac{v_{en}}{\omega_{ce}} \right)^2} \right) \right] \quad (3.45b)$$

$$A_3 = -n_e \mu_\perp \quad (3.45c)$$

$$A_4 = \frac{1}{1 + \left(\frac{v_{en}}{\omega_{ce}} \right)^2} \frac{1}{r B_r} \frac{\partial n_e}{\partial \theta} - n_e \frac{\partial \mu_\perp}{\partial z} - \mu_\perp \frac{\partial n_e}{\partial z} + \frac{n_e}{r B_r} \frac{\partial}{\partial \theta} \left(\frac{1}{1 + \left(\frac{v_{en}}{\omega_{ce}} \right)^2} \right) \quad (3.45d)$$

$$A_5 = f(n_e, T_e, \mu_\perp, v_{en}, \omega_{ce}) + \frac{n_e}{r} \frac{\partial u_{i\theta}}{\partial \theta} + \frac{u_{i\theta}}{r} \frac{\partial n_e}{\partial \theta} + n_e \frac{\partial u_{iz}}{\partial z} + u_{iz} \frac{\partial n_e}{\partial z} \quad (3.45e)$$

and

$$\begin{aligned}
f(n_e, T_e, \mu_\perp, v_{en}, \omega_{ce}) = & \frac{k_B T_e \mu_\perp}{er^2 n_e} \left(\frac{\partial n_e}{\partial \theta} \right)^2 + \frac{k_B T_e \mu_\perp}{en_e} \left(\frac{\partial n_e}{\partial z} \right)^2 \\
& + \frac{n_e k_B T_e}{er^2} \left[\frac{1}{n_e} \frac{\partial \mu_\perp}{\partial \theta} \frac{\partial n_e}{\partial \theta} + \frac{\mu_\perp}{n_e^2} \left(n_e \frac{\partial^2 n_e}{\partial \theta^2} - \left(\frac{\partial n_e}{\partial \theta} \right)^2 \right) \right] \\
& + \frac{n_e k_B T_e}{e} \left[\frac{1}{n_e} \frac{\partial \mu_\perp}{\partial z} \frac{\partial n_e}{\partial z} + \frac{\mu_\perp}{n_e^2} \left(n_e \frac{\partial^2 n_e}{\partial z^2} - \left(\frac{\partial n_e}{\partial z} \right)^2 \right) \right] \\
& - \frac{k_B T_e}{er B_r} \frac{\partial}{\partial \theta} \left(\frac{1}{1 + \left(\frac{v_{en}}{\omega_{ce}} \right)^2} \right) \frac{\partial n_e}{\partial z} \\
& + \frac{k_B T_e}{er B_r} \frac{\partial}{\partial z} \left(\frac{1}{1 + \left(\frac{v_{en}}{\omega_{ce}} \right)^2} \right) \frac{\partial n_e}{\partial \theta} \\
& - \frac{n_e k_B}{er B_r} \frac{\partial}{\partial \theta} \left(\frac{1}{1 + \left(\frac{v_{en}}{\omega_{ce}} \right)^2} \right) \frac{\partial T_e}{\partial z} + 2 \frac{k_B \mu_\perp}{e} \frac{\partial T_e}{\partial z} \frac{\partial n_e}{\partial z} \\
& - \frac{1}{1 + \left(\frac{v_{en}}{\omega_{ce}} \right)^2} \frac{k_B T_e}{er B_r^2} \frac{\partial B_r}{\partial z} \frac{\partial n_e}{\partial \theta} \tag{3.46}
\end{aligned}$$

$$+ \frac{n_e k_B}{e} \frac{\partial \mu_\perp}{\partial z} \frac{\partial T_e}{\partial z} + \frac{n_e k_B \mu_\perp}{e} \frac{\partial^2 T_e}{\partial z^2} \tag{3.47}$$

The electric potential equation (Eqn. 3.44) and the simplified electron temperature equation (Eqn. 3.41d) form a system of 2 equations, with 2 unknowns: ϕ and T_e . These are the 2 equations that will be solved numerically by the simulation.

3.5.5 Summary of Fluid Equations for Numerical Solution

The following system of 2 equations will be solved numerically for the electron temperature T_e and the electric potential ϕ , respectively:

$$\frac{3}{2} n_e k_B \frac{\partial T_e}{\partial t} = \dot{E}_{convect} + \dot{E}_{compress} + \dot{E}_{diffuse} + S_{joule} + S_{ioniz} \tag{3.48a}$$

$$A_1 \frac{\partial^2 \phi}{\partial \theta^2} + A_2 \frac{\partial \phi}{\partial \theta} + A_3 \frac{\partial^2 \phi}{\partial z^2} + A_4 \frac{\partial \phi}{\partial z} + A_5 = 0 \quad (3.48b)$$

The coefficients $\{A_1, A_2, \dots, A_5\}$ in Eqn. 3.48b are as described in Sect. 3.5.4.3, and we use the simplified forms, based on the 1D electron temperature assumption $T_e = T_e(z, t)$, for the right-hand side terms in Eqn. 3.48a:

$$\dot{E}_{convect} = -\frac{3}{2} n_e k_B u_{ez} \frac{\partial T_e}{\partial z} \quad (3.49a)$$

$$\dot{E}_{compress} = -n_e k_B T_e \left(\frac{\partial u_{ez}}{\partial z} + \frac{1}{r} \frac{\partial u_{e\theta}}{\partial \theta} \right) \quad (3.49b)$$

$$\dot{E}_{diffuse} = \frac{5}{2} \frac{k_B^2}{e} \left[\mu_{\perp} T_e \frac{\partial n_e}{\partial z} \frac{\partial T_e}{\partial z} + n_e \mu_{\perp} \left(\frac{\partial T_e}{\partial z} \right)^2 + n_e \mu_{\perp} T_e \frac{\partial^2 T_e}{\partial z^2} + n_e T_e \frac{\partial T_e}{\partial z} \frac{\partial \mu_{\perp}}{\partial z} \right] \quad (3.49c)$$

$$S_{joule} = m_e n_e v_{en} (u_{ez}^2 + u_{e\theta}^2) \quad (3.49d)$$

$$S_{ioniz} = -\gamma \dot{n}_e k_B E_i - \dot{n}_e \frac{3}{2} k_B T_e \quad (3.49e)$$

After solving numerically for the electric potential ϕ , we can obtain the electric field components,

$$E_z = -\frac{\partial \phi}{\partial z} \quad (3.50a)$$

$$E_{\theta} = -\frac{1}{r} \frac{\partial \phi}{\partial \theta} \quad (3.50b)$$

which we then use to calculate the electron velocities:

$$\begin{aligned}
 u_{ez} = & -\mu_{\perp} E_z - \frac{D_{\perp}}{n_e} \frac{\partial n_e}{\partial z} - \frac{D_{\perp}}{T_e} \frac{\partial T_e}{\partial z} - \frac{1}{1 + \left(\frac{v_{en}}{\omega_{ce}}\right)^2} \frac{E_{\theta}}{B_r} \\
 & - \frac{1}{1 + \left(\frac{v_{en}}{\omega_{ce}}\right)^2} \frac{k_B T_e}{en_e B_r r} \frac{\partial n_e}{\partial \theta}
 \end{aligned} \tag{3.51a}$$

$$\begin{aligned}
 u_{e\theta} = & -\mu_{\perp} E_{\theta} - \frac{D_{\perp}}{n_e r} \frac{\partial n_e}{\partial \theta} + \frac{1}{1 + \left(\frac{v_{en}}{\omega_{ce}}\right)^2} \frac{E_z}{B_r} \\
 & + \frac{1}{1 + \left(\frac{v_{en}}{\omega_{ce}}\right)^2} \frac{k_B T_e}{en_e B_r} \frac{\partial n_e}{\partial z} + \frac{1}{1 + \left(\frac{v_{en}}{\omega_{ce}}\right)^2} \frac{k_B}{e B_r} \frac{\partial T_e}{\partial z}
 \end{aligned} \tag{3.51b}$$

Chapter 4

Numerical Solution Method

In this chapter, we provide a detailed description of the numerical solution methods used to simulate the 2D thruster model described in Chap. 3. We describe the overall simulation process and data flow, including implementation details for both the particle (PIC) and fluid treatments.

4.1 Hybrid Fluid-PIC Approach

4.1.1 Particle-In-Cell Approach

The Particle-In-Cell (PIC) method is a commonly used approach for kinetic (or particle-based) plasma simulations. The basic premise is that particles can assume arbitrary positions within the computational domain; however, certain bulk properties, including forces, are evaluated and calculated only at a set of defined computational grid points. Based on the particle's location within the cell formed by its nearest (i.e., adjacent surrounding) grid points, some means of interpolation is used to assign or project particle properties to the grid representation; likewise, a similar interpolation method is used to apply or distribute quantities that are calculated at the grid points, e.g., calculated forces or fields, to nearby particles. The PIC approach is a computationally efficient means of performing particle-based, i.e., kinetic, simulations of partially-ionized gases, or plasmas. (Dawson, 1962; Birdsall and Langdon, 2005)

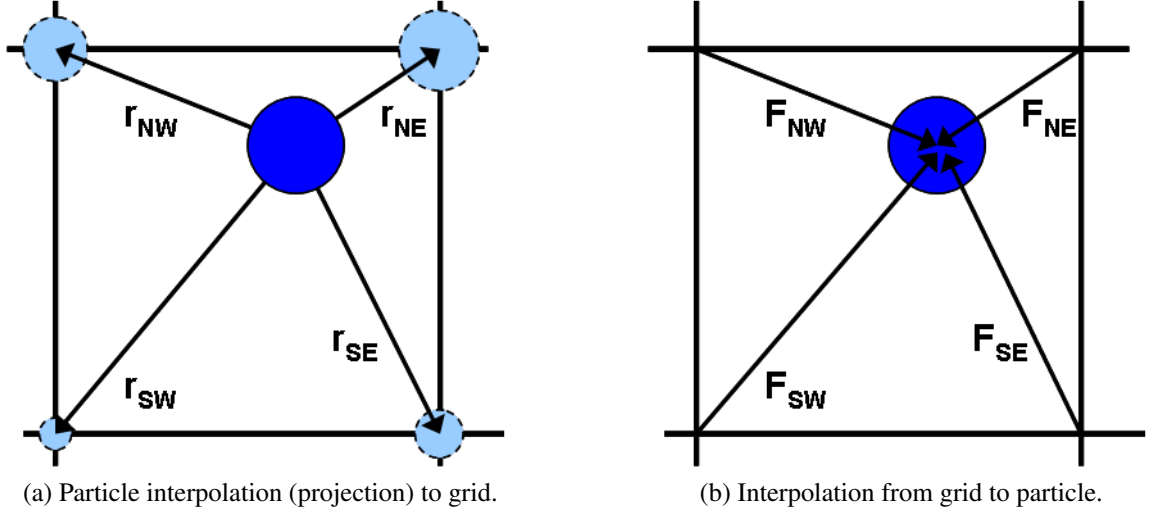


Figure 4.1: Generalized illustration of PIC interpolation.

In this case, we treat the ion and neutral species as discrete superparticles. A superparticle is a single computational (simulated) particle which represents a weighted version or collection of, in this case, individual ion (Xe^+) or neutral (Xe) particles. In our simulations, typical ion and neutral superparticles correspond to $\sim 10^6 \times$ and $\sim 10^{10} \times$ mass-weighted versions, respectively, of an individual ion or neutral particle. For a $10 \times$ weighted superparticle, the superparticle's mass is 10 times that of a physical Xe or Xe^+ particle, i.e., $m_{\text{simulated}} = 10m_{\text{Xe}}$. Superparticles are employed (in lieu of individual true physical mass ion and neutral particles) to reduce computational expense.

The ion and neutral superparticles can assume arbitrary locations within the 2D z - θ computational domain. Each superparticle is interpolated to the grid by projecting or apportioning the superparticle's mass to its nearest (surrounding) four grid points, as shown in Fig. 4.1a. By projecting, or counting, each ion or neutral superparticle's mass contribution to its surrounding grid points, we can compute the interpolated (cumulative) ion or neutral mass or number density at each grid point.

We use a bilinear interpolation, or first-order PIC weighting scheme, to interpolate from each particle to the grid. Consider a single superparticle, denoted as particle k (i.e., numbered as the k^{th} particle). The superparticle has an arbitrary z - θ location (z_k, θ_k) , which falls within the interval $z_i \leq z_k < z_{i+1}$ and $\theta_j \leq \theta_k < \theta_{j+1}$, where z_i , z_{i+1} , θ_j , and θ_{j+1} are

the z - and θ - locations, respectively, of the nearest 4 grid points (z_i, θ_j) , (z_{i+1}, θ_j) , (z_i, θ_{j+1}) , and (z_{i+1}, θ_{j+1}) that surround the superparticle k . We calculate the bilinear interpolation weights

$$W_{k,i,j} = \frac{(z_{i+1} - z_k)(\theta_{j+1} - \theta_k)}{\Delta z \Delta \theta} \quad (4.1a)$$

$$W_{k,i+1,j} = \frac{(z_k - z_i)(\theta_{j+1} - \theta_k)}{\Delta z \Delta \theta} \quad (4.1b)$$

$$W_{k,i,j+1} = \frac{(z_{i+1} - z_k)(\theta_k - \theta_j)}{\Delta z \Delta \theta} \quad (4.1c)$$

$$W_{k,i+1,j+1} = \frac{(z_k - z_i)(\theta_k - \theta_j)}{\Delta z \Delta \theta} \quad (4.1d)$$

where

$$\Delta z = z_{i+1} - z_i \quad (4.2a)$$

$$\Delta \theta = \theta_{j+1} - \theta_j \quad (4.2b)$$

The superparticle k represents a collection of individual true mass Xe particles, such that

$$m_k = \eta_k m_{Xe} \quad (4.3a)$$

or, in the case of ions,

$$m_k = \eta_k m_{Xe+} \quad (4.3b)$$

where m_k is the simulated superparticle mass (for particle k) and η_k is a multiplicative (superparticle multiplier) factor which can assume real number (non-integer) values. For neutrals, typical values are in the range $\eta \simeq 10^9 - 10^{11}$, with an average (mean value) $\eta_{n,avg} \simeq 10^{10}$, for a simulation with approximately 400,000 total neutral superparticles in the computational domain; for ions, typical values are in the range $\eta \simeq 10^3 - 10^7$, with an

average (mean value) $\eta_{n,avg} \simeq 10^6$, for a simulation with approximately 2 million total ion superparticles in the computational domain.

To calculate the number density n at a particular point, we consider

$$n = \frac{N_{particles}}{V} \quad (4.4)$$

where V is the representative unit volume. We can calculate the contribution of a single superparticle k to the number density at each of its surrounding grid points:

$$nContr_{k,i,j} = W_{k,i,j} \frac{\eta_k}{V_{cell,i,j}} \quad (4.5a)$$

$$nContr_{k,i+1,j} = W_{k,i+1,j} \frac{\eta_k}{V_{cell,i+1,j}} \quad (4.5b)$$

$$nContr_{k,i,j+1} = W_{k,i,j+1} \frac{\eta_k}{V_{cell,i,j+1}} \quad (4.5c)$$

$$nContr_{k,i+1,j+1} = W_{k,i+1,j+1} \frac{\eta_k}{V_{cell,i+1,j+1}} \quad (4.5d)$$

where V_{cell} denotes the representative cell volume, e.g., at the grid point (z_i, θ_j)

$$V_{cell,i,j} = \frac{(r_{outer}^2 - r_{inner}^2)}{2} (z_{i+1/2} - z_{i-1/2}) (\theta_{j+1/2} - \theta_{j-1/2}) \quad (4.6)$$

To find the number density at grid point (z_i, θ_j) , we consider sum the contributions of all nearby superparticles, i.e., particles adjacent to that grid point.

$$n_{i,j} = \sum_k nContr_{k,i,j} \quad (4.7)$$

$$z_{i-1} \leq z_k < z_{i+1}$$

$$\theta_{j-1} \leq \theta_k < \theta_{j+1}$$

In a similar manner, we can find the (local population average) ion and neutral species velocities at the grid points. For a single superparticle k (ion or neutral), we can calculate

the particle's velocity contribution to the average (or cumulative) species velocity at each of its surrounding grid points:

$$vContr_{k,i,j} = W_{k,i,j} \eta_k v_k \quad (4.8a)$$

$$vContr_{k,i+1,j} = W_{k,i+1,j} \eta_k v_k \quad (4.8b)$$

$$vContr_{k,i,j+1} = W_{k,i,j+1} \eta_k v_k \quad (4.8c)$$

$$vContr_{k,i+1,j+1} = W_{k,i+1,j+1} \eta_k v_k \quad (4.8d)$$

To find the species velocity, e.g., neutral velocity u_n , at grid point (z_i, θ_j) , we sum the contributions of all nearby neutral superparticles (particles adjacent to that grid point),

$$u_{n,i,j} = \frac{1}{N_{i,j}} \sum_{\substack{\text{neutrals } k \\ z_{i-1} \leq z_k < z_{i+1} \\ \theta_{j-1} \leq \theta_j < \theta_{j+1}}} vContr_{k,i,j} \quad (4.9)$$

normalizing for the (typically, non-integer) number of neutral particles $N_{i,j}$ that contribute to the neutral velocity (i.e., the number of particles counted) at grid point (z_i, θ_j)

$$N_{i,j} = \sum_{\substack{\text{neutrals } k \\ z_{i-1} \leq z_k < z_{i+1} \\ \theta_{j-1} \leq \theta_j < \theta_{j+1}}} W_{k,i,j} \eta_k \quad (4.10)$$

The plasma and electromagnetic properties, including the electric field and corresponding electrostatic (simplified Lorentz) force are calculated only at the grid points. To find the force and corresponding acceleration that govern the motion of an individual superparticle, we consider the calculated force at that superparticle's nearest (surrounding) four grid points and interpolate the corresponding force contribution from the grid to the individual superparticle, as illustrated in Fig. 4.1b.

Consider an ion superparticle, denoted particle k ; we are interested in the acceleration, due to the force that acts on particle k . As described in Sect. 3.4, the ion motion is governed by the simplified (non-magnetized) Lorentz force, i.e., by the electric field at particle k .

$$\mathbf{a}_k = \frac{\mathbf{F}_k}{m_i} = \frac{e}{m_{Xe^+}} \mathbf{E}_k \quad (4.11)$$

where $e = 1.6 \times 10^{-19}$ C is the elemental electron charge, $m_i = m_{Xe^+}$ is the individual Xe^+ ion (true physical) mass, and $\mathbf{E}_k = E_{kz}\hat{z} + E_{k\theta}\hat{\theta}$ is the electric field vector at particle k .

We use a bilinear interpolation scheme to interpolate the electric field from the particle to the grid. For a particle k at location (z_k, θ_k) which falls within the interval $z_i \leq z_k < z_{i+1}$ and $\theta_j \leq \theta_k < \theta_{j+1}$, the bilinear interpolation weights are the same as before:

$$W_{k,i,j} = \frac{(z_{i+1} - z_k)(\theta_{j+1} - \theta_k)}{\Delta z \Delta \theta} \quad (4.12a)$$

$$W_{k,i+1,j} = \frac{(z_k - z_i)(\theta_{j+1} - \theta_k)}{\Delta z \Delta \theta} \quad (4.12b)$$

$$W_{k,i,j+1} = \frac{(z_{i+1} - z_k)(\theta_k - \theta_j)}{\Delta z \Delta \theta} \quad (4.12c)$$

$$W_{k,i+1,j+1} = \frac{(z_k - z_i)(\theta_k - \theta_j)}{\Delta z \Delta \theta} \quad (4.12d)$$

Using this bilinear weighting scheme, we can calculate the electric field at particle location (z_k, θ_k) from the simulated electric field values at each of the surrounding 4 grid points (z_i, θ_j) , (z_{i+1}, θ_j) , (z_i, θ_{j+1}) , and (z_{i+1}, θ_{j+1}) :

$$\mathbf{E}_k = W_{k,i,j} \mathbf{E}_{i,j} + W_{k,i+1,j} \mathbf{E}_{i+1,j} + W_{k,i,j+1} \mathbf{E}_{i,j+1} + W_{k,i+1,j+1} \mathbf{E}_{i+1,j+1} \quad (4.13)$$

The use of superparticles (or macroparticles), in lieu of individual true physical mass particles, means that we are using a reduced set, or number, of particles to represent the true (realistic physical) phase space distribution of the physical ion and neutral species. The simulation is a discretely sampled representation of the underlying local phase space

distribution of each species. This sampled approach requires a sufficient number of simulated particles for adequate statistical representation of the sampled population. As we interpolate from the particles to the grid, we are interested in the validity and adequacy of the PIC grid quantities; this requires a sufficient number of particles per cell to assure that the interpolated grid quantities are not too discontinuous and that they adequately represent the simulated (sampled) species populations.

There is inherent noise and discontinuity associated with the use of discrete superparticles, i.e., a kinetic approach, e.g., compared to a fluid continuum approach. To some degree, the associated numerical, or particle, noise is a desired, or even required, feature of the PIC simulation. The simulated motion, or time advancement, of discrete, discontinuous particles enables the simulation of certain inherently noisy or statistical kinetic processes, e.g., collisional (impact) ionization, kinetic heating, and plasma fluctuations including unsteady wave modes that we seek to model. In some cases, the numerical noise serves to offset numerical damping or dissipation that is an artifact of our broader simulation approach (i.e., the result of certain simplifying assumptions/approximations or the consequence of the electron fluid treatment implementation). However, we must take care that the simulation does not become dominated or solely driven by the numerical noise; the PIC treatment (interpolation to the grid) has a mitigating effect, in this regard, as can increasing the number of simulated particles, which reduces the level of discontinuity.

In general, it is desirable to maximize the number of simulated particles; however, doing so significantly increases the computational expense, in both calculation time and memory storage and access time requirements. Generally, we strike a compromise between maximizing the number of particles, to improve statistical validity and mitigate numerical noise and discontinuity, and minimizing computational expense.

4.1.2 Coupled Fluid-PIC Treatment

The assumption of space charge neutrality, or quasineutrality, is the mechanism by which we couple the fluid treatment (for the electrons) and the PIC approach (for the ions and neutrals). Specifically, we enforce the condition:

$$n_e = n_i \quad (4.14)$$

We use the same numerical grid for both electron fluid discretization and the PIC grid. Per the PIC treatment, we calculate the (interpolated) ion number density at the PIC grid points; we then use this ion number density n_i as the electron number density n_e , as needed for the electron fluid calculations.

$$n_{eFluid} \equiv n_{iPIC} \quad (4.15)$$

4.2 Simulation Process (Numerical Solution Algorithm)

Figure 4.2 illustrates the overall the numerical simulation process. The simulation employs here are two distinct time steps: dt and dt_{sub} . The outer loop of the simulation, which includes the time advancement of the PIC species and the electric field (or electric potential) solution, is time advanced at the larger time step $dt = N_{sub}dt_{sub}$. The smaller time step dt_{sub} is used only for the inner loop time advancement of the electron temperature. The inner loop (electron time advancement) is executed N_{sub} times per single outer loop execution. $N_{sub} = \frac{dt}{dt_{sub}}$ is an integer value simulation parameter used to prescribe the ratio between the outer and inner loop time steps. Here, we describe each step in the simulation process, including numerical solution details.

4.2.1 Particle Motion

The simulation cycle begins with the time advancement of the particle motion according to the outer loop time step dt . We use the leapfrog integration method for the time advancement of the particle positions and velocities. The leapfrog method is a common choice for the particle push, or time advancement of the particle motion, in PIC simulations, primarily due to its computational efficiency. Leapfrog integration requires a minimal set of operations per integration calculation and imposes minimal memory storage requirements. Despite its simplicity and low computational expense, the leapfrog method is acceptably stable and accurate (with an appropriate choice of time step).

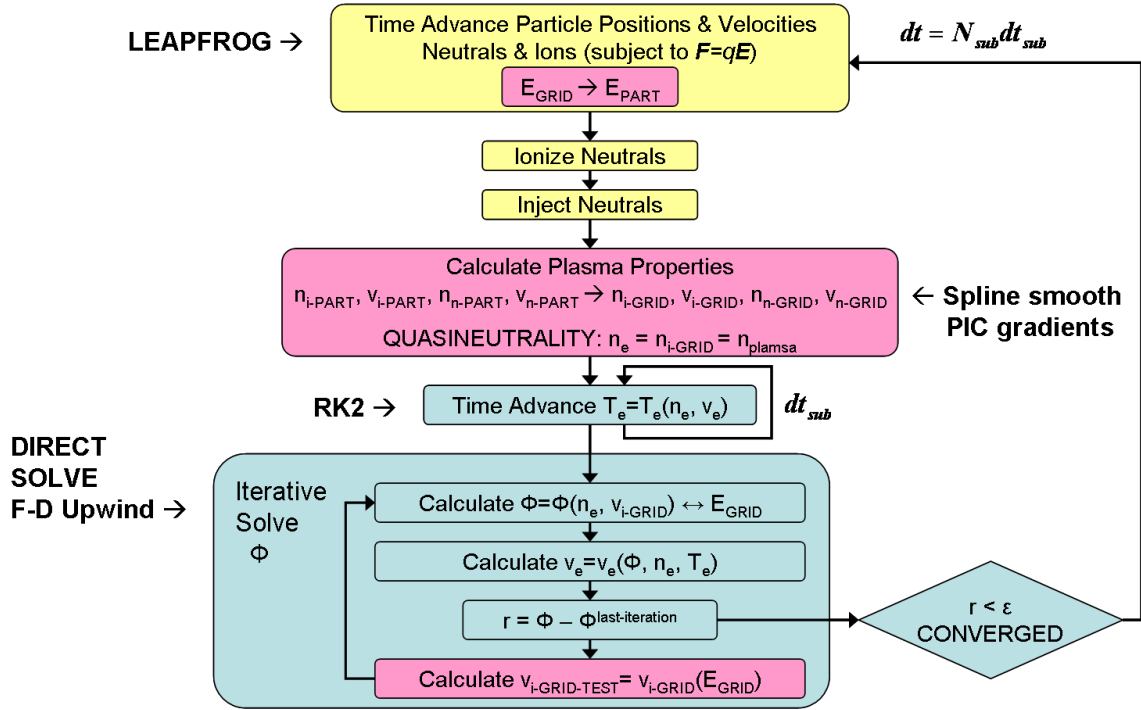


Figure 4.2: Simulation process flowchart.

The leapfrog integration method is applied to the particle equations of motion described in Sect. 3.4. In the case of the neutrals, there is no force (i.e., no acceleration) acting on the neutral particles; the particle velocities v_{nz} and $v_{n\theta}$ are thus constant, and we advance only the particle positions z and θ according to Eqns. 3.7a and 3.7b. In the case of the ions, the ion particle motion is subject to the locally computed electric field according to Eqns. 3.6a and 3.6b. For each ion particle, the electric field is interpolated from the PIC grid to the particle's location as described in Sect. 4.1.1.

Per the leapfrog treatment, the particle positions and acceleration components (due to the electric field in the case of the ions) are known and calculated at whole time steps, while

the particle velocities are calculated at half time steps. At time step n , we time advance the particle velocities for the ions

$$v_z^{n+1/2} = v_z(t_{n-1/2} + dt) = v_z^{n-1/2} + \frac{e}{m_i} E_z^n dt \quad (4.16a)$$

$$v_\theta^{n+1/2} = v_\theta(t_{n-1/2} + dt) = v_\theta^{n-1/2} + \frac{e}{m_i} E_\theta^n dt \quad (4.16b)$$

and the particle positions for both the neutrals and ions

$$z^{n+1} = z(t_n + dt) = z^n + v_z^{n+1/2} dt \quad (4.17a)$$

$$\theta^{n+1} = \theta(t_n + dt) = \theta^n + v_\theta^{n+1/2} dt \quad (4.17b)$$

4.2.2 Ionization

Neutral particles are ionized via a Monte Carlo sampling process according to the local ionization rate described by Eqn. 3.8. To calculate the ionization rate for a given cell, we calculate the ionization rate at each of the 4 surrounding grid points (z_i, θ_j) , (z_{i+1}, θ_j) , (z_i, θ_{j+1}) , and (z_{i+1}, θ_{j+1}) that comprise (border) the cell, using the PIC grid and fluid properties calculated during the previous time step cycle t_n ; we then average, i.e., take the arithmetic mean of, the ionization rates for the 4 grid points to find the local (average) ionization rate within the cell. We determine the number of superparticles per cell that will be ionized, according to the prescribed simulation parameters and the number of particles presently within the cell. In cases where the number of ion superparticles within a given cell is low, we ionize more neutral particles to create more ion particles in that cell. We then use a pseudo-random variable (pseudo-random number generator) to determine which specific particles within the cell will be ionized.

Once a neutral particle is selected for ionization, we create a corresponding new ion superparticle with mass

$$m_{i,new} = \frac{1}{N_{ipc}} \dot{n}_{e,cell} V_{cell} m_{Xe^+} dt$$

where N_{ipc} is the number of neutral superparticles ionized for that cell, $\dot{n}_{e,cell}$ is the ionization rate (averaged from the 4 surrounding grid points) for that cell, and V_{cell} is the cell volume described by Eqn. 4.6. The newly created ion particle assumes the same position and velocity as the original neutral particle (i.e., the neutral particle from which it was ionized).

To assure mass conservation, we must also adjust the mass of the neutral superparticles accordingly. While only certain neutral particles, selected by the Monte Carlo sampling process, are used to create new ion particles, we subtract the corresponding ionized mass equally from all neutral particles within the cell. For each neutral particle in the cell, we adjust the particle's mass to account for the neutral mass lost to ionization (on a per cell basis):

$$m_{n,updated} = m_n - \frac{1}{N_{npc}} \dot{n}_{e,cell} V_{cell} m_{Xe^+} dt$$

where N_{npc} is the total number of neutral superparticles in that cell. Typically, $N_{ipc} \ll N_{npc}$.

4.2.3 Neutral Injection

We inject neutral particles from the anode plane according to the prescribed neutral gas mass flow rate. At each time step dt (outer loop simulation cycle), we inject a specified number of neutral superparticles, as specified by the simulation parameters. The total neutral mass injected per time step dt is determined by the prescribed mass flow rate \dot{m}_n . We prescribe the mass of each injected superparticle

$$m_{n,inject} = \frac{1}{N_{inject}} \dot{m}_n dt$$

where N_{inject} is the number of neutral particles injected per outer loop simulation cycle. Typically, $N_{inject} = 1$ or 2 .

We introduce the injected neutral particles just inside the domain at the z -location $z = 0.01$ nm. We give each injected neutral particle a random θ -location, sampled from a uniform distribution over the range $\theta = 0 - 2\pi$ radians using a pseudo-random variable (pseudo-random number generator).

The velocity of each injected neutral particle is sampled from the distributions described in Sect. 3.3 and Appendix A. The one-way flux distribution for the z -velocity of the injected neutral particles is inverted by a Monte Carlo sampling process. Likewise, the θ -velocity of each injected neutral particle is obtained by sampling the velocity in the r - θ plane (i.e., inverting the relevant speed and planar velocity orientation distributions) and projecting that velocity onto particle's $\hat{\theta}$ -direction as described in Appendix A, using the randomly determined (sampled) θ -position for that particle. Details of the distribution inversion, or sampling, procedure can be found in Birdsall and Langdon (2005) or Scharfe (2009). The distribution inversion, or sampling, is performed a priori and the values are tabulated in a file; during the simulation, the sampled velocity values are read in from the file.

4.2.4 PIC Interpolation and Smoothing

As described in Sect. 4.1.1, we interpolate the particle properties (from the particle locations) to the grid to obtain the PIC grid quantities that will be used, in the subsequent steps, to find the electron temperature and electric potential solutions.

To mitigate the numerically destabilizing effect of strong spatial gradients due to the PIC treatment (i.e., particle noise or discontinuities due to the particle treatment), we apply a two-dimensional smoothing spline, described by Shikin and Plis (1995), to the PIC quantities – specifically, the neutral density n_n , ion or electron density n_e , and the ion velocities u_{iz} and $u_{i\theta}$ – prior to taking their derivatives or using these quantities in the v_{en} calculation; this smoothing applies only to cases in which we take spatial derivatives, e.g., we spatially spline smooth n_e prior to taking any spatial derivatives $\frac{\partial n_e}{\partial z}$ or $\frac{\partial n_e}{\partial \theta}$ or higher order derivatives. With the exception of the v_{en} calculation, in all other calculations that require the actual quantity, e.g., when the quantity n_e appears in the electron temperature or electric potential equations, we use the unsmoothed PIC quantity.

In addition to using the updated PIC quantities n_n , u_{iz} and $u_{i\theta}$, we impose quasineutrality and use the PIC-calculated ion density as the plasma, or electron, density n_e in the subsequent electron fluid calculations – thus, linking the PIC and electron fluid treatments, as discussed in Sect. 4.1.2.

4.2.5 Time Advancement of Electron Temperature

We next perform the inner loop time advancement of the electron temperature. We use the smaller time step $dt_{sub} = \frac{dt}{N_{sub}}$ for each inner loop simulation cycle, i.e., each time advancement of the electron temperature. The time advancement of the electron temperature T_e is performed N_{sub} times, in succession, per outer loop simulation cycle (i.e., the inner loop is executed N_{sub} times per outer loop simulation cycle).

During each inner loop simulation cycle, we numerically solve the electron energy, or electron temperature, equation 3.48a. Specifically, we rewrite Eqn. 3.48a in the form

$$\frac{dT_e}{dt} = f(t, T_e) \quad (4.18)$$

which will allow us to time advance, or numerically integrate, the electron temperature T_e .

For the spatial discretization of the (spatial) derivative terms, we use a central difference scheme for both the first and second spatial derivatives where possible within the domain (i.e., everywhere except the boundary points); for both the first and second spatial derivatives, we apply a two-point forward or backward difference at the upstream ($z = 0$) and downstream ($z = 0.12$ m) boundaries, respectively. As will be discussed in Sect. 4.3.2, the grid spacing is uniform in θ ; hence, we use the usual central difference formulas for the first and second spatial derivatives in θ . To find the spatial derivatives with respect to θ at grid points (z_i, θ_j) , we use the following discretization:

$$\frac{dg_{i,j}}{d\theta} = \frac{g_{i,j+1} - g_{i,j-1}}{2\Delta\theta} \quad (4.19)$$

$$\frac{d^2g_{i,j}}{d\theta^2} = \frac{g_{i,j+1} - 2g_{i,j} + g_{i,j-1}}{(\Delta\theta)^2} \quad (4.20)$$

In the z -direction, we sometimes use a non-uniform grid; in that case, we use a central difference scheme for the first spatial derivative in z that is weighted based on proximity or “nearness” (i.e., the point closer to the point of interest z_i is weighted more heavily in the derivative calculation):

$$\frac{df_{i,j}}{dz} = (f_{i+1,j} - f_{i,j}) \frac{(z_i - z_{i-1})}{(z_{i+1} - z_i)(z_{i+1} - z_{i-1})} + (f_{i,j} - f_{i-1,j}) \frac{(z_{i+1} - z_i)}{(z_i - z_{i-1})(z_{i+1} - z_{i-1})} \quad (4.21)$$

For the second derivative in z , we use the typical central difference formula for a non-uniform grid:

$$\frac{d^2 f_{i,j}}{dz^2} = \frac{2(f_{i+1,j} - f_{i,j})}{(z_{i+1} - z_i)(z_{i+1} - z_{i-1})} + \frac{2(f_{i-1,j} - f_{i,j})}{(z_i - z_{i-1})(z_{i+1} - z_{i-1})} \quad (4.22)$$

The non-uniform discretization formulas are derived from Hirsch (1988). For both the first derivative (Eqn. 4.21) and the second derivative (Eqn. 4.22) formulas, the discretization is second-order accurate for uniform or nearly uniform grid spacing; if the grid is highly nonuniform, e.g., if $z_i - z_{i-1} \ll z_{i+1} - z_i$, the accuracy is reduced.

For the time advancement of the electron temperature $T_e(z, t)$, we use a second-order Runge Kutta method (RK2). As discussed in Sect. 3.5.3, we assume the electron temperature is 1D in z . We implement this quasi-1D electron temperature solution by first calculating the right hand side of Eqn. 4.18 for all points in the 2D z - θ grid (i.e., all for all z and all θ) according to the spatially discretized versions of Eqns. 3.48a and 3.49a-3.49e; we then take the azimuthal average (i.e., average over all θ) for each z -location z_i to find the right hand side of the 1D version of Eqn. 4.18 where $T_e = T_e(z, t)$. Using this 1D version of Eqn. 4.18, we time advance the electron temperature $T_e(z, t)$ according to the second-order Runge Kutta scheme:

$$T_e^{*m+1/2} = T_e^m + \frac{dt_{sub}}{2} f(t_m, T_e^m) \quad (4.23)$$

$$T_e^{m+1} = T_e^m + dt_{sub} f(t_{m+1/2}, T_e^{*m+1/2}) \quad (4.24)$$

described in Moin (2001), where $f(t_m, T_e^m)$ is described by Eqn. 4.18.

To mitigate the numerically destabilizing effect of rapid temporal fluctuations in the electron temperature, we limit the change in the electron temperature $\Delta T = |T_e^{m+1} - T_e^m|$ at

each axial location z . We impose a maximum change $\Delta T_{e,max}$ per inner loop (electron temperature) time step dt_{sub} ; if $\Delta T_e > \Delta T_{e,max}$ (for T_e^{m+1} based on the RK2 time advancement), then we artificially set the electron temperature, at that point z , to $T_e^{m+1} = T_e^m \pm \Delta T_{e,max}$. $\Delta T_{e,max}$ is prescribed as a simulation parameter; for $dt_{sub} = 0.1$ ns, we typically use a value of $\Delta T_{e,max} = 10$ K, resulting in a maximum change $\frac{\Delta T_{e,max}}{dt_{sub}} = \frac{10\text{K}}{0.1\text{ns}}$.

To further assure that the electron temperature remains bounded within the operational (experimentally-observed) electron temperature range, we enforce minimum and maximum values $T_{e,min}$ and $T_{e,max}$, respectively, for the electron temperature throughout the domain. If the calculated electron temperature, per the RK2 time advancement, exceeds these bounds, we artificially set the electron temperature, at that point z , to $T_{e,min}$ or $T_{e,max}$, as appropriate. $T_{e,min}$ and $T_{e,max}$ are prescribed as simulation parameters, based on the prescribed operating voltage; higher operating voltages warrant a higher maximum temperature condition $T_{e,max}$. We typically prescribe $T_{e,max}$ based on the experimentally-measured peak electron temperature for the given operating voltage; for low voltage simulations (e.g., the representative case which will be presented in Chap. 5), the electron temperature typically does not exceed the prescribed maximum value $T_{e,max}$, i.e., no correction to the electron temperature value is required based on the maximum temperature upper bound. For the lower bound, we typically use a value of $T_{e,min} = 15,000$ K (~ 1.3 eV), regardless of operating voltage; in typical low voltage simulations, the time advanced electron temperature occasionally falls below this minimum value and must be artificially corrected.

After performing the electron temperature time advancement, we can calculate the updated electron velocities u_{ez} and $u_{e\theta}$ according to Eqns. 3.51a and 3.51b, using the updated electron temperature T_e .

We repeat this process for each inner loop cycle with the time step dt_{sub} ; the inner loop time advancement is successively executed N_{sub} times, resulting in a total time advancement $dt = N_{sub}dt_{sub}$ of the 1D electron temperature $T_e(z, t)$.

4.2.6 Iterative Solution for Electric Potential

The final step in the outer loop simulation cycle is the calculation of the electric potential ϕ , according to Eqn. 3.48b. In solving for the electric potential ϕ , and the resulting electric

fields E_z and E_θ , we assume that the modeled plasma discharge is in a quasi-steady-state at time $t = t^{n+1} = t^n + dt$ (as calculated during the n^{th} outer loop simulation cycle); we then perform an electrostatic solution for the resulting electric potential ϕ (and corresponding electric fields) at that moment in time $t = t^{n+1}$. Note that we do not time advance the electric potential, per se; instead, we calculate the electrostatic solution based on the particular set of system conditions, or plasma properties, at that given moment in time $t = t^{n+1}$.

The final solution value for ϕ is found by an iterative process. At each step (iteration) in the solution process, we perform a direct solution for ϕ , based on certain calculated properties (which are dependent on ϕ); we then update these properties, based on the most recent ϕ value (from the previous iteration), and calculate a new solution for ϕ . We iterate successively in this manner until the value of ϕ has converged, as determined by a tolerance ε which is set as a simulation parameter.

To find the electric potential ϕ , we must solve Eqn. 3.44. If we examine the coefficients of this equation, as described by Eqns. 3.45a-3.45e and 3.46, we see that ϕ is a function of the plasma properties n_n , n_e , T_e , u_{iz} , and $u_{i\theta}$. The neutral and plasma number densities, n_n and n_e , and the electron temperature T_e are known at time $t = t^{n+1}$ from the previous steps in the (n^{th}) simulation cycle. However, due to the leapfrog staggering for the particle positions and velocities, the PIC-interpolated ion velocities u_{iz} and $u_{i\theta}$ are known only at the half time step $t = t^{n+1/2}$ and are not known the present time $t = t^{n+1}$.

To begin the iterative solution cycle, we make a guess for the ion velocities at time $t = t^{n+1}$. More specifically, we predict, or extrapolate, the ion velocities at time $t = t^{n+1}$ based on the known ion velocities at the previous two half time steps $t = t^{n-1/2}$ and $t = t^{n+1/2}$:

$$u_{iz}^{*n+1} = u_{iz}^*(t = t_{n+1}) = \frac{3}{2}u_{iz}^{n+1/2} + \frac{1}{2}u_{iz}^{n-1/2} \quad (4.25a)$$

$$u_{i\theta}^{*n+1} = u_{i\theta}^*(t = t_{n+1}) = \frac{3}{2}u_{i\theta}^{n+1/2} + \frac{1}{2}u_{i\theta}^{n-1/2} \quad (4.25b)$$

Using this guess for u_{iz}^{*n+1} and $u_{i\theta}^{*n+1}$, we proceed to solve Eqn. 3.48b for ϕ^{*n+1} . We discretize Eqn. 3.48b and its coefficients (Eqns. 3.45a-3.45e and 3.46) using a high-order finite-difference upwind method (with a four-point central difference stencil and $q = 0.5$) described by Fletcher (1991). The method is up to third-order accurate for a uniform grid;

however, for a non-uniform grid as typically used here, the accuracy is reduced. The discretization results in a system of equations of the form

$$A\vec{\phi} = 0 \quad (4.26)$$

where the matrix A is block tridiagonal and the vector $\vec{\phi}$ contains the values of the electric potential $\phi_{i,j}^*$ at all grid points (z_i, θ_j) . We then solve directly for $\vec{\phi}$ using Gauss-Jordan elimination.

After solving for ϕ , we can update other dependent quantities accordingly, using this new value ϕ^{*n+1} . We calculate the electric fields E_z and E_θ , according to Eqns. 3.50a-3.50b, using the same central-difference scheme for the spatial derivatives described in Sect. 4.2.5. We calculate the updated electron velocities u_{ez} and $u_{e\theta}$ according to Eqns. 3.51a-3.51b.

Using the updated electric fields, E_z and E_θ , we can then update the ion velocities u_{iz}^{*n+1} and $u_{i\theta}^{*n+1}$. To do so, we use the newly updated electric field (or ion acceleration terms) E_z^{*n+1} and E_θ^{*n+1} to find the time advanced the particle velocities $v^{*n+3/2}$, which can then be PIC interpolated to the grid to find the ion velocities (at the grid) $u_{iz}^{*n+3/2}$ and $u_{i\theta}^{*n+3/2}$. We then calculate the updated ion velocities for time $t = t^{n+1}$ by averaging the PIC-interpolated ion velocities at times $t = t^{n+1/2}$ and $t = t^{n+3/2}$.

$$u_{iz}^{*n+1} = \frac{1}{2} \left(u_{iz}^{n+1/2} + u_{iz}^{*n+3/2} \right) \quad (4.27a)$$

$$u_{i\theta}^{*n+1} = \frac{1}{2} \left(u_{i\theta}^{n+1/2} + u_{i\theta}^{*n+3/2} \right) \quad (4.27b)$$

Using the updated ion velocities u_{iz}^{*n+1} and $u_{i\theta}^{*n+1}$, we restart the iteration cycle and solve for ϕ , as before. We continue to iterate in this manner – solving for ϕ^* , then updating E_z , E_θ , u_{ez} , $u_{e\theta}$, u_{iz} , and $u_{i\theta}$ – until the value of ϕ^* converges. At each iteration cycle, we calculate the residual

$$r_{i,j} = |\phi_{i,j}^{*new} - \phi_{i,j}^{*prev}| \quad (4.28)$$

at each grid point (z_i, θ_j) . We determine convergence using the simulation parameter ε . If $r_{i,j} > \varepsilon$ for any grid point (z_i, θ_j) , then we continue to iterate, repeating the process described above, until the ϕ solution converges. If $r_{i,j} \leq \varepsilon$ for all grid points (z_i, θ_j) , then the solution has converged; we terminate the iterative solution cycle and store the solution value $\phi^{n+1} = \phi^{*n+1}$ and the resulting updated quantities E_z, E_θ, u_{ez} , and $u_{e\theta}$. We typically use a convergence tolerance of $\varepsilon = 10^{-6}$; using the typical spatial grid and outer loop time step dt described in Sect. 4.3 with the convergence tolerance value $\varepsilon = 10^{-6}$, the potential solution typically converges within 5 iterations.

At this point, we have completed the final step in the outer loop simulation cycle. We then restart the outer loop simulation cycle.

4.3 Numerical Considerations

4.3.1 Time Step

The decision to use distinct time steps for the inner and outer simulation loops was driven by both the governing physics and computational considerations. The disparity in mass between the electrons and the heavy (ion and neutral) species means that the respective electron and heavy species motion occur at significantly different timescales. Relative to the heavy ion and neutral species, the electrons move more quickly, i.e., at faster timescales; while a larger time step is sufficient to resolve the ion and neutral motions, a smaller time step is required to adequately resolve the electron dynamics.

In early simulations, we used a single common time step for both the inner and outer simulation loops; however, this approach proved to be computationally inefficient. In addition to the disparate physical (time and velocity) scales, the electron temperature solution places additional constraints on the electron time step. The electron temperature equation contains several stiff terms (on the right hand side of Eqn. 3.48a) which require a small time step to maintain numerical stability when using an explicit time advancement method, such as RK2. The inner loop simulation structure, and corresponding use of a smaller time step, for the time advancement of T_e was implemented to address this challenge in the numerical solution and stability. (An alternative approach would have been to use a fully

implicit solution method or perform implicit-explicit operator splitting; however, either of these methods would be more computationally expensive than RK2.) While the electron temperature solution requires a small time step, the time step constraint for resolving the ion and neutral particle motion (and the resulting change in the electrostatic solution) is less restrictive. We thus chose to implement the inner-outer simulation loop structure, using a larger time step for the heavy particle motion and electric potential solution and a smaller time step for the electron temperature time advancement. Typical values for the inner and outer loop time steps are $dt_{sub} = 0.1$ ns and $dt = 10$ ns, or $N_{sub} = \frac{dt}{dt_{sub}} = 100$.

In selecting a value for the electron time step dt_{sub} , we seek to resolve the electron cyclotron frequency. The electron cyclotron frequency is maximum in the region of peak magnetic field; for the peak magnetic field strength $B_r = 0.11$ T, the electron cyclotron frequency is approximately 2 rad/s, which corresponds to a timescale $t_{\omega_{ce}} \simeq 3$ ns. Since we assume the plasma is quasineutral, we are not concerned with resolving the plasma frequency $\omega_{pe} = \sqrt{\frac{e^2 n_e}{\epsilon_0 m_e}}$ (where $\epsilon_0 \simeq 8.85 \times 10^{-12}$ F/m is the free space permittivity). For $n_e = 10^{17}$ - 10^{18} m⁻³, the electron plasma frequency is approximately 2.5×10^{10} rad/s, which corresponds to a timescale $t_{\omega_{pe}} \simeq 0.1$ - 0.3 ns. Although dt_{sub} is close to resolving the plasma frequency, this is irrelevant as the quasineutrality assumption prevents the model from predicting Langmuir, or plasma, oscillations.

The outer loop time step $dt = 10$ ns does not quite resolve the electron cyclotron motion. However, in the outer loop simulation cycle, we are concerned with resolving the ion and neutral particle motion and finding the corresponding change in the electric potential due the resulting changes in the electrostatic system conditions. The constraint on the time step for the particle time advancement is determined by the particle velocities and the grid spacing. To mitigate discontinuity and assure validity of the PIC treatment, we must select a time step that is small enough to prevent a particle from skipping a cell, i.e., traversing a distance larger than one cell (in either the z - or θ -direction), in a single time step.

We perform the electric potential solution according to the outer loop time step dt . To find the electric potential solution, we assume that the system has equilibrated to a quasi-steady-state. We do not perform the electric potential solution for each inner loop simulation cycle as we do not believe the change in the electron temperature, at that timescale, is significant to the overall electrostatic system conditions; furthermore, we can take the

electric potential and electric fields to be quasi-steady, i.e., constant in time, at the electron timescale dt_{sub} . We instead solve for the electric potential at the outer loop timescale dt since the changes in the electrostatic conditions, due to the particle time advancement and the electron temperature advancement at that timescale $dt = N_{sub}dt_{sub}$, are expected to be significant in characterizing the system state and evolution.

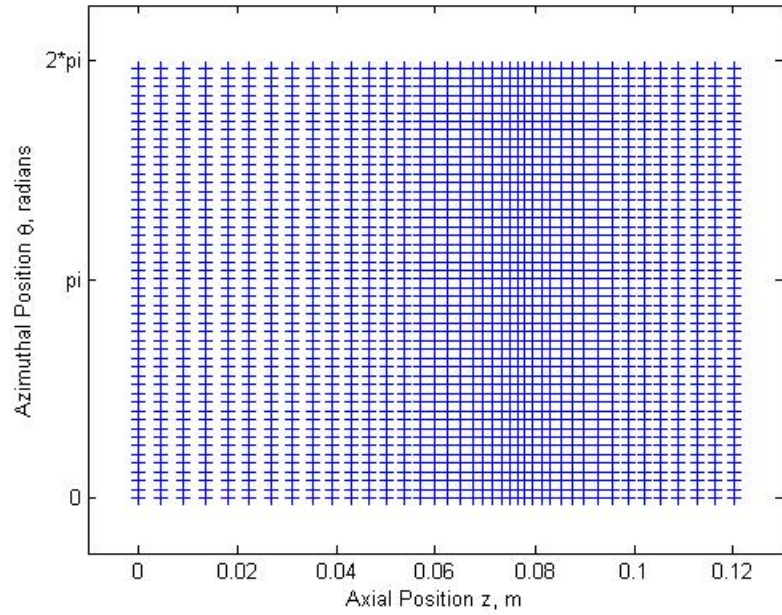
4.3.2 Spatial Resolution

Figure 4.3a shows the typical computational grid employed. The grid contains 40 points in z and 50 points in θ . The grid is non-uniform in z , with additional grid points clustered in the region of peak magnetic field where gradients are expected to be large. Figure 4.3b shows the grid spacing Δz , which ranges from a maximum $\Delta z_{max} = 4.6$ mm near the anode to a minimum $\Delta z_{min} = 1.5$ mm just upstream of the exit plane near the z -location of the peak magnetic field. The grid points are spaced uniformly in θ , with $\Delta\theta = \frac{2\pi}{50} \simeq 0.126$ radians, which corresponds to a distance $r_{mid}\Delta\theta \simeq 5.1$ mm.

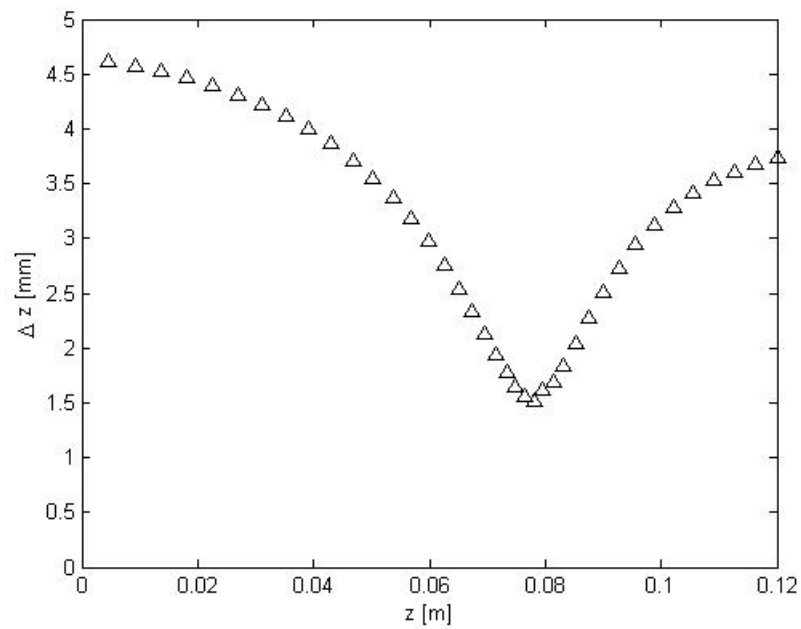
In both directions z and θ , the grid spacing is comparable to the distance between measurement probes in relevant laboratory experiments (Gascon and Cappelli, 2003). With the computational grid shown in Fig. 4.3a, we can resolve disturbances with axial wavelengths as small as $\lambda_z \simeq 10$ mm, even in regions where the grid is coarsest. In the azimuthal direction, we can resolve wavelengths as small as $\lambda_\theta \simeq 10$ mm which corresponds to azimuthal mode numbers up to $m_\theta \simeq 20$. While a finer spatial resolution might allow us to examine smaller length scale phenomena, the spatial resolution shown in Fig. 4.3 (used with the outer loop time step $dt = 10$ ns and inner loop time step $dt_{sub} = 0.1$ ns) is, in most cases, sufficient to resolve the fluctuations of interest, in both the axial and azimuthal directions.

4.3.3 Number of Simulated Particles (Validity of PIC Approach)

A sufficient number of particles per cell is required to mitigate numerical noise and discontinuity in the PIC treatment. Furthermore, increasing the number of simulated particles generally provides better PIC statistics, i.e., a more accurate representation, or statistical sampling, of the underlying statistical kinetic processes.



(a) Numerical grid with 40 points (non-uniform) in z and 50 points (uniform) in θ .



(b) Grid spacing in z -direction.

Figure 4.3: Typical spatial resolution.

In the case of the neutrals, neutral particles are introduced into the domain by the neutral injection process. Neutral particles that exit the domain or that are lost to ionization (i.e., neutral particles whose mass is reduced to zero by the ionization process) deplete the number of neutral particles in the domain. The number of neutral particles can be controlled by adjusting the number of neutral particles N_{inject} that are injected per outer simulation loop. In typical simulations, the total number of neutral superparticles is approximately 400,000, which corresponds to an average of 200 particles per cell.

In the case of the ions, the number of ion particles is continuously and quickly depleted as the ions, accelerated by the axial electric field, exit the domain. The only means of replenishing the ion particle population is ionization; hence, we must adjust the number of ionized particles per cell N_{ipc} (set as a simulation parameter) to sustain a sufficient number of ion superparticles in each cell in the domain. In the case of the ion particles, an insufficient number of particles per cell quickly leads to strong discontinuous gradients, which lead to strong (unphysical) discontinuities and resulting numerical instability in the simulated electric potential and electron temperature. We typically maintain the total number of ion superparticles at approximately 1.5 million to 2.5 million particles, which corresponds to an average of 750 - 1250 particles per cell.

4.3.4 Computational Expense

The computational expense, or total simulation wall clock time, is driven by the grid size (total number of grid points) and the number of particles simulated. While we generally wish to maximize the spatial grid resolution and the number of particles per cell (which correspondingly increases the total number of simulated particles), we must balance these priorities against the computational expense. Likewise, a smaller time step enables finer timescale resolution, but requires more simulation cycles to complete a given extent of simulated time. We strike a practical compromise between these competing factors by choosing a spatial resolution that adequately resolves the spatial phenomena of interest (particularly, the azimuthal fluctuations) and time steps dt and dt_{sub} that resolve the timescales of interest (e.g., the electron cyclotron frequency), but permit sufficiently long simulations.

For the 40 point \times 50 point grid (2000 grid points total) shown in Fig. 4.3, and an approximate total of 400,000 neutral and 2M ion particles, a typical simulation of 20,000 outer loop simulation cycles takes approximately 20 - 24 hours to run on a single Intel Xeon 3.40 GHz processor core. Using an outer loop time step $dt = 10$ ns with $N_{sub} = 100$ (or $dt_{sub} = 0.1$ ns), it takes approximately 100 - 120 hours (approximately 4-5 days) to simulate a total time of 1 ms.

4.4 Boundary Conditions

For the θ -direction, we apply periodic boundary conditions. As discussed in Sect. 3.1, the computational domain spans the full azimuth, and we apply the periodic boundary condition $\theta_0 = 0 = 2\pi$. The computational grid is periodic in θ , and the periodic boundary condition likewise applies to all particle motion and to the discretization of the electric potential (ϕ) equation and quasi-1D electron temperature (T_e) equation.

In the z -direction, we apply mixed boundary conditions (Dirichlet at the upstream, i.e., $z = 0$, boundary and Neumann at the downstream, i.e., $z = 0.12$ m, boundary) for T_e and Dirichlet boundary conditions for ϕ . For the electron temperature $T_e(z)$, we typically prescribe the temperature value at the $z = 0$ (upstream/anode) boundary; for the 100V operating condition, $T_e(z = 0) = 1.5$ eV is a typical value for the upstream Dirichlet boundary condition. At the downstream end of the domain, $z = 0.12$ m, we typically use a zero-slope boundary condition, i.e., $\frac{\partial T_e}{\partial z}(z = 0.12) = 0$.

For the electric potential ϕ , we apply Dirichlet boundary conditions at $z = 0$ and $z = 0.12$ m, according to the prescribed thruster operating voltage. In both cases, the ϕ boundary condition is applied axisymmetrically, i.e., uniformly in θ . Typically, we specify the voltage drop, or electric potential difference, across the thruster. For the 100 V experimental operating condition, the operating voltage is set to 100V at the anode (by an external power supply) and the electric potential at the downstream domain boundary ($z = 0.12$ m, or 4 cm past the channel exit) is measured to be approximately 30V (Hargus, 2001); the resulting electric potential difference between the anode ($z = 0$) and downstream ($z = 0.12$ m) domain end boundary is thus 70 V.

At the anode plane ($z = 0$), we assume the applied voltage, or electric potential, is constant across the plane for all θ . Likewise, at the downstream domain end ($z = 0.12$ m), we assume the electric potential is constant across the plane for all θ . While the Dirichlet boundary condition at the anode is reasonable (the anode is at a fixed voltage), the downstream boundary condition is less clear. Experimental measurements (Smith and Cappelli, 2009) indicate some azimuthal variation in the electric potential outside the thruster (beyond the channel exit in the discharge plume) due to the external electron-emitting cathode (located at a “single point” in θ) and other asymmetries. In imposing an axisymmetric boundary condition for $\phi(z = 0.12m)$, we neglect this asymmetry. We expect that the asymmetry does not significantly affect the plasma properties and fluctuations in the regions of interest inside the thruster channel or in the near plume; furthermore, we observe azimuthal variations in the simulated properties just inside the computational domain (a few cells upstream of the $z = 0.12$ m boundary) – so we do not believe that the axisymmetric boundary condition is significantly or artificially disrupting azimuthal fluctuations or property variations within the computational domain.

Chapter 5

Simulation Results

In this chapter, we present representative simulation results for a low voltage thruster operating condition. While we present only a single simulation case here, similar features, especially with regard to waves and electron transport, have been observed in simulations of other operating conditions (e.g., higher voltage and lower mass flow rate).

5.1 Simulation Conditions

5.1.1 Thruster Operating Condition

The simulated operating conditions were chosen to enable comparisons to low voltage SHT laboratory experiments (Hargus, 2001; Meezan et al., 2001; Meezan, 2002; Gascon and Cappelli, 2003) in which the axial plasma property profiles, effective electron mobility, and dispersive wave characteristics were measured. Table 5.1 describes the simulated operating condition. The voltage at the anode plane is supplied by an external power supply which is set to the prescribed operating voltage of, in this case, 100 V. The electric potential in the near plume region of the discharge, near the external cathode location and the computational domain end, was measured to be approximately 30 V (Hargus, 2001); the result is an electric potential, or voltage, difference of 70 V between the anode plane and the downstream computational boundary, which will be used to set the simulation boundary conditions for the electric potential ϕ .

Table 5.1: Simulated operating condition

Operating Parameter	Value
Xe neutral propellant mass flow rate (\dot{m}_n)	2.3 mg/s
Voltage at anode plane, $z = 0$ (set by external power supply)	100 V
Voltage at cathode plane / “near” plume extent, $z = 0.12$ m (measured)	30 V

In laboratory experiments, Xe neutral gas is supplied to both the anode plate and external cathode, respectively, by independent mass flow controllers. In relevant SHT experiments, the prescribed respective mass flow rates were 2.0 mg/s to the anode plate and 0.3 mg/s to the external cathode, resulting in a total Xe supply rate of 2.3 mg/s (Hargus, 2001; Meezan, 2002). In our simulations, we model the entire the entire neutral mass flow rate at the anode plane, i.e., the total Xe mass flow rate of 2.3 mg/s is supplied (injected into the computational domain) from the anode plane.

5.1.2 Simulation Parameters

Table 5.2 lists the relevant simulation parameters. We use the numerical grid shown in Fig. 4.3a, which contains 40 points non-uniformly spaced in z and 50 points uniformly-spaced in θ , for a total of $40 \times 50 = 2000$ grid points. As discussed in Sect. 4.3.1, we use an outer loop time step $dt = 10$ ns with $N_{sub} = \frac{dt}{dt_{sub}} = 100$, which results in an inner loop time step $dt_{sub} = 0.1$ ns. The simulation is time advanced over 190,000 outer loop time steps, which corresponds to 1.9 million inner loop time steps; the total simulated time extent is 1.9 ms of simulated time.

We set the electric potential boundary condition by prescribing the electric potential at the anode, relative to an electric potential of 0 V at the downstream domain boundary. For the 100 V operating condition described by Table 5.1, the electric potential difference between the anode plane (upstream domain boundary at $z = 0$) and the downstream domain boundary ($z = 0.12$ m) is 70V; hence, we prescribe an electric potential boundary condition of 70 V at $z = 0$, relative to an electric potential value (boundary condition) of 0 V at $z = 0.12$ m.

Table 5.2: Summary of simulation parameters

Simulation Parameter	Value	Description
dt	10 ns	Outer loop time step, used for particle time advancement and electric potential solution
$\Delta\phi = \phi_{z=0} - \phi_{z=0.12\text{ m}}$	70 V	Voltage difference between anode and downstream domain boundary, used to set electric potential boundary condition
ϵ	10^{-6}	Convergence tolerance for electrical potential solution
dt_{sub}	0.1 ns	Inner loop timestep, used for electron temperature time advancement
Boundary condition $T_e(z=0)$	$T_e = 17,500\text{ K}$ ($\sim 1.5\text{ eV}$)	Dirichlet boundary condition applied at anode plane
Boundary condition $T_e(z=0.12\text{ m})$	$\frac{\partial T_e}{\partial z} = 0$	Neumann boundary condition applied at downstream domain end
$T_{e,min}$	15,000 K ($\sim 1.3\text{ eV}$)	Enforced minimum electron temperature value throughout domain
$T_{e,max}$	120,000 K ($\sim 10.3\text{ eV}$)	Enforced maximum electron temperature value throughout domain
$\Delta_{max}T_e$	10 K ($\sim 8.6 \times 10^{-4}\text{ eV}$)	Enforced maximum change in electron temperature (at any given grid point) per electron timestep dt_{sub}
γ	1.0	Ionization cost factor for S_{ioniz} (Eqn. 3.49e)
Number of neutral particles	$\sim 400,000$	Time-averaged total number of simulated neutral superparticles in computational domain
Number of ion particles	$\sim 1.6\text{M} - 2.1\text{M}$	Time-averaged total number of simulated ion superparticles in computational domain
Number of grid points	2000	Grid with 40 points (non-uniform) in z and 50 points (uniform) in θ
Total simulated time	1.9 ms	Time extent of simulation (corresponds to 190,000 outer loop timesteps dt or 1.9M inner loop timesteps dt_{sub})
Total wall clock time	$\sim 200\text{ hours}$ ($\sim 8.3\text{ days}$)	Simulation execution time on a single Intel Xeon (E3-1245 v3) 3.40 GHz processor core

5.1.3 Initial Conditions

Initial conditions were prescribed for the neutral and ion particle populations and the electron temperature $T_e(z)$. The neutral and ion particle populations were initialized by assigning a uniform number of superparticles to each cell, with the particles randomly distributed in position within each cell. The prescribed initial ion particle population was set to reflect a uniform ion number density of $n_i = 2 \times 10^{17} \text{ m}^{-3}$ throughout the computational domain; the neutral population was initialized according to a neutral density profile which varied linearly from a peak value of $n_n(z = 0) = 4 \times 10^{19} \text{ m}^{-3}$ at the anode to $n_n(z = 0.12 \text{ m}) = 2 \times 10^{19} \text{ m}^{-3}$ at the downstream computational boundary. The particle velocities were initialized by inverting the respective Maxwellian ion and neutral velocity distributions, described in Appendix A, based on initial equilibrium temperatures $T_i = 650 \text{ K}$ for the ions and $T_n < 1 \text{ K}$ for the neutrals.

The initial electron temperature was prescribed according to the analytical temperature profile

$$T_e(z) = T_{e0} + T_{e,peak} \exp\left(-\frac{(z - z_{peak})^2}{z_\sigma^2}\right)$$

with constants $T_{e0} = 34,416 \text{ K}$ ($\sim 3 \text{ eV}$), $T_{e,peak} = 36,416 \text{ K}$ ($\sim 3.1 \text{ eV}$), $z_{peak} = 0.077$, and $z_\sigma = 0.02$, to roughly mimic the shape and magnitude of the experimentally-measured electron temperature profile (Meezan, 2002). The analytical expression is used in lieu of the experimentally-measured values to provide a smooth initial profile from which the simulated profile can evolve. The initial electron temperature profile has a peak value of approximately 6.1 eV just upstream of the thruster exit plane at $z = 0.077 \text{ m}$.

5.2 Plasma Properties

5.2.1 Initial Transient Behavior

After initializing and launching the simulation, we observe an initial transient phase during which the plasma properties evolve from the initial conditions before eventually settling into a quasi-steady-state. Here, we present results for the particular operating and initial

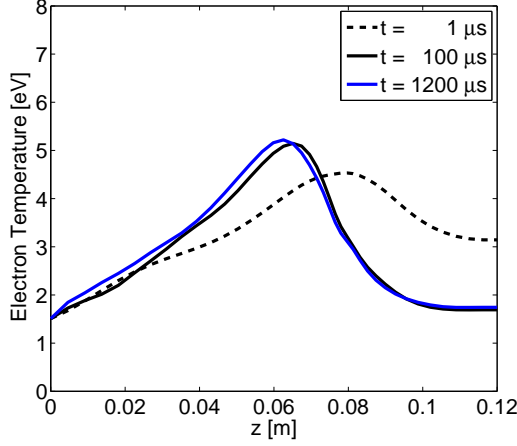


Figure 5.1: Electron temperature $T_e(z)$ at various times t .

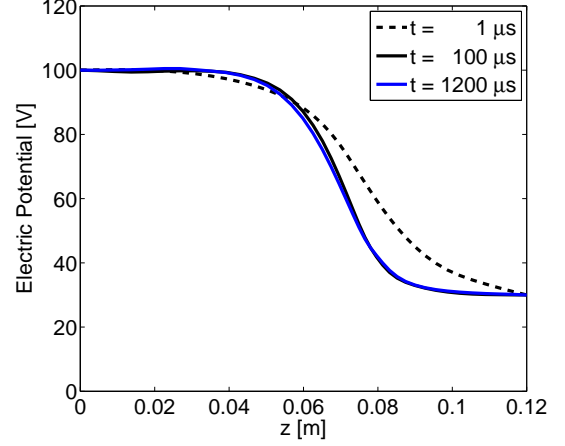


Figure 5.2: Electric potential $\phi(z)$ at various times t . (Shown relative to experimentally-measured potential $\phi(z = 0.12) = 30\text{V}$.)

conditions described in Sect. 5.1; however in all such numerically-stable simulations for the low voltage operating condition ($\Delta\phi = 70\text{ V}$), the plasma tends towards the same eventual quasi-steady-state (i.e., similar quasi-steady values and axial profiles for the plasma properties), regardless of the prescribed initial conditions for n_n , $n_i(=n_e)$, and T_e .

Figures 5.1 - 5.4 illustrate the trends in various plasma properties during this initial transient phase. In each case, the property values have been averaged over θ to provide a θ -averaged axial profile of the property variation with z , e.g., $T_e(z)$; the respective figures show the time evolution of these axial property profiles by providing a comparison of the property profiles at various times, e.g., $T_e(z, t)$. In the case of the PIC properties (e.g., the ion and neutral velocities and neutral density), we sample the population average or PIC-interpolated quantities at the computational grid points; likewise, the fluid properties (e.g., electron velocities) and grid-calculated properties (e.g., the plasma density, electric potential, and electric fields) are evaluated at these same grid points.

The electron temperature $T_e(z)$ and electric potential $\phi(z)$ profiles stabilize quickly, within the first $\sim 100\text{ }\mu\text{s}$ of the simulation, as shown in Figs. 5.1 and 5.2. The time evolution of the axial electric field $E_z(z)$ and axial ion velocity $u_{iz}(z)$ is shown in Figs. 5.3a and 5.3c,

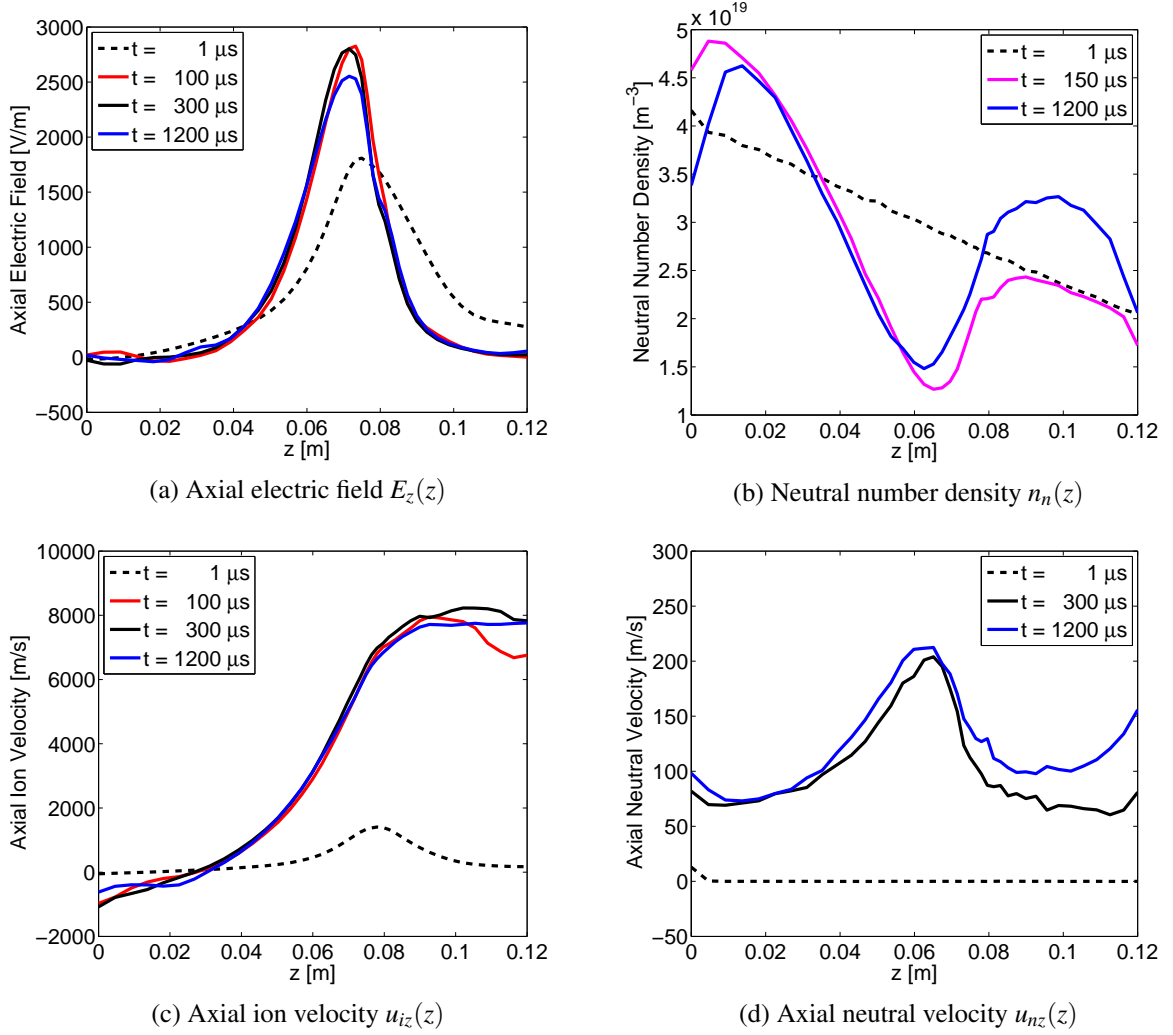


Figure 5.3: Axial electric field, axial ion velocity, neutral number density, and axial neutral velocity at various times t .

respectively. The axial profile of the population average axial ion velocity $u_i(z)$, which is governed by the axial electric field $E_z = -\frac{\partial\phi}{\partial z}$, has mostly stabilized by $t \simeq 100 \mu\text{s}$ (i.e., when the electric potential profile $\phi(z)$ has stabilized). However, there is a population of slow-moving (low velocity) ions outside the channel exit ($z \gtrsim 0.1 \text{ m}$) which are created by the ionization of slow-moving (low velocity) neutrals in that region; since the axial electric field E_z is weak in this region, these newly created low velocity ions retain their low velocity (due to the absence of a strong accelerating electric field) and serve to reduce the population average ion velocity in the region. The result is the observed dip, i.e., the decreased PIC-interpolated population average value, in the tail of the population average ion velocity $u_i(z)$ for $z \gtrsim 0.1 \text{ m}$. These slow moving ions, created from slow moving neutrals, are an artifact of the simulation initial conditions; by $t \simeq 300 \mu\text{s}$, the slow moving ions and neutrals have been mostly flushed out of the computational domain (i.e., most of the low velocity neutrals have either exited the computational domain without being ionized or have been ionized, and the resulting ions have exited the computational domain after being accelerated by the weak positive electric field E_z downstream of the channel) as the ion velocity profile stabilizes to its quasi-steady-state.

Figures 5.3b and 5.3d show the time evolution of the neutral number density n_n and population average axial neutral velocity u_{nz} , respectively. The general shape and features of the neutral density profile $n_n(z)$ stabilize fairly quickly, by $t \simeq 150 \mu\text{s}$; however, the the extremum values (peak and minimum values) of this profile do not fully stabilize until $t \simeq 1200 \mu\text{s}$. This is the time required for the initial neutral population to evolve, both by ionization and by exiting the computational domain, to the quasi-steady-state, as the injected neutral population (i.e., neutrals injected from the anode plane according to the velocity distribution described in Sect. 3.3) move through the computational domain and replace the initial neutral population. Correspondingly, the approximate profile shape of the population average axial neutral velocity $v_n(z)$ stabilizes by $t \simeq 300 \mu\text{s}$; however, the peak and minimum values do not fully stabilize until $t \simeq 1200 \mu\text{s}$, when the neutral particle population and neutral density profile have stabilized.

Similar to the neutral density profile, the plasma number density, i.e., the electron density or ion density, profile $n_e(z) = n_i(z)$ does not stabilize until $t \simeq 1200 \mu\text{s}$. The shape of

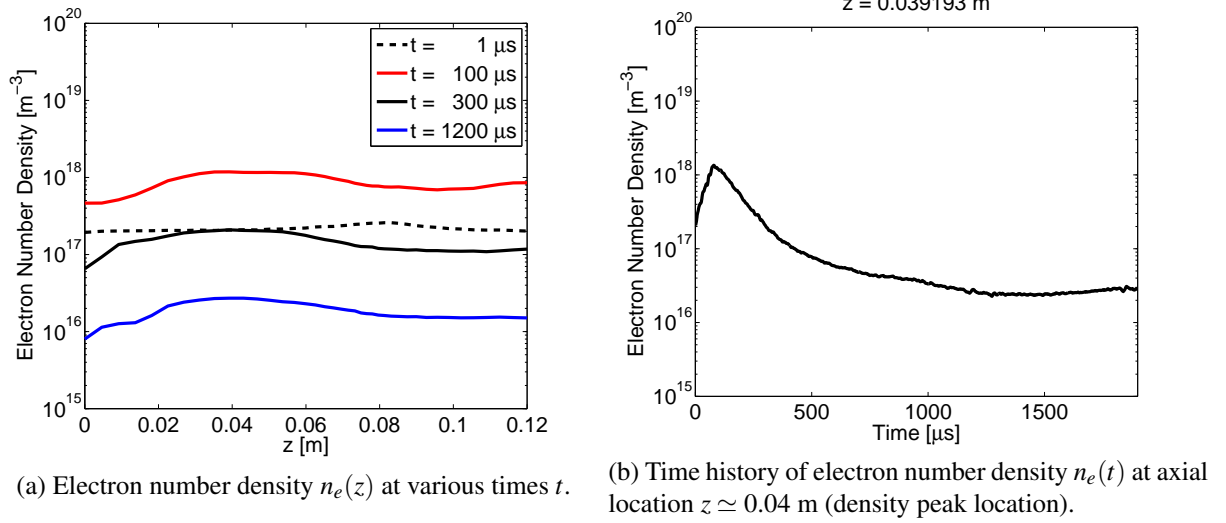


Figure 5.4: Electron number density profile and time history, shown on logarithmic scale.

the plasma density profile, which evolves from the flat (uniform) initial condition, is established within the first $100 \mu\text{s}$ of the simulation. There is an initial surge, throughout the computational domain, in the magnitude of the plasma density during the first $100 \mu\text{s}$ of the simulation; during this time, the magnitude of the plasma density rapidly increases as the axial profile shape develops. The plasma density magnitude reaches its maximum value at approximately $t \simeq 100 \mu\text{s}$; after that, the magnitude of the plasma density steadily falls, decreasing by two orders of magnitude, until it finally stabilizes at approximately $t \simeq 1200 \mu\text{s}$. Once the axial profile shape has been established at $t \simeq 100 \mu\text{s}$, it remains consistent; for $t \gtrsim 100 \mu\text{s}$, the axial location of the defining feature of the plasma density profile, the plasma density peak, persists at the location $z \simeq 0.04 \text{ m}$, both while the magnitude of the plasma density is evolving (i.e., decreasing for $t \simeq 100 \mu\text{s} - 1200 \mu\text{s}$) and after the quasi-steady-state has been reached ($t \gtrsim 1200 \mu\text{s}$). Figure 5.4a shows the plasma density profile as it evolves to the eventual quasi-steady-state, and Fig. 5.4b shows the time history of the plasma density at the axial peak location $z \simeq 0.04 \text{ m}$; note that, in both figures, the plasma density values $n_e(z, t)$ are shown on a logarithmic scale.

5.2.2 Quasi-steady Operation

In typical Hall thruster operation and in SHT laboratory experiments, the thruster settles into a quasi-steady operation mode after some initial start-up transient period. Similarly, the simulated plasma properties eventually settle to a quasi-steady-state, in this case, for $t \gtrsim 1200 \mu\text{s}$. The simulated quasi-steady-state is representative of the quasi-steady operation condition and enables comparison to laboratory measurements of the quasi-steady operation of the SHT laboratory discharge; we compare the simulated quasi-steady state to time-averaged laboratory measurements of properties within the SHT channel (Hargus, 2001; Meezan, 2002).

Figures 5.5 - 5.7 provide a comparison of the time-averaged simulated axial property profiles with the experimentally-measured values. The simulated properties are first averaged over θ to obtain the θ -averaged axial property profiles, e.g., $T_e(z, t)$, as described in Sect. 5.2.1; the axial property profiles are then time-averaged over the interval $t \simeq 1300 \mu\text{s}$ - $1900 \mu\text{s}$ to obtain the time-averaged simulated axial profiles, e.g., $\bar{T}_e(z)$, shown in Figs. 5.5 - 5.7.

In most cases, the time-averaged simulated property profiles agree reasonably well with the experimental measurements, as shown in Fig. 5.5. Figures 5.5a and 5.5c show the respective electric potential and axial ion velocity profiles. The shape of the simulated electric potential profile $\bar{\phi}(z)$ is similar to the experimental profile, with comparable electric potential values throughout the computational domain; however, the axial location of the simulated electric potential fall (i.e., the z -region in which the maximum axial electric field E_z exists and the majority of the electric potential drop occurs) is shifted slightly upstream, relative to the experimental profile. There is a corresponding discrepancy between the simulated and experimentally-measured axial ion velocity profiles $\bar{u}_{iz}(z)$, which are primarily governed by the axial electric field $E_z = -\frac{\partial \phi}{\partial z}$. While the simulated axial and ion velocity profiles show excellent agreement toward the anode ($z \lesssim 0.04 \text{ m}$) and outside the channel ($z \gtrsim 0.1 \text{ m}$), there is a discrepancy in the ion acceleration region. In laboratory experiments, most of the ion acceleration occurs in a narrow axial region near the channel exit plane at $z = 0.08 \text{ m}$; the simulated profile exhibits a broader axial ion acceleration region which occurs further upstream ($0.05 \text{ m} \lesssim z \lesssim 0.08 \text{ m}$).

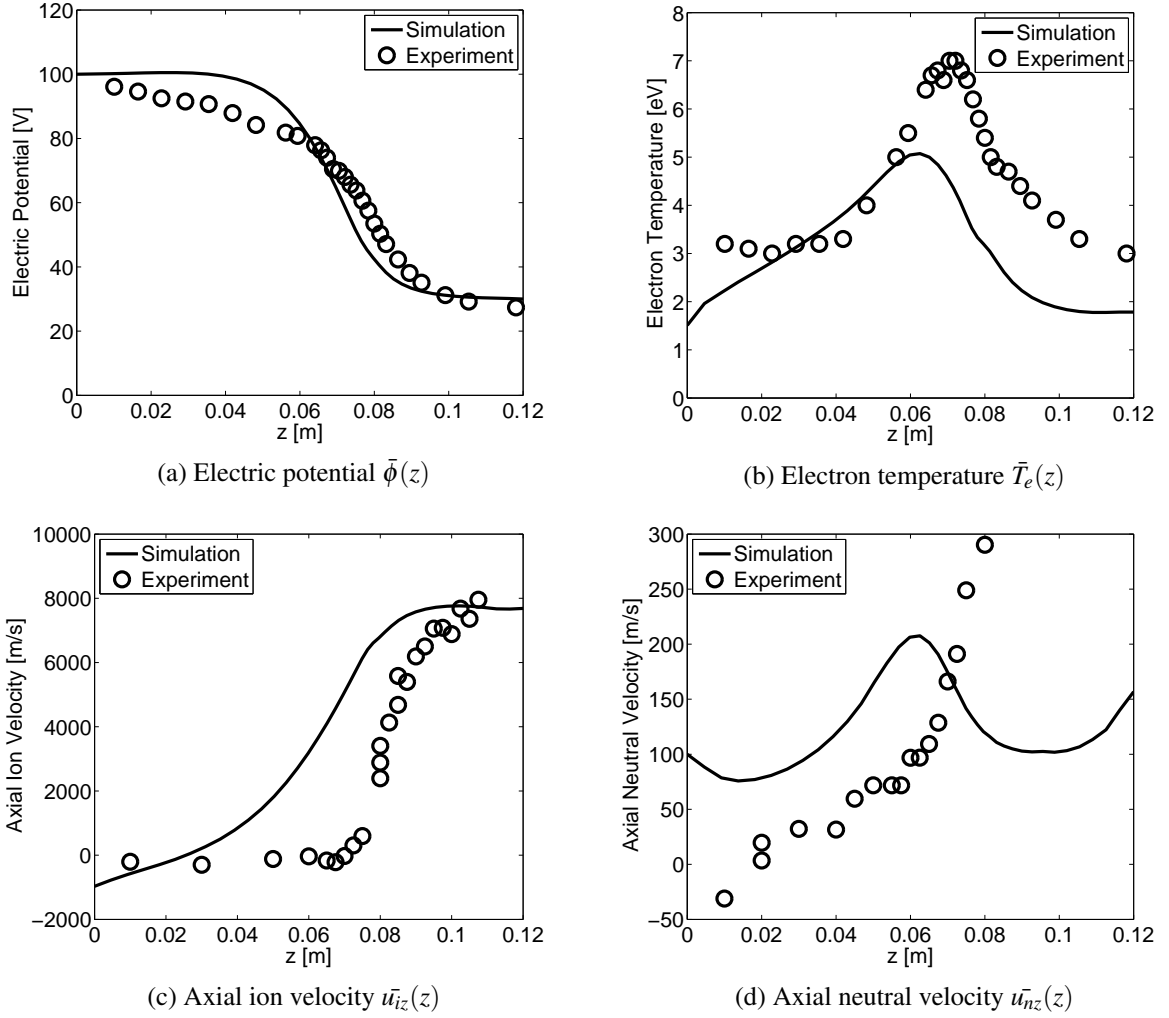
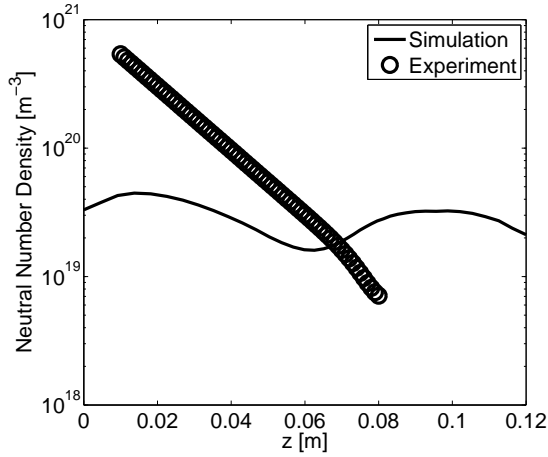
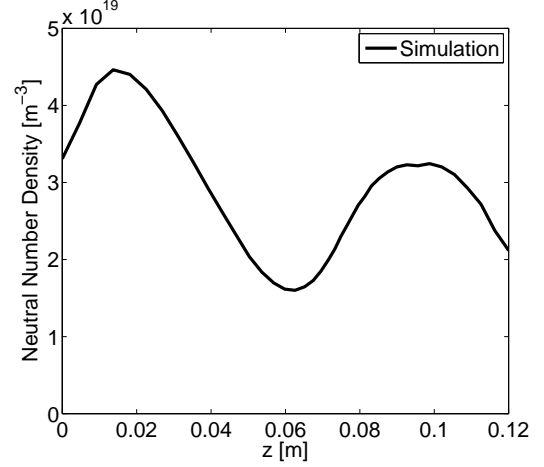


Figure 5.5: Time-averaged electric potential, electron temperature, axial ion velocity and axial neutral velocity profiles, compared with experimentally-measured values.

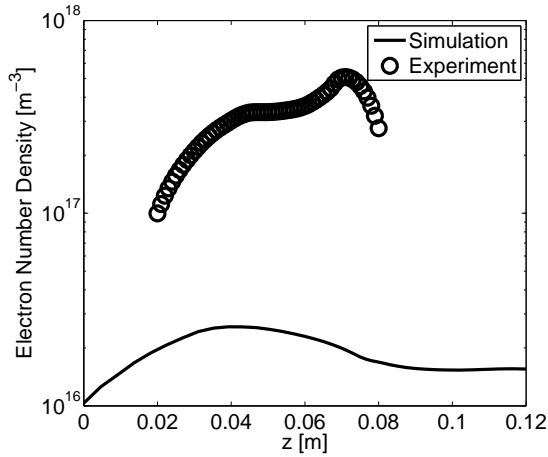


(a) Simulated and experimentally-measured values, shown on logarithmic scale.

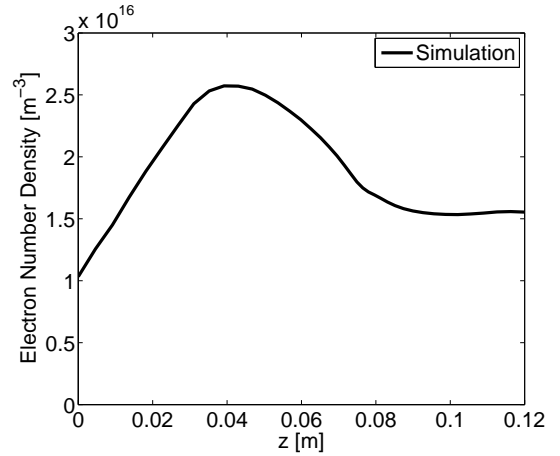


(b) Simulated profile shown on linear scale.

Figure 5.6: Time-averaged neutral number density profile $\bar{n}_n(z)$ compared with experimentally-measured values.



(a) Simulated and experimentally-measured values, shown on logarithmic scale.



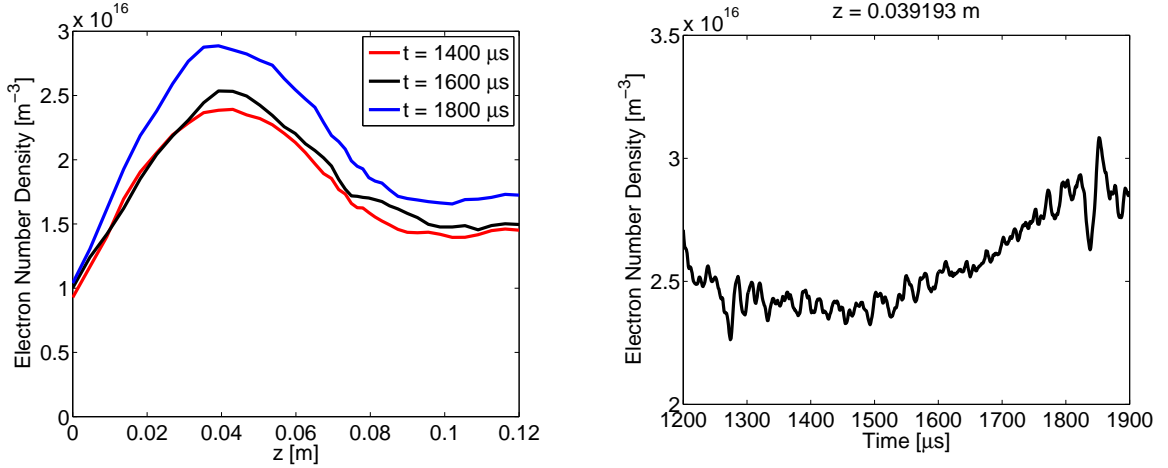
(b) Simulated profile shown on linear scale.

Figure 5.7: Time-averaged electron number density profile $\bar{n}_e(z)$ compared with experimentally-measured values.

The simulated electron temperature values are slightly lower than the experimentally-measured values, as shown in Fig. 5.5b; the simulated peak electron temperature value is approximately 2 eV lower than the experimentally-measured peak and the simulated minimum electron temperature values, which occur at the domain ends $z = 0$ and $z = 0.12$ m, are approximately 1 eV lower than the corresponding experimental values. The axial location of the simulated electron temperature peak, at $z \simeq 0.06$ m, occurs slightly upstream of the experimentally-measured peak location ($z \simeq 0.075$ m).

Inside the channel ($z \leq 0.08$ m), the axial neutral velocity profile shows reasonable qualitative agreement with the experimentally-measured profile, as shown in Fig. 5.3d. For $z \gtrsim 0.02$ m, both the simulated and experimental profiles exhibit the same increasing velocity trend with increasing z . Outside the channel ($z > 0.08$ m), experimental measurements are scarce, and the experimental and simulated profiles appear to diverge; however, given the scarcity of data in this region and that we do not explicitly model the neutral flow (or plume) expansion outside the channel, this discrepancy is not concerning. There is a significant discrepancy between the simulated neutral number density profile $\bar{n}_n(z)$ and the experimentally-measured values; as shown in Fig., 5.6a, the simulated neutral density magnitude is significantly lower than the experimentally-measured values. The profile shapes also differ significantly; however, for $0.02 \text{ m} \lesssim z \lesssim 0.06 \text{ m}$, both the simulated and experimental profiles exhibit a similar decreasing magnitude trend with increasing z . The experimental neutral density values are based on an indirect, i.e., inferred, measurement; as such, there is significant uncertainty in the experimentally-measured values for this property, and the discrepancy between the simulated and experimentally-measured values may be within the experimental measurement uncertainty.

The one notable discrepancy between the simulated and experimentally-measured profiles is in the electron number density $\bar{n}_e(z)$, shown in Fig. 5.7. Throughout the domain, the simulated quasi-steady electron number density is more than an order of magnitude smaller than the experimentally-measured profile values. There is also a significant discrepancy in the axial location and shape of the plasma density peak; the experimental profile is characterized by a sharp peak at $z \simeq 0.07$ m, just upstream of the exit plane, while the simulated profile exhibits a much broader peak which occurs farther upstream at $z \simeq 0.04$ m.



(a) Electron number density profile $n_e(z)$ at various times $t > 1200 \mu\text{s}$.

(b) Time history of electron number density $n_e(t)$ at axial location $z \simeq 0.04 \text{ m}$ (density peak location), shown for $t \geq 1200 \mu\text{s}$.

Figure 5.8: Fluctuating nature of electron number density during quasi-steady-state operation.

In both cases (i.e., for both the experimental laboratory discharge and its simulation counterpart), the quasi-steady-state is non-stationary; reflective of operational behavior, the simulation predicts continuing sustained fluctuations in the plasma properties as shown in Fig. 5.8. Once the simulated discharge has reached a quasi-steady-state, the plasma property magnitudes do not vary significantly; we can characterize the continuing fluctuations as small perturbations, or small signal oscillations, relative to the established steady-state, or time-averaged, condition. These fluctuations are, in fact, a distinctive feature of the simulation; we are particularly interested in characterizing the fluctuations, or sustained oscillations, in the electron density and axial electron velocity as they relate to electron transport and the total sustained discharge current.

5.3 Discharge Current

The total axial electric current, or discharge current, defines the I-V (current-voltage) operating condition of the thruster. The axial electric current is comprised of a contribution from

the electron current and a contribution from the ion current; we define the axial discharge current

$$I_D = I_e + I_i \quad (5.1)$$

where I_e and I_i are the respective electron and ion current contributions to the total discharge current. At any axial location z , we can write the electron and ion currents in terms of the respective current densities J_{ez} and J_{iz}

$$I_e = J_{ez} A_{sect} \quad (5.2a)$$

$$I_i = J_{iz} A_{sect} \quad (5.2b)$$

where $A_{sect} = 0.0031 \text{ m}^2$ is the cross-sectional area of the thruster as defined by Eqn. 3.1, and

$$J_{ez}(z) = -\frac{1}{2\pi} \int_0^{2\pi} e n_e(z, \theta) u_{ez}(z, \theta) d\theta \quad (5.3a)$$

$$J_{iz}(z) = \frac{1}{2\pi} \int_0^{2\pi} e n_e(z, \theta) u_{iz}(z, \theta) d\theta \quad (5.3b)$$

with $n_i = n_e$ according to quasineutrality and $e = 1.6 \times 10^{-19} \text{ C}$. In practice, we calculate the current density contributions at the discrete grid points (z_i, θ_j) :

$$J_{ez}(z_i) = -\frac{1}{N_\theta} \sum_j e n_e(z_i, \theta_j) u_{ez}(z_i, \theta_j) \quad (5.4a)$$

$$J_{iz}(z_i) = \frac{1}{N_\theta} \sum_j e n_e(z_i, \theta_j) u_{iz}(z_i, \theta_j) \quad (5.4b)$$

Note that we define positive current as positive charge moving in the $+z$ -direction, i.e., from the anode towards the cathode. In the case of the electrons, due to their negative electrical charge, electrons moving in the negative z -direction ($-z$) result in positive current;

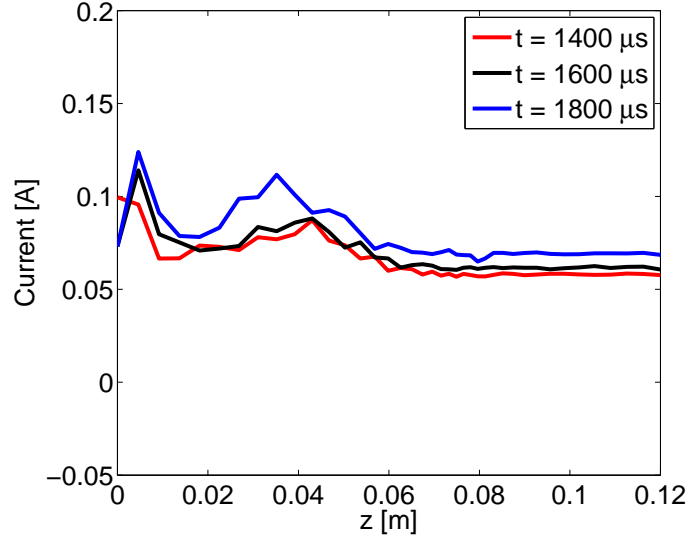


Figure 5.9: Discharge current $I_D(z)$ at various times t .

electrons moving in the positive z -direction ($+z$) result in negative current, according to the current convention used here.

Figures 5.9 and 5.10 illustrate the fluctuating nature of the discharge current during quasi-steady operation ($t \gtrsim 1200 \mu\text{s}$). Figure 5.9 shows an overlay comparison of representative time snapshots of the axial variation in the discharge current, which oscillates throughout the domain about its quasi-steady (time-averaged) profile values. Figure 5.10 shows the time history of the simulated discharge current at an axial location just upstream of the channel exit. As the plasma density n_e rises, falls, then stabilizes to a quasi-steady state, the discharge current correspondingly exhibits an initial surge (peak value at $t \simeq 100 \mu\text{s}$) followed by a steady decrease in magnitude, before it stabilizes to a quasi-steady value of approximately 0.06 A at $z = 0.078 \text{ m}$.

From Fig. 5.10b, we can observe an extremely slow-moving temporal oscillation in the discharge current with an apparent time period of approximately $T \simeq 1000 \mu\text{s} - 1200 \mu\text{s}$, which corresponds to a linear frequency $f \leq 1 \text{ kHz}$; a similar fluctuation can be observed in the plasma density (electron number density), as shown in Fig. 5.8b. We believe that this fluctuation may be related to the transit time of the neutrals across the domain, i.e., through the thruster; for an axial neutral velocity $u_{nz} = 70 \text{ m/s} - 100 \text{ m/s}$, as observed upstream

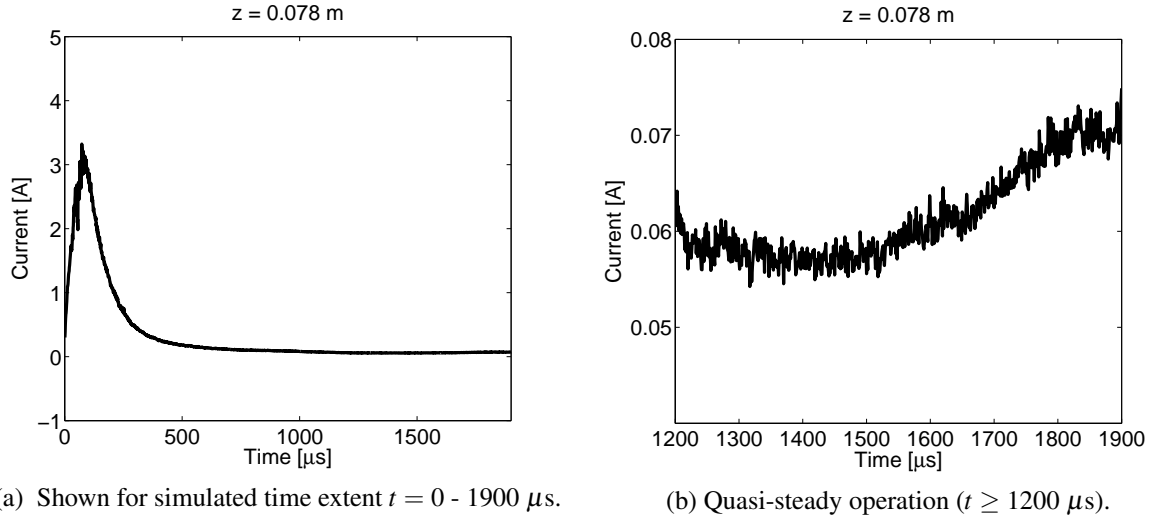


Figure 5.10: Time history of discharge current $I_D(t)$ at axial location $z = 0.078$ m (just upstream of the exit plane).

in the channel for $z \lesssim 0.04$ m in Fig. 5.5d, the time required to traverse the length of the thruster channel $L = 0.08$ m is approximately $T_{n,transit} = L/u_{nz} \simeq 800 \mu s - 1200 \mu s$. This neutral transit time oscillation may be similar to or related to the experimentally-observed breathing mode phenomenon.

In laboratory experiments at this operating voltage, the measured discharge current was approximately 2 A. The simulated quasi-steady discharge current, which varies between 0.05 - 0.12 A, is significantly lower than the experimentally-measured current. We attribute this discrepancy to the extremely low simulated plasma density (n_e) magnitude (discussed in Sect. 5.2.2 and shown in Fig. 5.7a). The simulated plasma density magnitude is 1 - 2 orders of magnitude lower than the experimentally-measured plasma density; as expected, the simulated discharge current is correspondingly 1 - 2 orders of magnitude smaller than the experimentally-measured current.

The relative contributions of the electron and ion currents, I_e and I_i , respectively, to the total discharge current I_D vary with z . Fig. 5.11 shows the time-averaged electron and ion contributions to the total discharge current (all time-averaged over the interval $t = 1300 \mu s - 1900 \mu s$). For $z \lesssim 0.05$ m, the electron current dominates; in this region, the electron current comprises most of the total current and the ion current contribution

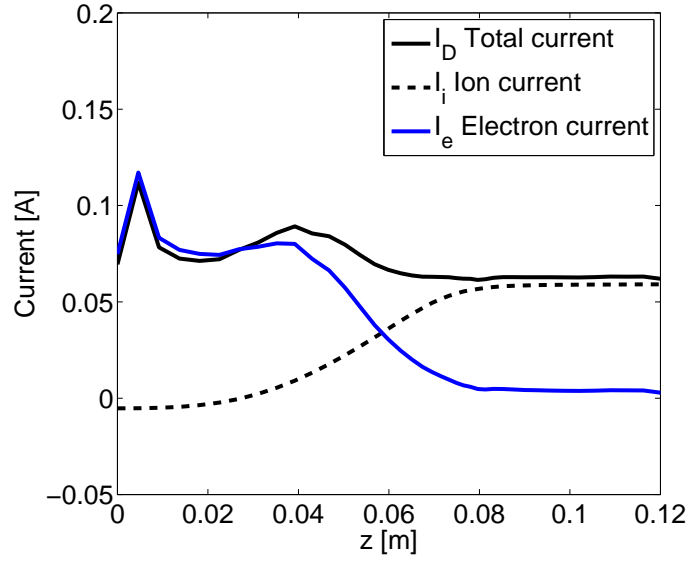
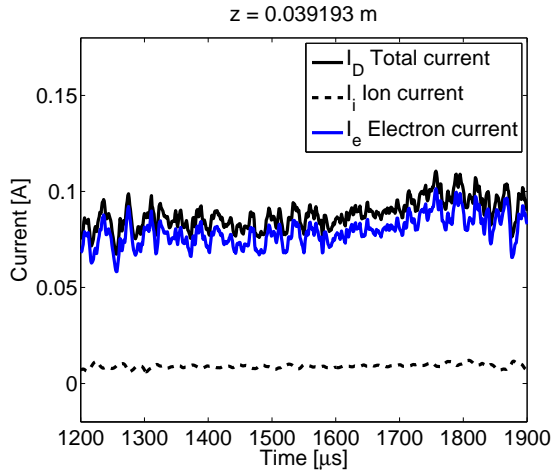
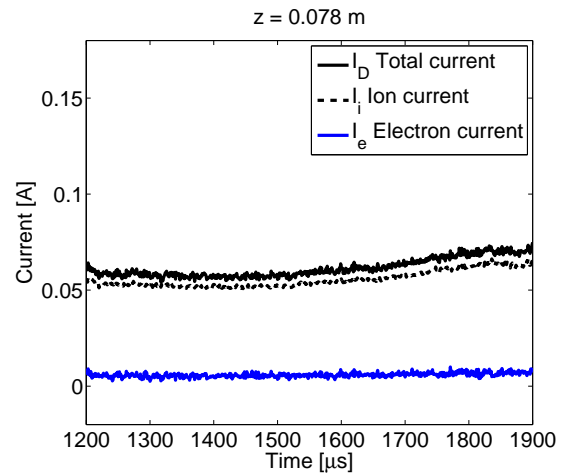


Figure 5.11: Comparison of time-averaged ion and electron current contributions to total discharge current.



(a) At axial location $z \simeq 0.04$ m (mid-channel).



(b) At axial location $z = 0.078$ m (just upstream of the exit plane).

Figure 5.12: Time history of ion and electron current contributions to total discharge current during quasi-steady operation ($t \geq 1200 \mu\text{s}$).

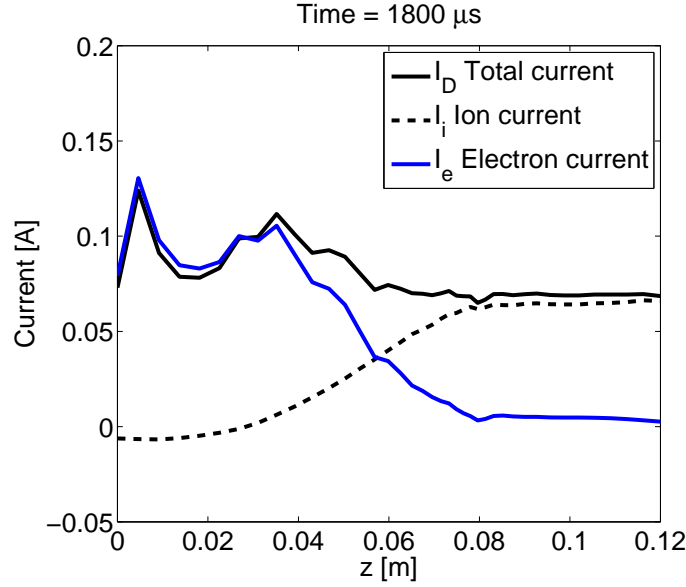


Figure 5.13: Time snapshot of ion and electron current contributions to total discharge current.

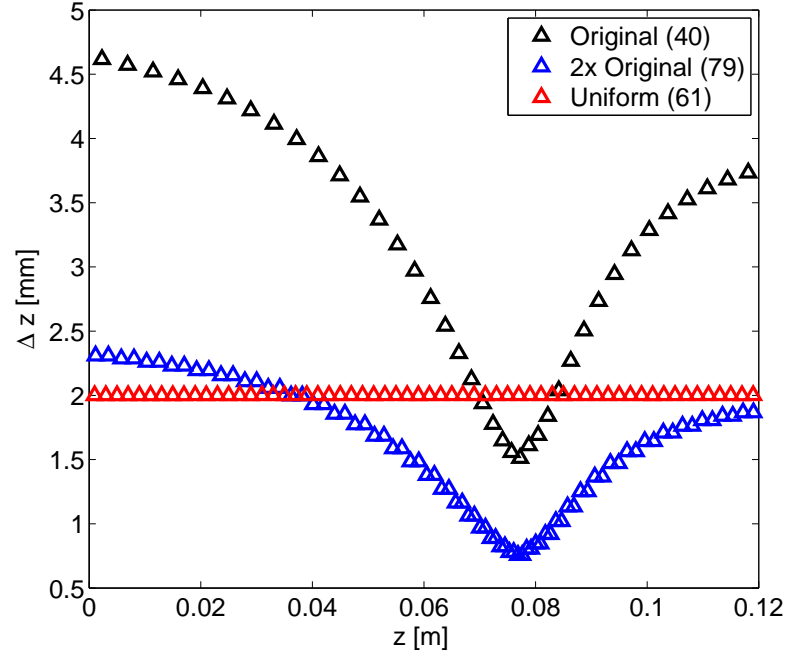
is small or, in some cases (i.e., for $z \lesssim 0.02$ m near the anode), negative. For $z \gtrsim 0.07$ m, the electron current contribution is extremely small and the ion current dominates; for most of this region, the electron current is an extremely small positive current and, near the exit plane ($z = 0.08$ m), the electron current is sometimes negative, leading to a reduction in the total current. Figure 5.12 shows the time history of the current at representative z -locations within the two distinct current regions in which the respective electron and ion current contributions dominate; in all cases (i.e., for all z), the ion and electron current contributions and the resulting total current fluctuate with time.

Figure 5.13 shows a representative time snapshot of the current contributions and total current, during simulated quasi-steady operation. Note that the total discharge current varies, in some cases, significantly, with axial position. Although the relative electron and ion current contributions can vary with z , current conservation dictates that the axial discharge current should be conserved, i.e., $\frac{dI_D}{dz} = 0$; the simulated results clearly violate current conservation. We suspect that the current non-conservation is an artifact of the non-conservative numerical scheme used in the simulations; for the finite-difference discretization scheme and numerical solution method employed here, there is no specific

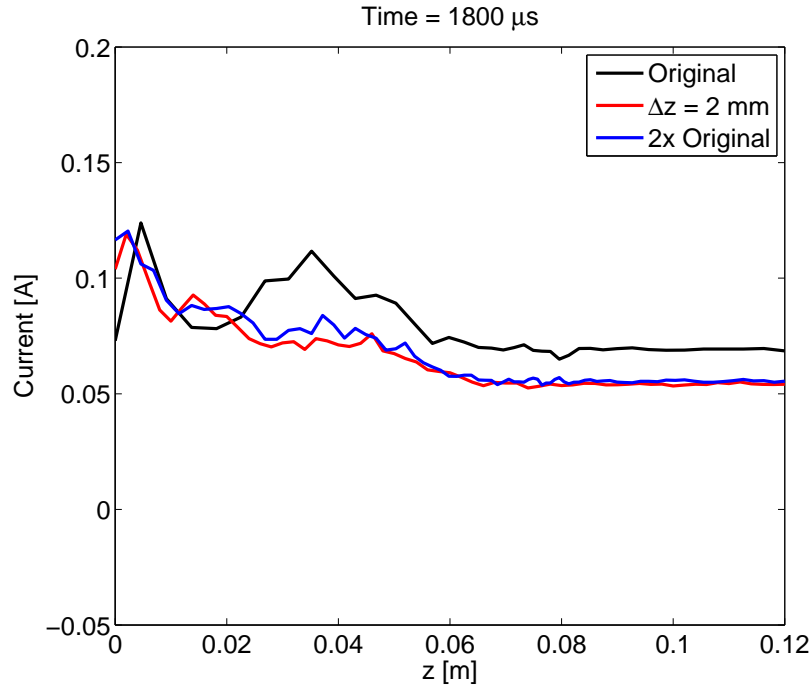
enforcement of current conservation. An alternative approach would be to use a conservative, e.g., finite volume, numerical scheme; a finite volume formulation of this model is being developed separately and is currently still in progress. When completed, it will be compared to the present results and may provide an alternative to the present finite difference implementation. For most of the computational domain, the current non-conservation ($\frac{dI_D}{dz} \neq 0$) is not significant; in the region $z > 0.05$ m, the total current is reasonably well conserved and varies minimally, by $< 10\%$. However, near the anode, for $z \leq 0.04$ m, the axial variation in the total discharge current is significant.

In the region $z \leq 0.04$ m, the total current varies by as much as 40% over a range of 0.05 A (from approximately 0.07 A minimum to 0.12 A maximum). We believe the strong variation in the axial current (for $z \leq 0.04$ m) to be a consequence of the non-conservative numerical scheme, coarse grid resolution, and strong gradients in the plasma properties in this region. The imposition of the axisymmetric electric potential boundary condition at the anode ($z = 0$) leads to an effective boundary layer and strong gradients near the anode; without significantly finer (computationally expensive) grid resolution, such strong gradients can be difficult to resolve via a finite difference scheme, as employed here. We believe the coarseness of the axial grid in this region, i.e., the failure to sufficiently resolve strong axial gradients in this region, contributes to the apparent lack of global current conservation in this region.

To assess the effect of axial grid resolution on the current non-conservation effect, we performed a limited grid refinement study; we refined the grid in z as shown in Fig. 5.14a, reducing the grid spacing from a maximum $\Delta z = 4.6$ mm for the original non-uniform grid to a minimum $\Delta z = 2$ mm near the anode for the 61-point uniform grid (and $\Delta z = 0.75$ mm near the exit plane for the 79-point non-uniform grid). Figure 5.14b compares a representative time snapshot of the resulting respective axial profiles for the discharge current. We observe some improvement in axial current conservation (i.e., a reduction in the current non-conservation effect) with grid refinement, especially in the region $0.02 \text{ m} \leq z \leq 0.04 \text{ m}$. We expect further grid refinement would further improve the axial current conservation.



(a) Axial grid spacing Δz for non-uniformly- and uniformly-spaced grids. Number in parentheses indicates total number of axial grid points.



(b) Time snapshot of axial (i.e., total discharge) current.

Figure 5.14: Comparison of axial current conservation with axial grid refinement.

Even with further grid refinement, properly resolving the anode region, and the discharge current in this region, has historically been problematic for other similar hybrid simulations (e.g., Scharfe, 2009); furthermore, in this region of weak magnetic field strength, there is little experimental data for comparison and validation. In general, the near anode region is less well described and more difficult to accurately simulate than other features of the thruster discharge; the variation in the predicted axial current is thus not surprising. The current is reasonably well conserved throughout the rest of the thruster channel and computational domain ($z > 0.04$ m) with the present numerical scheme and original (coarsest) grid resolution.

5.4 Electron Transport

We are interested in characterizing the cross-field axial electron transport, i.e., the electron transport perpendicular to the radial magnetic field B_r in the axial (z -) direction. We define the effective axial electron mobility

$$\mu(z) = \frac{J_{ez}}{en_e E_z} \quad (5.5)$$

where $e = 1.6 \times 10^{-19}$ C, J_{ez} is as defined in Eqns. 5.3a and 5.4a, and $n_e = n_e(z)$ and $E_z = E_z(z)$ are the θ -averaged electron number density and axial electric field, respectively, at axial location z .

We can compare the simulated axial electron mobility profile $\mu(z)$ with experimentally-measured values (Meezan et al., 2001; Meezan, 2002). To obtain the time-averaged simulated mobility profile, we first calculate the time-dependent axial electron mobility $\mu(z, t)$ for all sampled time t and locations z ; we then time-average the mobility values $\mu(z, t)$ over the specified time interval to obtain the time-averaged profile $\bar{\mu}(z)$. In Fig. 5.15, the simulated mobility values have been time-averaged over the quasi-steady operation interval $t \simeq 1300 \mu\text{s} - 1900 \mu\text{s}$.

We can also calculate the various contributions to the cross-field electron transport, or mobility. We consider the axial electron velocity, described by Eqn. 3.51a and repeated here for convenience,

$$\begin{aligned}
u_{ez} = & -\mu_{\perp} E_z - \frac{D_{\perp}}{n_e} \frac{\partial n_e}{\partial z} - \frac{D_{\perp}}{T_e} \frac{\partial T_e}{\partial z} - \frac{1}{1 + \left(\frac{v_{en}}{\omega_{ce}}\right)^2} \frac{E_{\theta}}{B_r} \\
& - \frac{1}{1 + \left(\frac{v_{en}}{\omega_{ce}}\right)^2} \frac{k_B T_e}{en_e B_r r} \frac{\partial n_e}{\partial \theta}
\end{aligned} \tag{5.6}$$

The first three terms on the right hand side of Eqn. 5.6 comprise the so-called classical contribution to the electron mobility, where

$$\mu_{\perp} = \frac{e}{m_e v_{en} \left[1 + \left(\frac{\omega_{ce}}{v_{en}} \right)^2 \right]} \tag{5.7}$$

is the classical expression for the cross-field electron mobility, i.e., the electron mobility in the direction perpendicular to the magnetic field, based on electron-neutral collisions. Including the second and third terms, which account for the effect of axial gradients in the electron number density and the electron temperature (i.e., gradients in the electron pressure), we can calculate the so-called classical electron velocity and resulting classical mobility (i.e., the axial electron mobility based solely on classical theory):

$$u_{ez, classical} = -\mu_{\perp} E_z - \frac{D_{\perp}}{n_e} \frac{\partial n_e}{\partial z} - \frac{D_{\perp}}{T_e} \frac{\partial T_e}{\partial z} \tag{5.8}$$

where

$$D_{\perp} = \frac{k_B T_e}{e} \mu_{\perp} \tag{5.9}$$

$$J_{ez, classical}(z) = -\frac{1}{2\pi} \int_0^{2\pi} en_e u_{ez, classical} d\theta \tag{5.10}$$

$$\mu_{classical}(z) = \frac{J_{ez, classical}}{en_e E_z} \tag{5.11}$$

and , as in Eqn. 5.5, $n_e = n_e(z)$ and $E_z = E_z(z)$ are the θ -averaged electron number density and axial electric field, respectively, at axial location z . The fourth and fifth terms on the right hand side of Eqn. 5.6 comprise the so-called anomalous contribution to the electron current, i.e., the portion of the electron transport (or current) beyond that described by classical theory. It is via these two terms that the azimuthal (θ) dynamics influence the axial electron velocity u_{ez} ; specifically, azimuthal gradients in the electric potential $-\frac{\partial\phi}{\partial\theta} = E_\theta$ and the electron density $\frac{\partial n_e}{\partial\theta}$ can affect the axial electron velocity. We can calculate the so-called anomalous transport, i.e., the contribution to the axial electron current due to temporal and spatial fluctuations and gradients in θ .

$$u_{ez,anom} = -\frac{1}{1 + \left(\frac{v_{en}}{\omega_{ce}}\right)^2} \frac{E_\theta}{B_r} - \frac{1}{1 + \left(\frac{v_{en}}{\omega_{ce}}\right)^2} \frac{k_B T_e}{en_e B_r r} \frac{\partial n_e}{\partial \theta} \quad (5.12)$$

$$J_{ez,anom}(z) = -\frac{1}{2\pi} \int_0^{2\pi} en_e u_{ez,anom} d\theta \quad (5.13)$$

$$\mu_{anom}(z) = \frac{J_{ez,anom}}{en_e E_z} \quad (5.14)$$

Figure 5.15 provides a comparison of the total effective simulated electron mobility $\bar{\mu}(z)$ and the experimentally-measured effective electron mobility; time-averaged profiles, taken on the same interval $t \simeq 1300 \mu s - 1900 \mu s$, for the classical cross-field mobility $\bar{\mu}_\perp(z)$ and overall classical contribution to the mobility $\bar{\mu}_{classical}(z)$ are shown for reference. Figure 5.16 illustrates the relative contribution of the anomalous electron current $I_{e,anom} = J_{ez,anom} A_{sect}$ to the corresponding time-averaged electron current I_e and the discharge current I_D ; as before, the various current contributions and the total discharge current have been time-averaged over the interval $t \simeq 1300 \mu s - 1900 \mu s$.

We are interested in the simulation's ability to predict the axial electron mobility, as compared to the experimentally-measured values. For much of the domain, there is a significant discrepancy between the simulated mobility and the experimentally-measured values; for $z \gtrsim 0.035$ m, the simulated mobility is 1 - 1.5 orders of magnitude smaller than the experimentally-measured values.

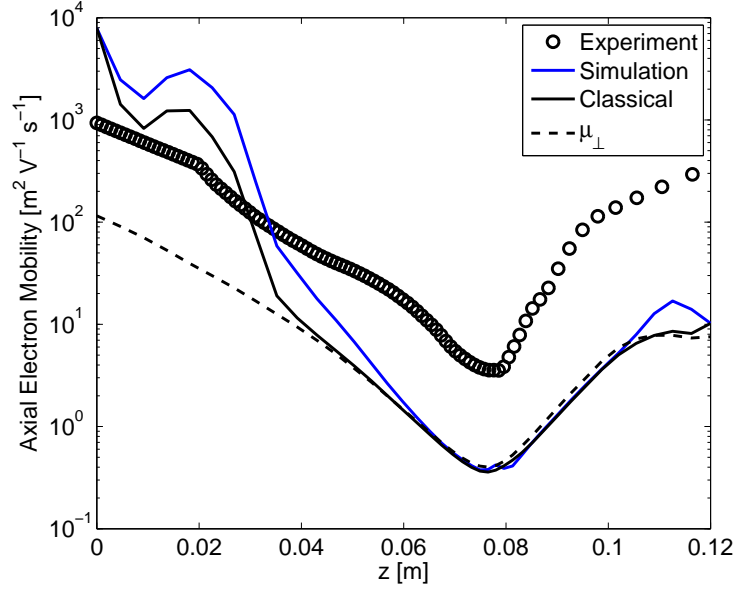


Figure 5.15: Time-averaged simulated axial electron mobility $\bar{\mu}(z)$ compared to experimentally-measured values. Simulated classical mobility terms $\bar{\mu}_{classical}$ and $\bar{\mu}_{\perp}$ are shown for reference.

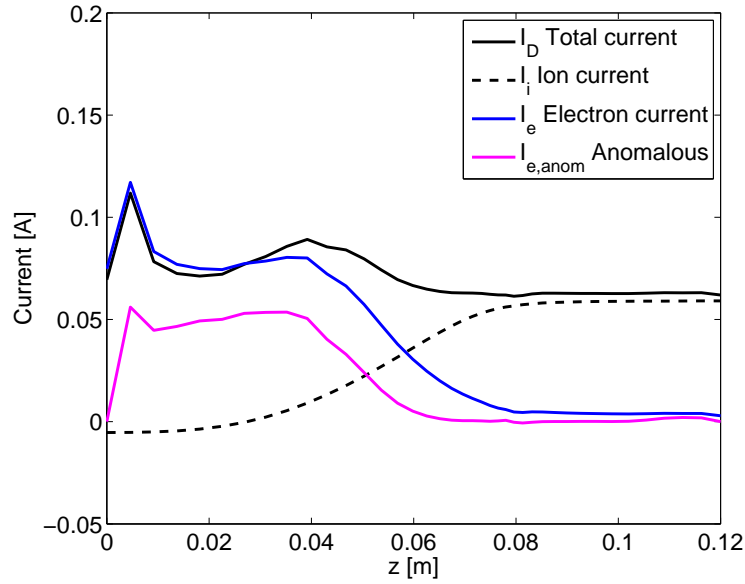


Figure 5.16: Comparison of time-averaged ion, electron, and anomalous electron current contributions to total discharge current.

We can further focus on the relative contributions of the so-called classical and anomalous electron mobility (or electron transport) terms. For $z \gtrsim 0.03$ m, the classical mobility contribution is significantly lower than the experimentally-measured mobility. In comparing the classical contribution (i.e., the electron mobility predicted by classical theory) and the experimental mobility, we see that classical theory alone cannot fully account for the experimentally-observed electron transport; by consequence and as has been shown in previous simulation efforts (Bouchoule et al., 2004; Adam et al., 2008; Scharfe, 2009; Cha, 2015), models based solely on classical theory (i.e., with no ad hoc or experimentally-based super-classical mobility scaling or inclusion of azimuthal effects) cannot be expected to fully capture the axial electron transport.

For much of the domain ($0.005 \text{ m} \lesssim z \lesssim 0.06 \text{ m}$ and $z \gtrsim 0.105 \text{ m}$), the total simulated mobility is significantly higher than the simulated classical mobility; we can attribute this discrepancy, or mobility enhancement above the classical mobility, to the anomalous portion of the electron current. As shown in Fig. 5.16, the anomalous contribution comprises the majority ($> 50\%$) of the electron current in these regions. Near the channel exit plane and outside the channel ($z \gtrsim 0.07 \text{ m}$), the total electron current is relatively small and, consequently, comprises a small portion of the total current; the anomalous contribution is correspondingly small, even in the region $z \gtrsim 0.105 \text{ m}$ where it comprises most of the electron current. However, inside the channel for $0.005 \text{ m} \lesssim z \lesssim 0.06 \text{ m}$, the anomalous contribution to the electron current is significant; in this region, the anomalous contribution current significantly enhances, i.e., adds to, the total effective electron mobility. For $0.03 \text{ m} \lesssim z \lesssim 0.06 \text{ m}$ and $z \gtrsim 0.105 \text{ m}$, the anomalous electron current contribution leads to a total enhanced electron mobility that is greater than the classical mobility and that is, in some cases, comparable to the experimentally-measured values. In these regions, the simulated anomalous transport thus accounts for some of the difference between the classical mobility and the experimental mobility.

A representative time snapshot of the relative anomalous contribution to the electron current, as shown in Fig. 5.17, reveals interesting axial variations not easily discerned from the time-averaged profile, shown in Fig. 5.16, and provides further insight into the role of the anomalous electron current. As in the time-averaged case, the electron current is strongly anomalous (i.e., the anomalous contribution appears to primarily comprise the

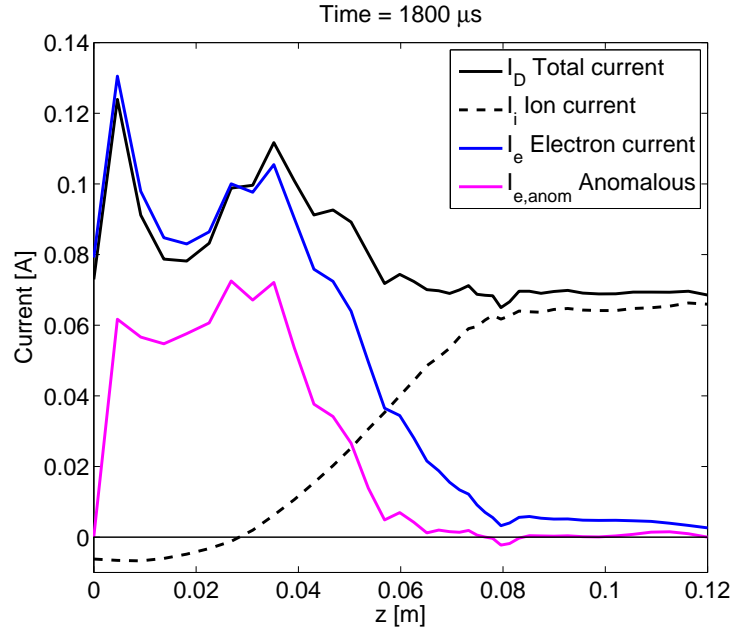


Figure 5.17: Time snapshot of ion, electron, and anomalous electron current contributions to total discharge current.

positive electron current) in the region $0.005 \text{ m} \lesssim z \lesssim 0.05 \text{ m}$; in this region, the simulated anomalous electron current appears to enhance the electron mobility, adding to and augmenting the classical electron mobility, resulting in a total effective mobility that is, in some cases, comparable to the experimentally-measured values. However, near the exit plane at $z = 0.08 \text{ m}$, the anomalous electron transport results in a negative current contribution to the electron current, i.e., the anomalous contribution serves to oppose, or reduce, electron transport in this region; as will be further discussed in Chap. 6, it appears that the anomalous electron current may contribute to a transport barrier in this region (instead of a transport enhancement as it does upstream inside the thruster channel). It is clear that the anomalous electron current plays a significant role in the overall electron transport for most of the simulated domain, resulting in either enhanced or reduced transport for certain distinct axial regions within the thruster and near plume.

Chapter 6

Discussion

6.1 Fluctuation-Induced Transport

6.1.1 Premise

It has been suggested (Yoshikawa and Rose, 1962; Janes and Lowder, 1966; Fife, 1999) that quasi-coherent fluctuations resulting from instabilities in the plasma can play a role in electron transport – specifically, that correlated azimuthal fluctuations in the electron (plasma) density and the electron velocity can contribute to axial (i.e., cross-field) electron transport. As a simple example, consider a spatially- and temporally-fluctuating electron number density and electron velocity, each fluctuating with the same wavenumber $k = 2\pi/\lambda$ and frequency $\omega = 2\pi f$,

$$\tilde{n}_e(x, t) = n_o \cos(kx - \omega t) \quad (6.1a)$$

$$\tilde{u}_e(x, t) = u_o \cos(kx - \omega t + \psi) \quad (6.1b)$$

We can calculate the current density based on this fluctuating density \tilde{n}_e and velocity \tilde{u}_e

$$J_e(x, t) = e\tilde{n}_e(x, t)\tilde{u}_e(x, t) \quad (6.2)$$

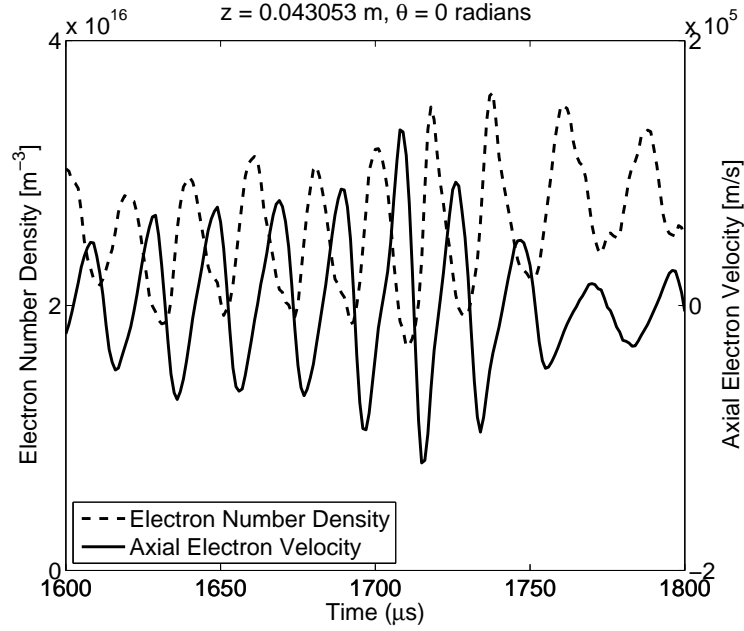


Figure 6.1: Time history of electron number density $n_e(t)$ and axial electron velocity $u_{ez}(t)$, shown for $t = 1600 \mu s - 1800 \mu s$ at $z \simeq 0.043$ m.

where $e = 1.6 \times 10^{-19}$ C. Averaging over one full cycle, i.e., over one spatial wavelength λ and one temporal period $T = 1/f$, we can find the net resulting fluctuation-induced current

$$\begin{aligned}
 \langle J_e \rangle &= \frac{1}{T} \frac{1}{\lambda} \int_T \int_{\lambda} e n_o \cos(kx - \omega t) u_o \cos(kx - \omega t + \psi) dx dt \\
 &= \frac{1}{2} e n_o u_o \cos \psi
 \end{aligned} \tag{6.3}$$

From Eqn. 6.3, we see that the resulting net, or average, current depends on the phase difference ψ between the fluctuating quantities \tilde{n}_e and \tilde{u}_e . This phase offset ψ , between the fluctuating electron number density and electron velocity, determines not only the magnitude, but also the sign, or direction, of the resulting current.

Figure 6.1 shows the time history of the electron number density and axial electron velocity at a representative location (z, θ) . The fluctuating electron density and axial electron velocity appear to have a similar, i.e., correlated quasi-coherent, temporal structure

or fluctuation frequency f ; depending on the phase difference between the two fluctuating quantities, so-called anomalous or fluctuation-induced electron current can result. We are specifically interested in the axial electron current

$$\langle J_{ez} \rangle_{anom} = \frac{1}{T} \frac{1}{\lambda} \int_T \int_{\theta} e n_o \cos(k_{\theta} \theta - \omega t) u_o \cos(k_{\theta} \theta - \omega t + \psi) dx dt$$

generated by azimuthally-propagating fluctuations.

6.1.2 Simulated Waves

We observe spatially- and temporally-varying fluctuations in the plasma properties. In Fig. 6.2, we present representative time snapshots of the spatially-varying electron number density n_e , axial electron velocity u_{ez} , and electric potential ϕ to illustrate the spatial structure of the simulated waves; the properties also fluctuate with time, as shown previously for the electron number density in Fig. 5.8b. We can characterize the fluctuations as dispersive waves (or sinusoidal oscillations) with characteristic axial and azimuthal wavenumbers, $k_z = 2\pi/\lambda_z$ and $k_{\theta} = 2\pi/\lambda_{\theta}$, respectively, and temporal frequency $\omega = 2\pi f$, e.g.,

$$\tilde{n}_e(z, \theta, t) = n_o \cos(k_z z + k_{\theta} \theta - \omega t) \quad (6.4a)$$

$$\tilde{u}_{ez}(z, \theta, t) = u_o \cos(k_z z + k_{\theta} \theta - \omega t + \psi) \quad (6.4b)$$

We are interested in the dispersive wave characteristics, i.e., frequencies and wavenumbers $\omega(k)$ or, equivalently, linear frequencies and wavelengths $f(1/\lambda)$, especially those that propagate in the azimuthal direction and generate axial electron transport. At any axial location z , we can calculate the fluctuation-induced anomalous electron current

$$J_{ez,anom}(z, t) = \frac{1}{2\pi} \int_{\theta} \tilde{n}_e(z, \theta, t) \tilde{u}_{ez}(z, \theta, t) d\theta$$

where $n_e(z, \theta, t)$ and $u_{ez}(z, \theta, t)$ assume a form similar to Eqns. 6.4a and 6.4b. Note that we do not limit our study to a single wavenumber or frequency; we fully expect that, multiple

frequencies f and wavenumbers k_z and k_θ will be present and can propagate simultaneously.

6.1.2.1 Azimuthal (θ) Grid Refinement

In order to better characterize, i.e., more finely resolve the wave structure in the azimuthal (θ) direction, we performed limited grid refinement in θ ; we doubled the number of grid points in θ , resulting in a grid with 100 points uniformly spaced in θ , i.e., $\Delta\theta = 2\pi/100$. Due to the additional computational expense, we performed simulations with the refined 100-point azimuthal grid only for a limited time duration $t = 1600 \mu\text{s} - 1800 \mu\text{s}$, starting from the plasma properties at $t = 1600 \mu\text{s}$ based on the previous simulation with the original grid with 40 points in $z \times 50$ points in θ , i.e., $\Delta\theta = 2\pi/50$.

Figure 6.3 provides a comparison of representative time snapshots for the 50- and 100-point azimuthal grids. For much of the domain, the discrepancy between the two grids is not significant; however, near the exit plane where there is fine azimuthal spatial structure in the axial electron velocity, shown for the respective grids in Figs. 6.3b and 6.3d, the increased azimuthal grid refinement is necessary. Figure 6.4 provides a comparison of time snapshots of the anomalous contribution to the electron current for simulations with the respective grids. It is clear that the azimuthal grid refinement affects the simulated current contributions throughout the channel ($z \leq 0.08$ m); near the exit plane at $z = 0.08$ m, the azimuthally-refined grid simulation predicts a stronger negative anomalous current than the original 50-point grid case. The resulting effect can be seen in Fig. 6.5 which provides a comparison of the time-averaged electron mobility; for the azimuthally-refined grid, we observe a lower effective mobility (due to the negative anomalous electron current) at $z \simeq 0.08$ m. This dip, or decrease, in the effective electron mobility near the exit plane is referred to as the transport barrier; with the azimuthally-refined grid, the simulated transport barrier near the exit plane is more pronounced.

6.1.2.2 Time Step Sampling (Undersampling of Simulated Time)

Both sets of simulations for the respective 50-point and 100-point azimuthal grids were performed using an outer loop time step $dt = 10$ ns. In the interest of reducing data storage and

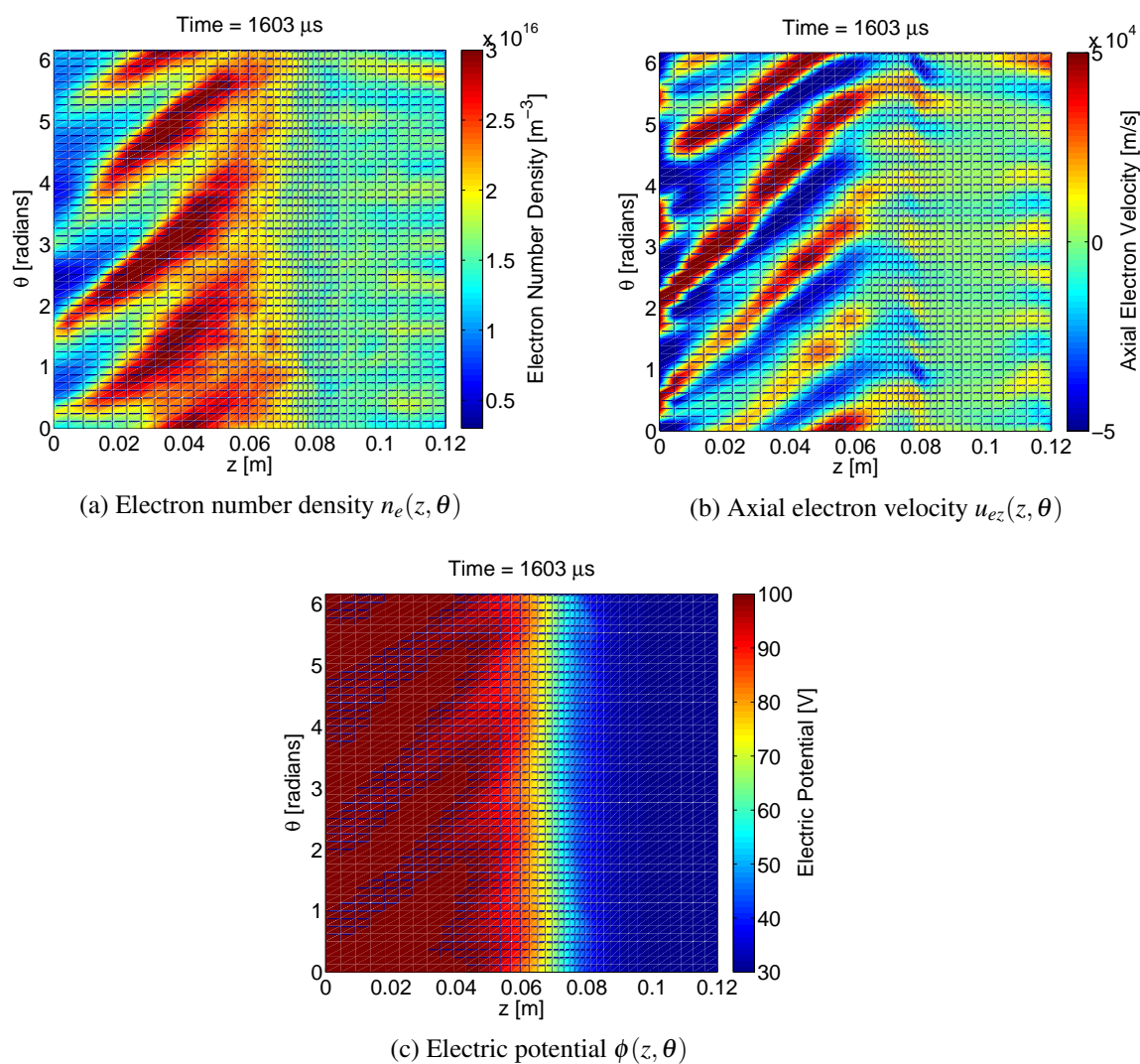
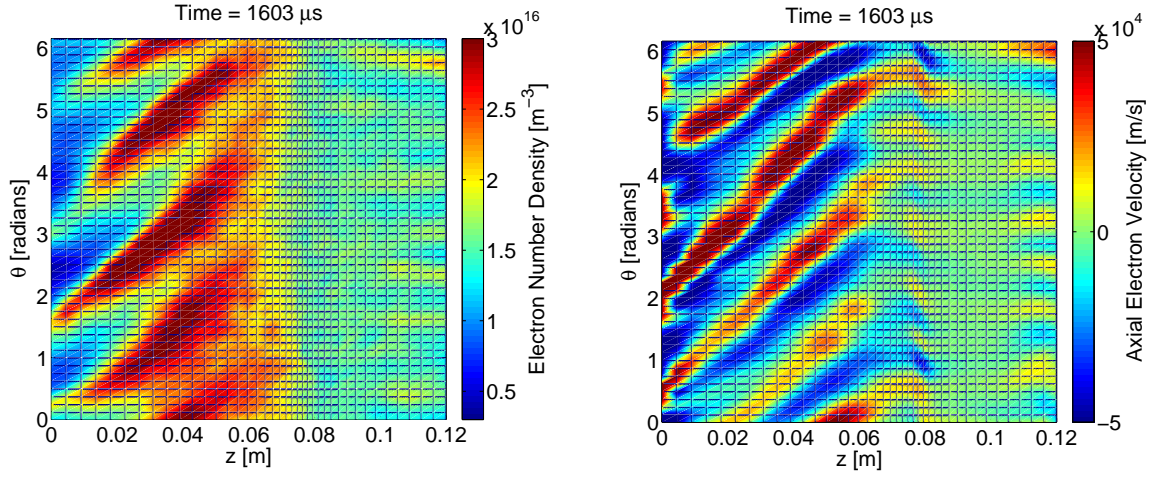
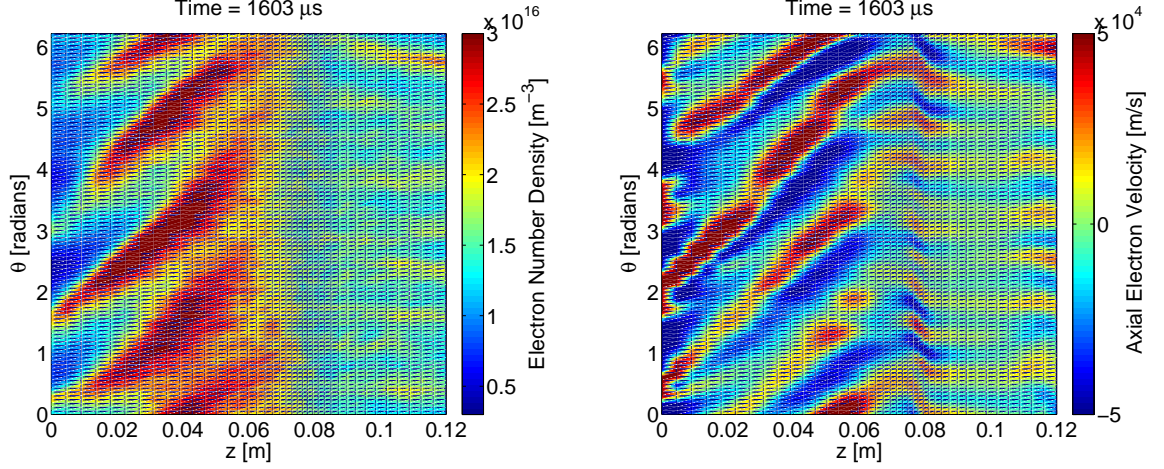


Figure 6.2: Representative time snapshots of axial and azimuthal variation in plasma properties.



(a) Electron number density $n_e(z, \theta)$ for grid with 40 points in $z \times 50$ points in θ ($\Delta\theta = 2\pi/50$). (b) Axial electron velocity $u_{ez}(z, \theta)$ for grid with 40 points in $z \times 50$ points in θ ($\Delta\theta = 2\pi/50$).



(c) Electron number density $n_e(z, \theta)$ for grid with 40 points in $z \times 100$ points in θ ($\Delta\theta = 2\pi/100$). (d) Axial electron velocity $u_{ez}(z, \theta)$ for grid with 40 points in $z \times 100$ points in θ ($\Delta\theta = 2\pi/100$).

Figure 6.3: Comparison of representative time snapshots of electron number density $n_e(z, \theta)$ and axial electron velocity $u_{ez}(z, \theta)$ with azimuthal grid refinement.

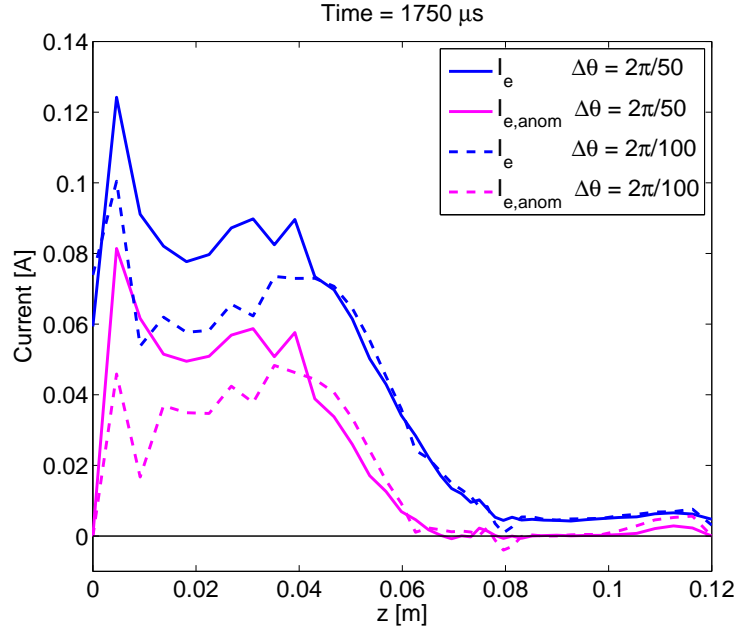
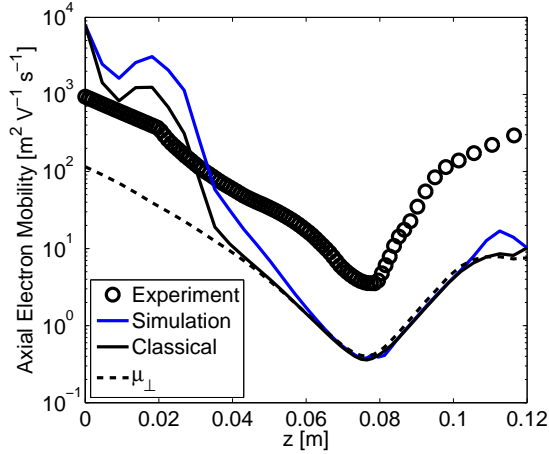
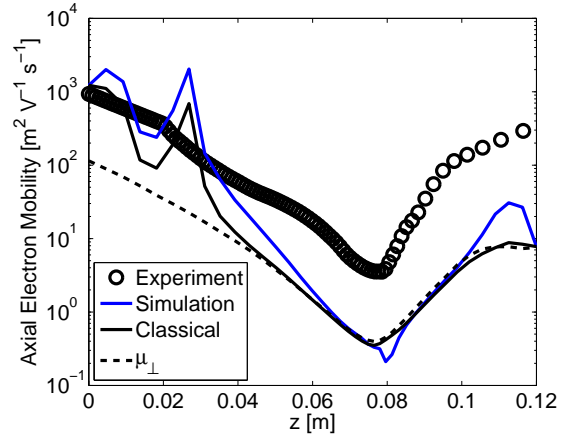


Figure 6.4: Time snapshot of anomalous contribution to electron current with azimuthal grid refinement.



(a) Grid with 40 points in $z \times 50$ points in θ ($\Delta\theta = 2\pi/50$), time-averaged over the interval $t = 1300 \mu\text{s} - 1900 \mu\text{s}$.



(b) Grid with 40 points in $z \times 100$ points in θ ($\Delta\theta = 2\pi/100$), time-averaged over the interval $t = 1600 \mu\text{s} - 1800 \mu\text{s}$.

Figure 6.5: Comparison of time-averaged simulated axial electron mobility $\bar{\mu}(z)$ with azimuthal grid refinement. Experimentally-measured values and simulated classical mobility terms $\bar{\mu}_{\text{classical}}$ and $\bar{\mu}_{\perp}$ are shown for reference.

data transfer overhead, we typically undersample the simulated data using a sampling time step $t_{\text{samp}} = 1 \mu\text{s} = 100dt$. A comparison of simulation results using the respective sampling time steps $t_{\text{samp},\text{max}} = dt = 10 \text{ ns}$ and $t_{\text{samp}} = 1 \mu\text{s} = 100dt$ shows that undersampling the data does not have any significant effect for most cases of interest.

The sampling time step most significantly affects the minimum time resolution or maximum resolvable temporal frequency; the maximum time step sampling $t_{\text{samp},\text{max}} = dt$ provides a Nyquist frequency of $f_{\text{Nyq},\text{max}} = 50 \text{ MHz}$, whereas undersampling at $t_{\text{samp}} = 100dt$ results in a Nyquist frequency $f_{\text{Nyq},\text{samp}} = 500 \text{ kHz}$. In the following analysis, we see that the relevant frequency content typically does not exceed $f_{\text{max}} = \frac{1}{2}f_{\text{Nyq},\text{samp}} = 250 \text{ kHz}$. It is not critical to resolve the timescale any more finely than $t_{\text{samp}} = 1 \mu\text{s}$; hence, the under-sampled data is, in most cases, sufficient.

6.2 Analysis of Simulated Waves

We focus on four axial regions in which we observe distinct wave structure and propagation characteristics:

1. Near-anode region: $z \leq 0.01 \text{ m}$
2. Mid-channel region: $0.02 \text{ m} \lesssim z \lesssim 0.06 \text{ m}$
3. Near exit plane (i.e., just upstream of exit plane): $0.07 \text{ m} \leq z \leq 0.08 \text{ m}$
4. Outside channel: $z > 0.08 \text{ m}$

Figures 6.6a and 6.6b are maps of the axial variation in the simulated axial wavenumber $k_z(f)$ and azimuthal wavenumber $k_\theta(f)$, respectively. The dispersive wave characteristics in Fig. 6.6 were obtained by performing a Morlet wavelet decomposition analysis, similar to that detailed in Thomas (2006) and Scharfe (2009) and further described in Appendix B. While most of the analysis results shown here are for the axial electron velocity u_{ez} , similar wave structure and propagation characteristics (k_z, k_θ, f) are observed in the electron density.

Figure 6.6a indicates that upstream in the channel for $z \leq 0.06 \text{ m}$, the axial wavenumber k_z is negative, i.e., the waves in this region propagate in the negative z -direction; near the

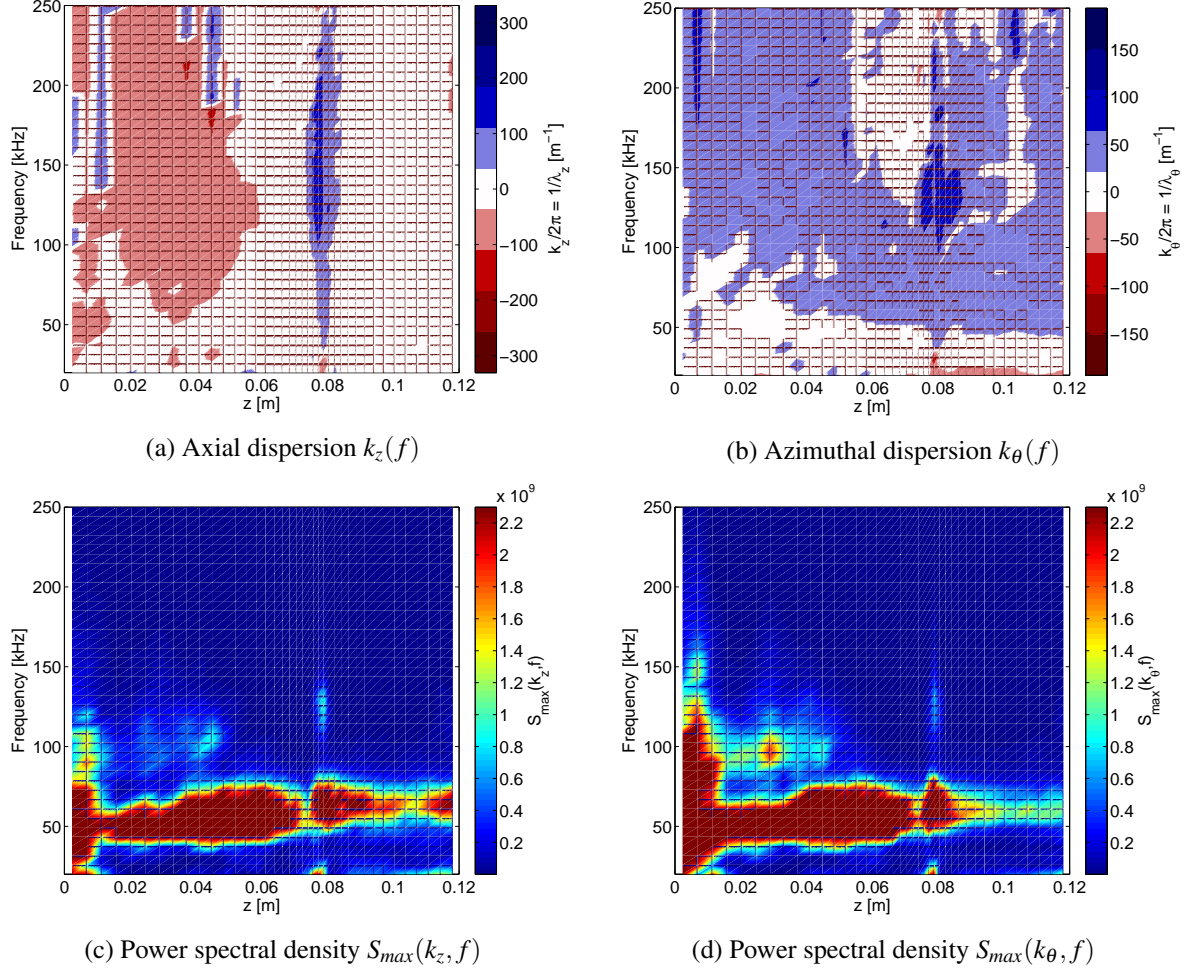


Figure 6.6: Axial variation of axial and azimuthal wave characteristics for axial electron velocity u_{ez} . Analysis performed for $t = 1600 \mu\text{s} - 1800 \mu\text{s}$ with $\Delta\theta = 2\pi/100$, sampled at $T_{\text{samp}} = 1 \mu\text{s}$ ($f_{\text{max}} = \frac{1}{2}f_{\text{Nyq}} = 250 \text{ kHz}$).

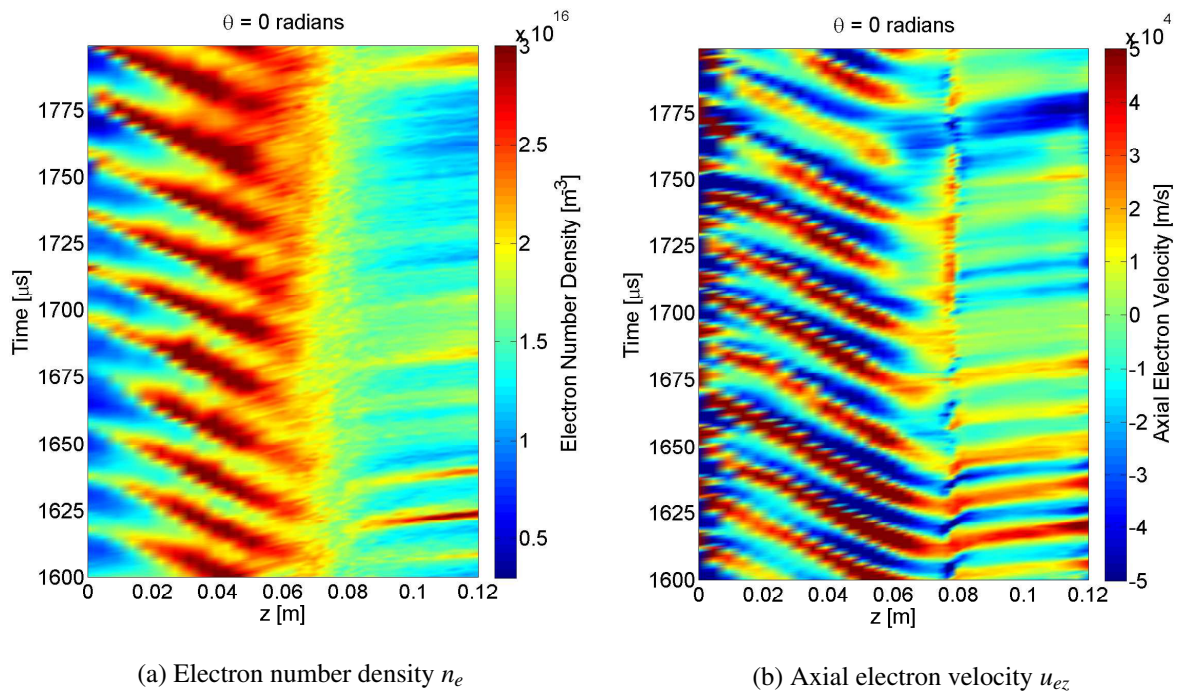


Figure 6.7: Axial streak plots at azimuthal location $\theta = 0$, shown for time duration $t = 1600 \mu\text{s} - 1800 \mu\text{s}$ with $\Delta\theta = 2\pi/100$.

exit plane, k_z is positive, indicating that the waves in this region propagate in the positive z -direction. We can observe the axial propagation direction more clearly from the streak plots (of axial position z versus time t , observed at single θ -location) shown in Fig. 6.7. For $z \leq 0.06$ m, we observe wave propagation in the negative z -direction; for $z \geq 0.08$ m, axial wave propagation is in the positive z -direction. Figure 6.6b shows the axial variation in the azimuthal wavenumber $k_\theta(f)$; for most of the domain (and at most frequencies f), azimuthal wave propagation is the positive θ -, i.e., the $+\mathbf{E} \times \mathbf{B}$, direction, where $\mathbf{E} \simeq E_z \hat{z}$ and $\mathbf{B} \simeq B_r \hat{r}$.

Note that not all wavenumbers and frequencies $k_z(f)$ and $k_\theta(f)$ depicted in Figs. 6.6a and 6.6b are equally significant. Figures 6.6c and 6.6d show the maximum scattering function, or power spectral density, values for the respective $k_z(z, f)$ and $k_\theta(z, f)$ shown in Fig. 6.6; the scattering function values indicate the relative magnitude or strength, i.e., the relative power or energy, carried in each of the propagation modes $k_z(z, f)$ and $k_\theta(z, f)$. Note that lower frequency modes in the range $f \simeq 0 - 120$ kHz appear to be the most dominant; they have the largest $S_{max}(k_z, f)$ and $S_{max}(k_\theta, f)$ values, indicating that they carry the most power (relative to other frequency modes).

6.2.1 Near Anode ($z \leq 0.01$ m)

Near the anode for $z \leq 0.01$ m, we observe a relatively low-velocity azimuthal disturbance with a long azimuthal wavelength λ_θ . From the azimuthal streak plots (of azimuthal position θ versus time t , observed at $z \simeq 0.005$ m) shown in Fig 6.8b, we see that the disturbance appears in both the electron density n_e and the axial electron velocity u_{ez} and corresponds to an azimuthal mode number $m_\theta = 4$. The wave propagation direction is tilted, i.e., the wave propagates in both the axial and azimuthal directions – in this case, in the negative z -direction (i.e., toward the anode) and the positive θ -direction.

We believe this disturbance may represent the so-called rotating spoke, which is a slow moving azimuthal rotation of the plasma near the anode which has been observed in laboratory experiments (Ellison et al., 2012). The spoke instability is characterized by distinct low azimuthal mode numbers ($m_\theta = 3 - 4$) and its radial extent across the channel width; viewed in the r - θ plane (i.e., cylindrical cross-sectional view of the thruster channel), it

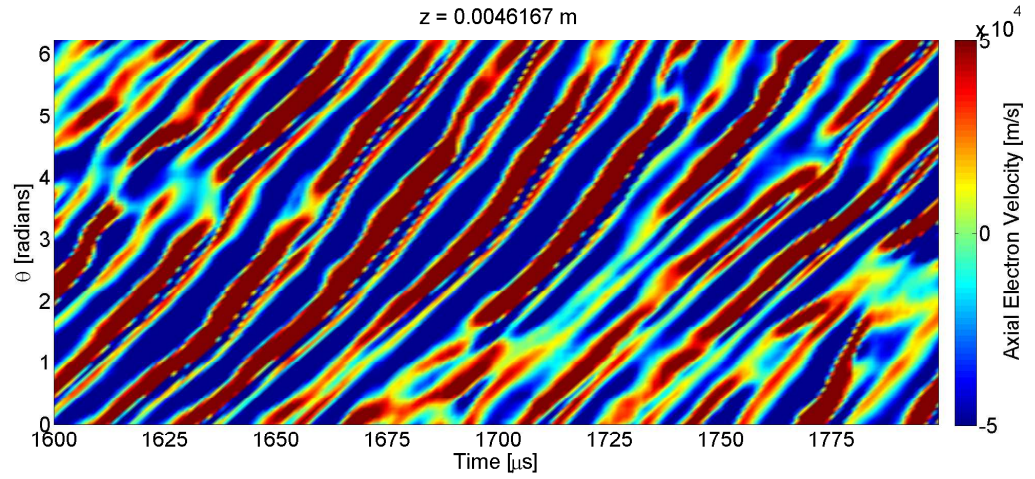
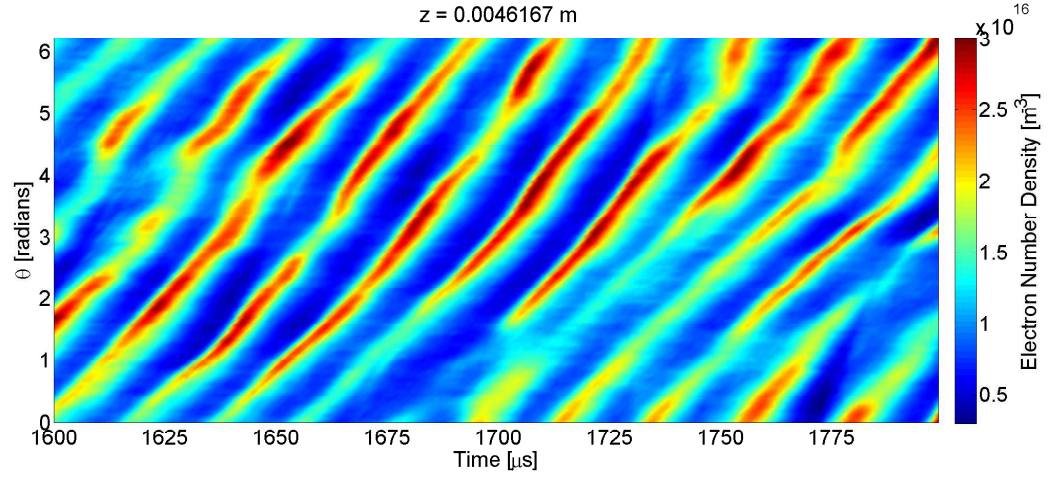


Figure 6.8: Azimuthal streak plots at axial location $z \simeq 0.005 \text{ m}$ (near anode), shown for time duration $t = 1600 \mu\text{s} - 1800 \mu\text{s}$ with $\Delta\theta = 2\pi/100$.

resembles the rotating spokes of a wheel. The rotating spoke is believed to carry significant current and represents a significant non-uniformity in the r - θ plane, with the majority of the current carried by the high electron density regions or spokes. Since we are concerned about current non-conservation (due to insufficient axial grid resolution) in this region as discussed in Sect. 5.3, it is difficult to make a strong statement regarding the current carried in this simulated disturbance. However, it is possible that current carried in the simulated spoke and the resulting strong gradients in both the axial and azimuthal directions contribute to the difficulty with the current non-conservation; in addition to the axial grid resolution required to address strong axial gradients in this region, the non-uniformity due to the rotating spoke may place further, more stringent constraints upon the required axial and azimuthal grid resolution in this region.

6.2.2 Mid-channel ($0.02 \text{ m} \leq z \leq 0.06 \text{ m}$)

In the mid-channel region $0.02 \text{ m} \leq z \leq 0.06 \text{ m}$, we observe tilted waves which propagate in the negative z -direction and positive θ -direction, as shown in the respective axial and azimuthal streak plots Figs. 6.7 and 6.9. Figure 6.10 shows the scattering functions $S(k_z, f)$ and $S(k_\theta, f)$ for the axial and azimuthal propagation, respectively, obtained from the wavelet decomposition analysis at $z \simeq 0.04 \text{ m}$. As expected, Fig. 6.10a indicates propagation in the negative z -direction at fairly low wavenumber $k_z/2\pi \simeq -30 \text{ m}^{-1}$, i.e., long axial wavelength λ_z , and fairly low frequency $f \simeq 30 \text{ kHz} - 70 \text{ kHz}$. In the azimuthal direction, Fig. 6.10b indicates propagation in both the positive and negative θ -directions; while there is some propagation in the negative θ -direction for very low frequency ($f \leq 10 \text{ kHz}$), there is clear propagation in the positive θ -direction for azimuthal wavenumbers up to $k_\theta/2\pi \simeq +50 \text{ m}^{-1}$ at frequencies up to $f \simeq 150 \text{ kHz}$.

We can consider these disturbances in the context of drift waves and make comparisons to the linearized model developed by Kapulkin and Guelman (2008) and further extended by Frias et al. (2012). Frias uses a linearized small-amplitude fluctuation (i.e., perturbation analysis) model to describe drift waves driven by axial gradients in the plasma density n_e and magnetic field $\mathbf{B} \simeq B_r \hat{r}$. For the conditions simulated here, the simulated wave characteristics $k_z(f)$ and $k_\theta(f)$ appear to be consistent with the dispersion relation $\omega(k_z, k_\theta)$

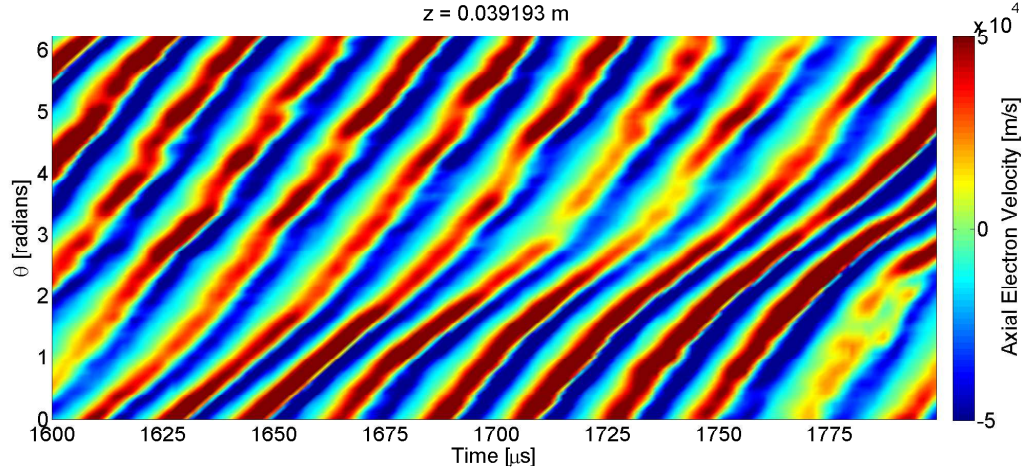


Figure 6.9: Azimuthal streak plot of axial electron velocity u_{ez} at axial location $z \simeq 0.04$ m (mid-channel), shown for time duration $t = 1600 \mu\text{s} - 1800 \mu\text{s}$ with $\Delta\theta = 2\pi/100$.

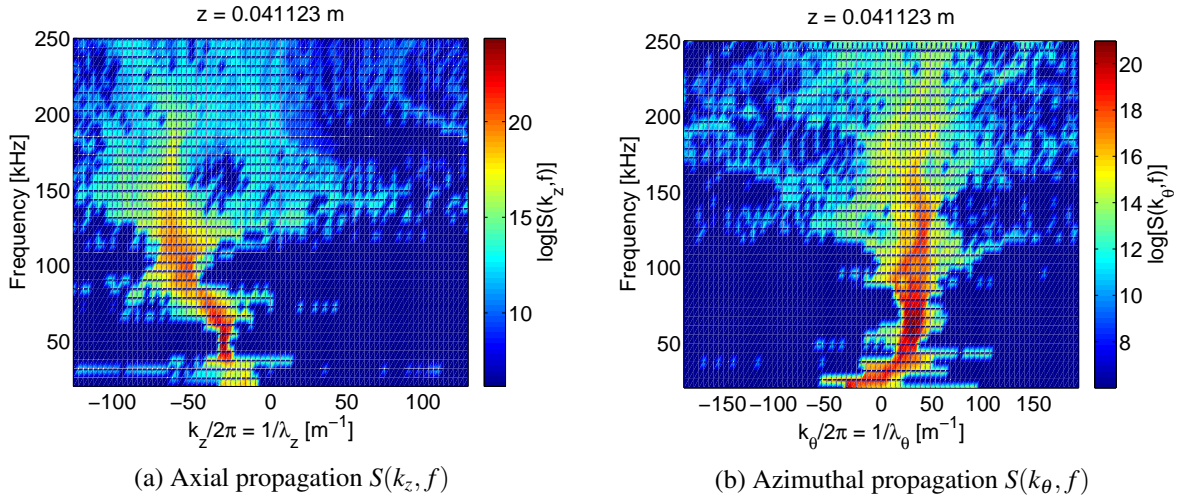


Figure 6.10: Simulated dispersive wave propagation at $z \simeq 0.04$ m. Analysis performed for $t = 1600 \mu\text{s} - 1800 \mu\text{s}$ with $\Delta\theta = 2\pi/100$, sampled at $T_{\text{samp}} = 1 \mu\text{s}$ ($f_{\text{max}} = \frac{1}{2}f_{\text{Nyq}} = 250$ kHz).

described by Frias et al. (2012); however according to the Frias model, it is unclear whether these waves can generate significant current. At these fairly low frequencies and wavenumbers $k_z(f)$ and $k_\theta(f)$, the Frias model predicts neither significant current nor significant growth of these particular instability modes $k_z(f)$ and $k_\theta(f)$. From the calculated effective electron mobility, shown in Fig. 6.5, we see that the anomalous fluctuation-induced electron current leads to some enhancement over the classical mobility in this region; further analysis and investigation of alternate transport (i.e., dispersive wave propagation) models may be warranted to determine whether and by what mechanism these waves generate anomalous transport.

6.2.3 Near Exit Plane ($0.07 \text{ m} \leq z \leq 0.08 \text{ m}$)

Inside the thruster channel near the exit plane for $0.07 \text{ m} \leq z \leq 0.08 \text{ m}$, we observe wave structure of much higher azimuthal wavenumber k_θ , i.e., shorter azimuthal wavelength λ_θ . In the axial direction, the simulated waves propagate in the positive z -direction at wavenumbers up to $k_z/2\pi \simeq 30 \text{ m}^{-1}$ and frequencies up to $f \simeq 150 \text{ kHz}$, as indicated by Fig. 6.11a. In the azimuthal direction, we observe propagation in both the positive and negative θ -directions. From the streak plot Fig. 6.13a shown for the time duration $t = 1600 \mu\text{s} - 1800 \mu\text{s}$, we observe a dominant mode which propagates in the positive θ -direction; however, on shorter timescale, e.g., $t = 1700 \mu\text{s} - 1750 \mu\text{s}$ as shown in Fig. 6.13b, we also observe wave structures which propagate in the negative θ -direction and others which appear constant in θ , i.e., which propagate only in the axial direction and not in the azimuthal direction. Figure 6.11b indicates negative azimuthal wavenumbers as low as $k_\theta/2\pi \simeq -50 \text{ m}^{-1}$ at very low frequencies ($f \leq 10 \text{ kHz}$) and positive azimuthal wavenumbers up to $k_\theta/2\pi \simeq 60 \text{ m}^{-1}$ at frequencies up to $f \simeq 200 \text{ kHz}$. From Fig. 6.12, we also observe low wavenumber propagation in the positive axial and positive azimuthal directions, with $k_z/2\pi \lesssim 10 \text{ m}^{-1}$ and $k_\theta/2\pi \lesssim 20 \text{ m}^{-1}$, at frequencies up to $f \simeq 8 \text{ MHz}$.

From Fig. 6.14b, we see that the anomalous fluctuation-induced electron current contribution in this region is negative, i.e., it opposes or reduces the classical electron current. Figure 6.14a depicts the axial electron shear $s = \partial u_{ez}/\partial z$; we see that there is strong negative shear (i.e., negative values of large magnitude for the axial shear) in this region. Shear is

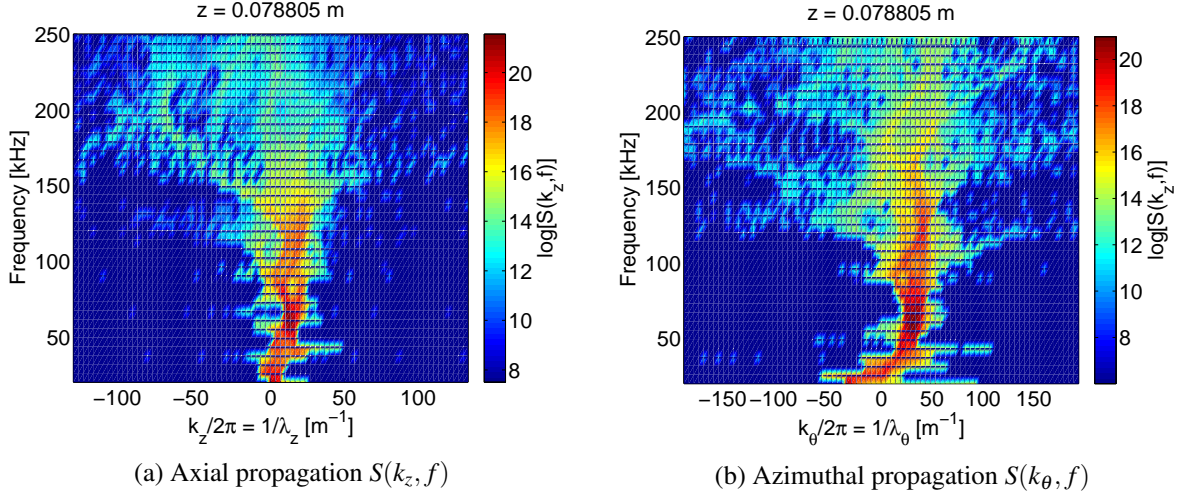


Figure 6.11: Simulated dispersive wave propagation at $z \simeq 0.079$ m. Analysis performed for $t = 1600 \mu\text{s} - 1800 \mu\text{s}$ with $\Delta\theta = 2\pi/100$, sampled at $T_{\text{samp}} = 1 \mu\text{s}$ ($f_{\text{max}} = \frac{1}{2}f_{\text{Nyq}} = 250$ kHz).

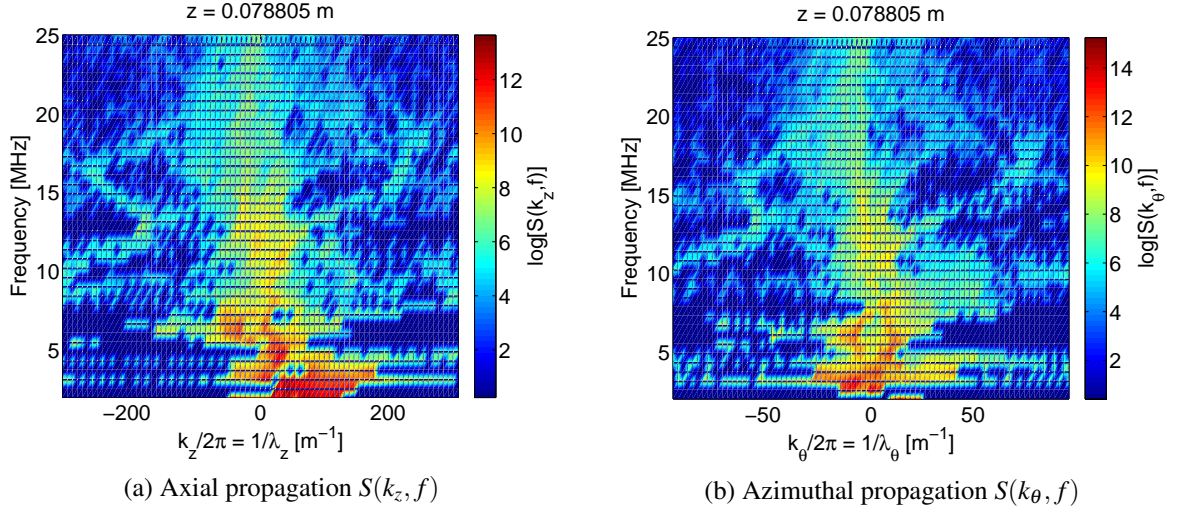


Figure 6.12: Simulated dispersive wave propagation at $z \simeq 0.079$ m. Analysis performed for $t = 1600 \mu\text{s} - 1602 \mu\text{s}$ with $\Delta\theta = 2\pi/50$, sampled at $T_{\text{samp}} = 10$ ns ($f_{\text{max}} = \frac{1}{2}f_{\text{Nyq}} = 25$ MHz).

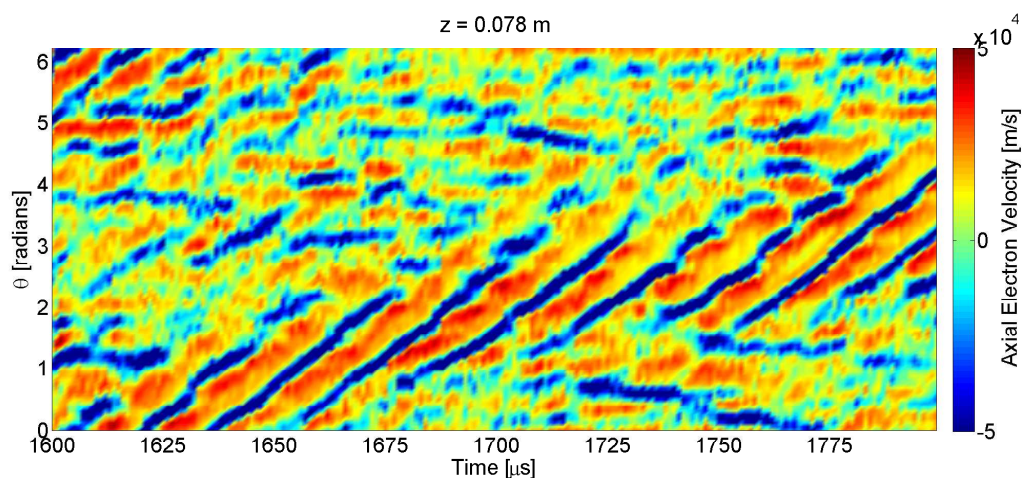
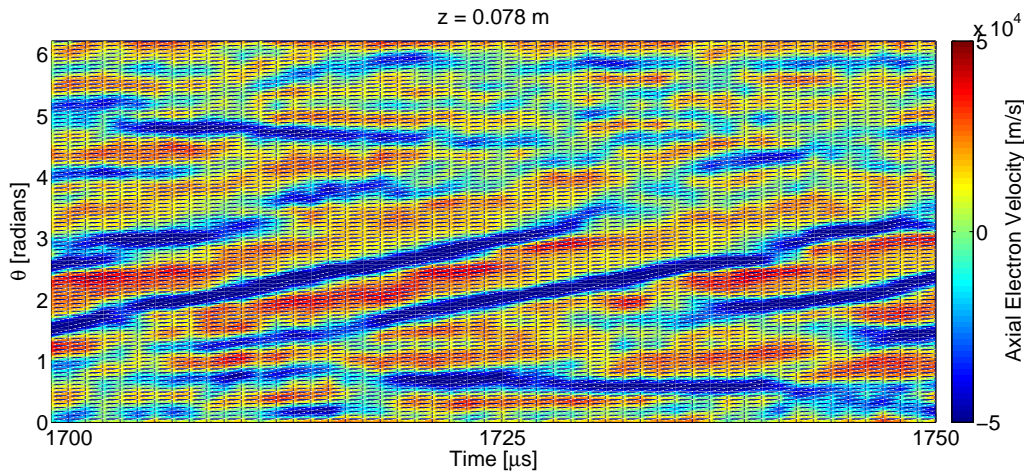
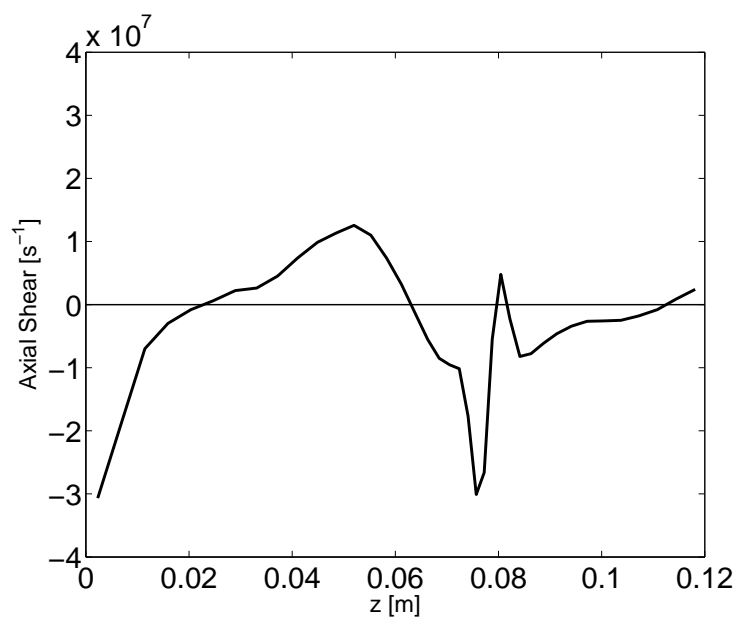
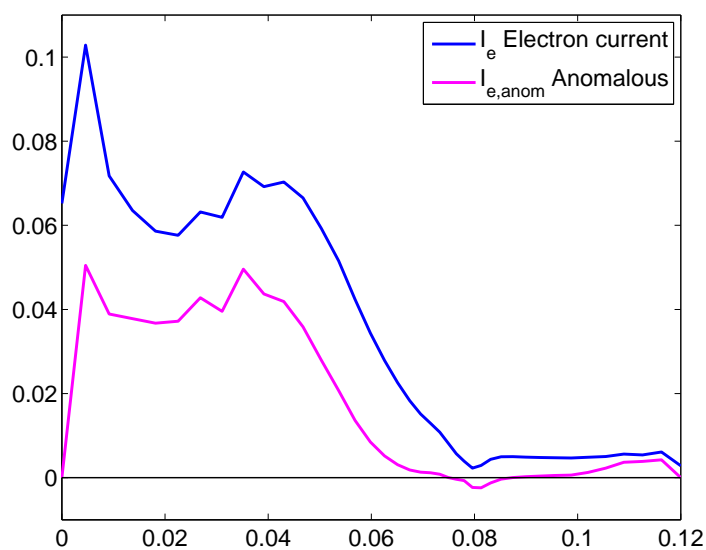
(a) $t = 1600 \mu\text{s} - 1800 \mu\text{s}$ (b) $t = 1700 \mu\text{s} - 1750 \mu\text{s}$

Figure 6.13: Azimuthal streak plots of axial electron velocity u_{ez} at axial location $z = 0.078 \text{ m}$ (just upstream of exit plane), shown for various time durations with $\Delta\theta = 2\pi/100$.

(a) Axial shear $\frac{\partial v_{e\theta}}{\partial z}$ 

(b) Anomalous contribution to electron current

Figure 6.14: Effect of axial shear on anomalous electron transport. Axial profiles have been time averaged over the interval $t = 1600 \mu\text{s} - 1800$ for simulation with $\Delta\theta = 2\pi/100$.

believed to play a role in fluctuation-induced transport; it can serve to disrupt correlated fluctuations and coherent wave structure, resulting in reduced electron transport.

We consider the small signal model and dispersion relations $\omega(k)$ developed by Thomas (2006). It appears that the simulated waves in this region may be consistent with the streaming instability described by Thomas. For the conditions simulated here, the Thomas model predicts pairs of azimuthally counter-propagating instabilities, including one at lower frequencies ($f \simeq 100$ kHz - 800 kHz) for low azimuthal wavenumbers k_θ , similar to the simulated $k_\theta(f)$ observed here for $f \simeq 200$ kHz; however, it is not clear whether this low frequency instability grows or decays, nor is it clear whether this propagation mode generates positive or negative current. The Thomas model predicts another instability at higher frequencies ($f \simeq 1$ MHz - 6 MHz) which appears to be consistent with that shown in Fig. 6.12b; however, again, it is unclear whether this mode grows or decays and whether it generates positive or negative current. The Thomas model also predicts instabilities at even higher frequencies ($f \simeq 1.5$ GHz) and higher wavenumbers $k_z(f)$ and $k_\theta(f)$ than those simulated here; however, it may be that finer time resolution and finer spatial resolution are required to simulate these higher frequency and higher wavenumber instabilities.

It is possible that the resulting macroscopic effect of counter-propagating waves, which can destructively interfere with (i.e., cancel) each other, is a perceived azimuthally-standing or slowly azimuthally-propagating wave; the counter-propagating waves can combine to create an aliased version (of the original two waves) which appears as a single, slower-moving fluctuation. Based on the Thomas model with the simulated conditions in this region, it is clear that the axial shear plays a significant role in determining the predicted propagation characteristics and resulting anomalous current. For the azimuthal wavenumbers frequencies $k_\theta(f)$ simulated here, the Thomas model does, in some cases, predict a growing instability which generates negative fluctuation-induced current.

From Figs. 6.4 and 6.5b, it is clear that the fluctuation-induced anomalous transport in this region generates negative current and results in a pronounced transport barrier near the channel exit plane; it is likely that the axial shear plays a role in creating this transport barrier, as evidenced by the coincident significant shear in these region. It may be that azimuthally counter-propagating instabilities exist in the region, complicating the analysis and observation of the resulting fluctuations.

6.2.4 Outside Channel ($z > 0.08$ m)

Outside the thruster channel for $z > 0.08$ m, we observe a disturbance that propagates in the positive z -direction and positive θ -direction, as shown in Fig. 6.15; this disturbance appears to be similar to that observed just inside the exit plane ($0.07 \text{ m} \leq z \leq 0.08 \text{ m}$). However, at shorter timescale as shown in Fig. 6.15b, we also observe azimuthally-standing structures (i.e., structures which propagate only in the positive z -direction and do not propagate in the θ -direction) and azimuthal propagation in the negative θ -direction. There also appears to be an unsteady advection of the electron flow in the positive axial direction; this phenomenon manifests as azimuthally-standing (or very low azimuthal velocity) structures which persist with significant magnitude for only a limited time duration, e.g., for $t = 1705 \mu\text{s} - 1725 \mu\text{s}$ at $\theta \simeq 4.5$ radians in Fig. 6.15b.

From Figs. 6.14b and 6.5, we see that there is positive anomalous current of small magnitude and some electron current enhancement in this region, especially for $0.10 \text{ m} \leq z \leq 0.12 \text{ m}$. It has been suggested that small spatial scale, high-frequency turbulence in this region can contribute to enhanced electron transport. However, it is difficult to make strong assertions regarding the anomalous current and simulated wave structures in this region. In our model formulation, there is little distinction between the computational domain and simulated conditions inside and outside the thruster channel; aside from the decreased magnetic field strength which results in decreased magnetic confinement outside the channel, there is no significant difference in the simulated plasma or model treatment outside the channel (compared to the portion of the domain that is inside the thruster channel). The decreased magnitude of the axial shear in this region points to the possibility of anomalous electron transport, i.e., mobility enhancement, in this region; however, since we do not simulate the radial expansion of the discharge plume, the cathode electron flow, or other salient features of the plume dynamics, we hesitate to draw strong conclusions from the simulated results in this region.

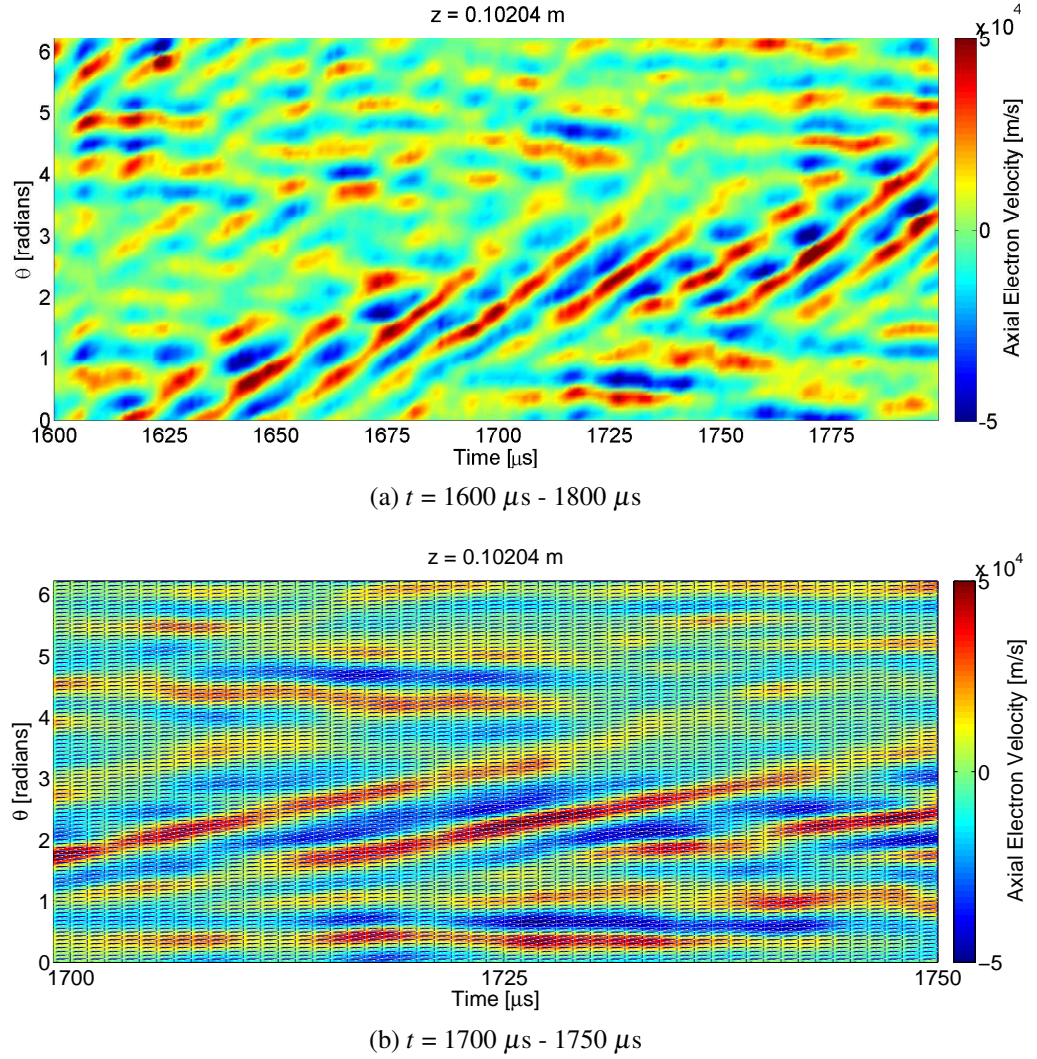


Figure 6.15: Azimuthal streak plots of axial electron velocity u_{ez} at axial location $z \simeq 0.10 \text{ m}$ (outside channel), shown for various time durations with $\Delta\theta = 2\pi/100$.

6.3 Summary

The simulation predicts a rich variety of quasi-coherent wave fluctuations which propagate at various frequencies and wavenumbers in the axial and azimuthal directions. We can identify four distinct axial regions which exhibit distinct wave structure and propagation characteristics. In the mid-channel region ($0.02 \text{ m} \leq z \leq 0.06 \text{ m}$) and outside the channel ($z \geq 0.10 \text{ m}$), appropriately-correlated fluctuations in the electron number density and axial electron velocity serve to enhance axial electron transport, resulting in an effective axial mobility that is higher than the classical mobility in those regions. Inside the channel near the exit plane ($0.07 \text{ m} \leq z \leq 0.08 \text{ m}$), it appears that fluctuations may, in fact, reduce the magnitude of the total electron current to create a transport barrier near the exit plane.

The dispersion characteristics (i.e., wavenumbers and frequencies) of the mid-channel ($0.02 \text{ m} \leq z \leq 0.06 \text{ m}$) waves appear to be consistent with gradient-driven drift waves, as suggested by Frias et al. (2012); near the exit plane ($0.07 \text{ m} \leq z \leq 0.08 \text{ m}$), the simulated waves bear some resemblance to the streaming instability described by Thomas (2006). Near the anode, we observe a simulated disturbance similar to the experimentally-observed rotating spoke phenomenon.

While the simulated fluctuations appear to contribute to both enhancement and reduction of the electron mobility consistent with some of the axial variation in the experimentally-measured electron mobility, the simulated fluctuation-induced transport does not appear to fully account for the total effective electron mobility observed in experiments. This leads us to conclude that some additional mechanism or transport model is needed to account for the remaining super-classical experimental mobility; we expect that additional physics (i.e., the inclusion and modeling of additional physical phenomena) may be required to generate the additional mobility enhancement required to match the experimentally-measured mobility.

We consider the relevant approximations and assumptions in our model. A key simplification is the exclusion of radial dynamics and wall effects, which may contribute to enhanced electron transport. The neglected plasma interactions with the walls could account for the missing electron transport enhancement required to address the gap between the

predicted fluctuation-induced transport and total experimentally-measured effective electron mobility.

Chapter 7

Enhanced Collision Frequency (Additional Results)

7.1 Electron Mobility Enhancement due to Wall Interactions

The so-called near wall conductivity, due to electron interactions with the thruster channel wall, was proposed early on (Morozov, 1968) as a mechanism to explain the experimentally-observed super-classical cross-field electron mobility, i.e., electron mobility in the direction perpendicular to the magnetic field. The premise is that electron collisions with the walls can disrupt the electron cyclotron motion and result in enhanced electron movement across the magnetic field lines in the direction perpendicular to the magnetic field.

As the theory for the near wall conductivity was further developed (Bugrova et al., 1992; Morozov and Savelyev, 2000), laboratory experiments have provided evidence that the thruster walls, e.g., wall material, can have a significant effect on cross-field electron mobility (Gascon et al., 2003). Further theoretical work and numerical simulations (Barral et al., 2003) have shown that both electron scattering (backscattering) and secondary electron emission (SEE) at the walls can contribute to enhanced electron mobility near the

channel walls. Most recently (Sydorenko et al., 2008), it has been suggested that an instability in the plasma sheath near the wall (more specifically, fluctuations in the near-wall electric potential within the plasma sheath) can influence secondary electron emission and result in significant near wall conductivity and cross-field electron transport.

In all cases, the near wall conductivity, i.e., the additional conductivity due to electron interactions with the thruster channel walls and the near-wall plasma sheath, is shown to contribute to the cross-field electron mobility. In our 2D z - θ model, we do not model the radial (r) direction; our model, thus, does not include the effect of electron, or plasma, interactions with the outer and inner radial channel walls. As such, it is likely that we are underestimating the realistic electron collision frequency; while we model effective electron collisions with neutrals, we neglect electron collisions with the walls. We believe that at least some of the discrepancy between our simulated electron mobility and the experimentally-measured results can be attributed to the neglected wall interactions.

7.2 Enhanced Collision Frequency

As an ad hoc means to account for the additional electron transport not captured by the existing model, we introduce an enhanced collision frequency. The collision frequency enhancement is intended to address the discrepancy between the simulated electron transport and the experimentally-measured electron mobility. Wall effects and scattering have been shown to contribute to an increased electron conductivity near the channel walls; we use the enhanced collision frequency as a proxy for these wall effects and any other collisional mobility-enhancing mechanisms that are not otherwise explicitly included.

We use a simple implementation for the enhanced collision frequency, which requires minimal modification to the existing model. The enhanced collision frequency is used as a simulation tool (parameter) to investigate the effect of (i.e., characterize the effective mobility discrepancy due to) the wall scattering and other collisional or conductivity effects not explicitly modeled here. We do not expect that this simple implementation will provide a precise or accurate model; however, the simulations provide a rough quantitative and qualitative appreciation for the effect of such additional conductivity mechanisms.

7.2.1 Model Implementation

We introduce a constant additional collision frequency contribution ν_{add} throughout the domain. In the electron fluid equations 3.48a, 3.48b, and 3.51a-3.51b, we replace all instances of the electron-neutral collision frequency ν_{en} with the effective collision frequency

$$\nu_{eff} = \nu_{en} + \nu_{add} \quad (7.1)$$

where ν_{en} is calculated, as before, according to Eqn. 3.22 and ν_{add} is prescribed as a simulation parameter which is constant in space and constant in time.

The collision frequency appears several times throughout the electric potential ϕ , electron velocity (u_{ez} and $u_{e\theta}$), and electron temperature T_e equations – notably, in the cross-field electron mobility μ_{\perp} (Eqn. 3.21a), the corresponding diffusion constant D_{\perp} (Eqn. 3.21b), the electron velocity expressions u_{ez} and $u_{e\theta}$ (Eqns. 3.51a-3.51b), and the electric potential ϕ (Eqn. 3.48b) coefficients $\{A_1, A_2, \dots, A_5\}$ (Eqns. 3.45a-3.45e and 3.46); in the electron temperature T_e equation (3.48a), the collision frequency appears in the diffusive (Eqn. 3.49c) and Joule heating (Eqn. 3.49d) terms. In each case, i.e., for each of these expressions or equations described in Chap. 3, the electron-collision frequency ν_{en} is replaced by the enhanced effective collision frequency ν_{eff} .

7.2.2 Effect of Collision Frequency Enhancement (ν_{add})

In an attempt to match the experimentally-measured property data and roughly quantify the impact of the collision frequency enhancement, we performed simulations with a range of ν_{add} values. For the original simulation with $\nu_{add} = 0$ (i.e., the simulation results presented in Chap. 5), the time-averaged electron-neutral collision frequency ν_{en} is on the order of 10^7 s^{-1} . We expect that ν_{add} must be of the same order of magnitude to contribute appreciably to ν_{eff} and have any significant impact on electron transport.

For a lower bound on ν_{add} , we consider the work of Boeuf and Garrigues (1998) and Fife (1999). In similar 1D hybrid simulations described by Boeuf and Garrigues (1998), an additional constant collision frequency term ν_{walls} is used to account for the electron-wall

interactions and resulting electron conductivity enhancement; for these 1D (axial) simulations of a thruster of comparable channel width, the value $v_{walls} = 2 \times 10^6 \text{ s}^{-1}$ was chosen to match experimental results. Fife (1999) presents a more detailed analysis of electron interactions with the channel walls; based on this detailed analysis, we can calculate a wall collision frequency $v_{wall} = 10^5 - 10^6 \text{ s}^{-1}$ for the range of electron temperatures simulated and experimentally-measured here. We choose a lower bound of $v_{add} = 10^6 \text{ s}^{-1}$; we expect any smaller v_{add} value will have negligible impact on the total effective collision frequency v_{eff} and the resulting electron transport.

For an upper bound on v_{add} , we consider the maximum possible frequency for electron collisions with the walls, based on the mean electron speed. To roughly estimate the electron speed, we consider the electron temperature T_e ; for the peak experimentally-measured electron temperature $T_e = 7 \text{ eV}$, the mean electron speed is $\bar{c}_e = \sqrt{8k_B T_e / \pi m_e} \simeq 2 \times 10^6 \text{ m/s}$. If we consider the channel width $W = r_{outer} - r_{inner} = 0.012 \text{ m}$, we can estimate a maximum collision frequency $v_{max} = \bar{c}_e / W \simeq 1.5 \times 10^8 \text{ s}^{-1}$. This is an absolute maximum collision frequency, based on the assumption that each electron traverses the channel width and strikes the wall. In reality, only a small percentage of electrons, typically the more energetic, i.e., higher velocity, electrons strike the wall. There is an electron-repelling plasma sheath that develops near the channel walls; in order to strike the wall, an electron must overcome the sheath potential. Only the most energetic electrons can overcome the sheath potential to strike the wall; hence, the actual collision frequency, and resulting electron scattering at the walls, is significantly lower than our estimated v_{max} . For purposes of comparison, we use $v_{add} = 10^8 \text{ s}^{-1}$ as an upper bound.

Using simulation parameter values similar to those in Table 5.2, we performed simulations with v_{add} over the range $v_{add} = 10^6 \text{ s}^{-1} - 10^8 \text{ s}^{-1}$. Figure 7.1 provides a comparison of the time-averaged simulation results. Figure 7.1a provides a comparison of the effective collision frequency $v_{eff} = v_{en} + v_{add}$ for each case; Fig. 7.1b shows the corresponding time-averaged electron number density profiles $\bar{n}_e(z)$, as compared to the experimentally-measured values. For the $v_{add} = 10^6 \text{ s}^{-1}$ simulation, the time averages were taken over the last 300 μs of the simulation; for all other values of v_{add} (including $v_{add} = 0$), the time averages were taken over the last 500 μs of each simulation.

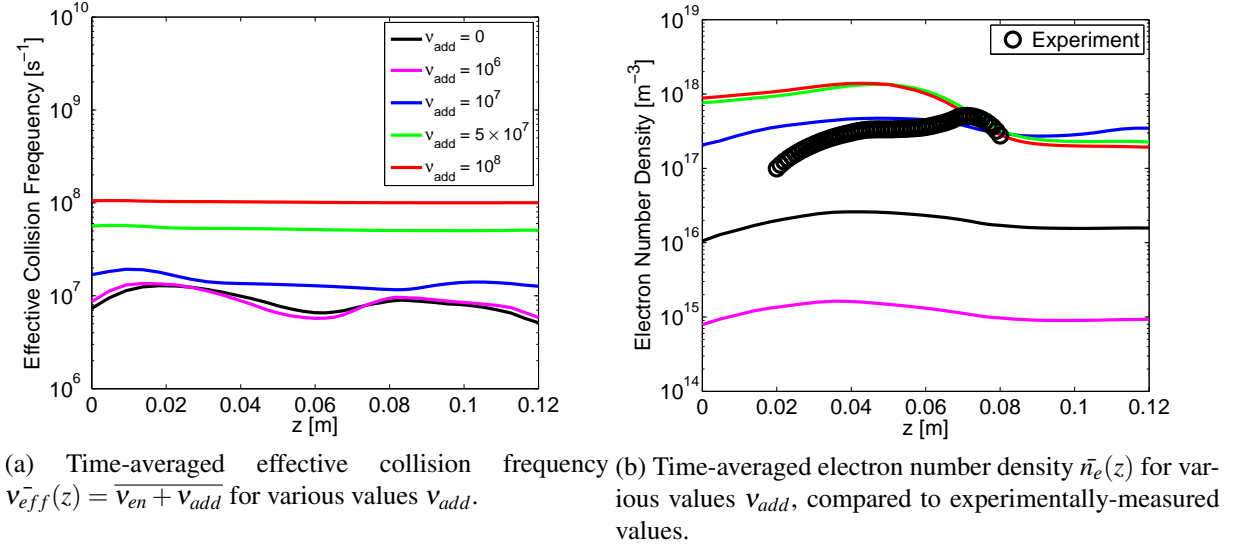


Figure 7.1: Comparison of simulation results for various values $v_{add} = 10^6 \text{ s}^{-1} - 10^8 \text{ s}^{-1}$.

For $v_{add} = 10^6 \text{ s}^{-1}$, the effect of the collision enhancement is insignificant compared to the electron-neutral collision frequency ν_{en} ; the effective collision frequency ν_{eff} is dominated by the ν_{en} term, i.e., $v_{add} \ll \nu_{en}$ and $\nu_{eff} \simeq \nu_{en}$, so the collision frequency enhancement v_{add} has almost no effect. As shown in Fig. 7.1a, the effective collision frequency ν_{eff} is nearly identical for the $v_{add} = 0$ and $v_{add} = 10^6 \text{ s}^{-1}$ cases; the $v_{add} = 10^6 \text{ s}^{-1}$ simulation, in fact, predicts a lower electron number density than the $v_{add} = 0$ simulation, as shown in Fig. 7.1b.

For $v_{add} = 5 \times 10^7 \text{ s}^{-1}$ and $v_{add} = 10^8 \text{ s}^{-1}$, the collision frequency enhancement dominates the effective collision frequency, i.e., $v_{add} \gg \nu_{en}$ and $\nu_{eff} \simeq v_{add}$. In these cases, v_{add} is responsible for almost all the electron transport; the collision frequency enhancement becomes the dominant electron transport mechanism, obscuring the role of the anomalous fluctuation-driven transport contributions. The electron transport becomes primarily a function of the prescribed value v_{add} ; while v_{add} could be used as a simulation parameter to match the experimental measurements, this would lead to a tuned model, which would be counter to the purpose of our work here and would preclude the use of our simulation as a tool for characterizing the effects of fluctuation-induced anomalous electron transport. The predicted electron number density values for $v_{add} = 5 \times 10^7 \text{ s}^{-1}$ and $v_{add} = 10^8 \text{ s}^{-1}$ are

significantly higher than the experimentally-measured values, especially inside the thruster channel for $z \lesssim 0.06$ m, as shown in Fig. 7.1b.

For $\nu_{add} = 10^7 \text{ s}^{-1}$, the simulated electron number density is comparable to the experimentally-measured values. The collision frequency enhancement ν_{add} is comparable to, i.e., of the same order of magnitude as, ν_{en} ; both terms contribute comparably to the effective collision frequency ν_{eff} . The contribution from ν_{add} is significant and clearly impacts the plasma property profiles and overall electron transport, as will be shown in Sect. 7.3; however, the fluctuation-induced anomalous transport is of comparable significance.

Overall, $\nu_{add} = 10^7 \text{ s}^{-1}$ appears to provide a reasonable fit to experimentally-measured data, both in the magnitude and axial variation (profile shapes) of the most relevant plasma properties. The value $\nu_{add} = 10^7 \text{ s}^{-1}$ falls within the expected range for the electron-wall collision frequency $10^6 \text{ s}^{-1} \leq \nu_{wall} \leq 10^8 \text{ s}^{-1}$ and is a reasonable choice to represent the wall scattering and near wall conductivity effect. Note that the purpose of these particular simulations is not to precisely match or predict thruster operation, but to provide qualitative (and roughly quantitative, i.e., order or magnitude) insight into the level of missing transport or collision frequency enhancement required to address the discrepancy between the (un-enhanced) simulation results and the experimentally-measured values (i.e., experimental mobility and plasma property profiles). While the exact value of ν_{add} could be further fine tuned (e.g., $\nu_{add} = 1 - 3 \times 10^7 \text{ s}^{-1}$ or $\nu_{add} = \nu_{add}(z)$), the constant value $\nu_{add} = 10^7 \text{ s}^{-1}$ provides a fairly good, i.e., comparable to experiment, prediction of plasma properties and trends, while still enabling the study of fluctuations and the relative classical and anomalous contributions to electron transport.

7.3 Simulation Results for $\nu_{add} = 10^7 \text{ s}^{-1}$

We present updated simulation results, similar to those presented in Chaps. 5 and 6; the only difference between the simulation presented here and that presented in Chap. 5 is the introduction of the constant collision frequency enhancement ν_{add} via the effective collision frequency $\nu_{eff} = \nu_{en} + \nu_{add}$. Whereas the simulation described previously in Chap. 5 did not include any collision frequency enhancement (i.e., $\nu_{add} = 0$), for the

Table 7.1: Simulated operating condition for enhanced collision frequency simulation

Operating Parameter	Value
Xe neutral propellant mass flow rate (\dot{m}_n)	2.3 mg/s
Voltage at anode plane, $z = 0$ (Set by external power supply)	100 V
Voltage at cathode plane / “near” plume extent, $z = 0.12$ m (Measured)	30 V

simulation presented here, we use $v_{add} = 10^7 \text{ s}^{-1}$. We present a complete set of simulation results, with comparison to the the original ($v_{add} = 0$) case, where relevant.

7.3.1 Simulation Conditions

The simulated thruster operating condition is the same as before, as described by Table 5.1, repeated here as Table 7.1 for convenience. Table 7.2 lists the relevant simulation parameters. We use the same simulation parameters as before; the only change from the previous case is the slightly longer simulation duration and, of course, the inclusion of $v_{add} = 10^7 \text{ s}^{-1}$. We use the same numerical grid shown in Fig. 4.3a, which contains 40 points non-uniformly spaced in z and 50 points uniformly-spaced in θ , for a total of $40 \times 50 = 2000$ grid points; we also perform grid refinement in θ , as before, using an azimuthally-refined grid with 100 points uniformly-spaced in θ . As before, we use an outer loop time step $dt = 10 \text{ ns}$ with $N_{sub} = \frac{dt}{dt_{sub}} = 100$, which results in an inner loop time step $dt_{sub} = 0.1 \text{ ns}$. The simulation is time advanced over 200,000 outer loop time steps, which corresponds to 2 million inner loop time steps; the total simulated time extent is 2.0 ms of simulated time.

7.3.2 Plasma Properties

7.3.2.1 Initial Transient Behavior

As before, we observe an initial transient phase during which the plasma properties evolve from the initial conditions before eventually settling into a quasi-steady-state. Figures 7.2 - 7.5 illustrate the trends in various plasma properties during this initial transient phase. In each case, the property values have been averaged over θ to provide a θ -averaged axial

Table 7.2: Summary of simulation parameters for enhanced collision frequency simulation

Simulation Parameter	Value	Description
v_{add}	10^7	Collision frequency enhancement (constant in space and time)
dt	10 ns	Outer loop time step, used for particle time advancement and electric potential solution
$\Delta\phi = \phi_{z=0} - \phi_{z=0.12\text{ m}}$	70 V	Voltage difference between anode and downstream domain boundary, used to set electric potential boundary condition
ϵ	10^{-6}	Convergence tolerance for electrical potential solution
dt_{sub}	0.1 ns	Inner loop timestep, used for electron temperature time advancement
Boundary condition $T_e(z=0)$	$T_e = 17,500\text{ K}$ ($\sim 1.5\text{ eV}$)	Dirichlet boundary condition applied at anode plane
Boundary condition $T_e(z=0.12\text{ m})$	$\frac{\partial T_e}{\partial z} = 0$	Neumann boundary condition applied at downstream domain end
$T_{e,min}$	15,000 K ($\sim 1.3\text{ eV}$)	Enforced minimum electron temperature value throughout domain
$T_{e,max}$	120,000 K ($\sim 10.3\text{ eV}$)	Enforced maximum electron temperature value throughout domain
$\Delta_{max}T_e$	10 K ($\sim 8.6 \times 10^{-4}\text{ eV}$)	Enforced maximum change in electron temperature (at any given grid point) per electron timestep dt_{sub}
γ	1.0	Ionization cost factor for S_{ioniz} (Eqn. 3.49e)
Number of neutral particles	$\sim 400,000$	Time-averaged total number of simulated neutral superparticles in computational domain
Number of ion particles	$\sim 1.6\text{M} - 2.1\text{M}$	Time-averaged total number of simulated ion superparticles in computational domain
Number of grid points	2000	Grid with 40 points (non-uniform) in z and 50 points (uniform) in θ
Total simulated time	2.0 ms	Time extent of simulation (corresponds to 200,000 outer loop timesteps dt or 1.9M inner loop timesteps dt_{sub})
Total wall clock time	$\sim 210\text{ hours}$ ($\sim 8.38\text{ days}$)	Simulation execution time on a single Intel Xeon (E3-1245 v3) 3.40 GHz processor core

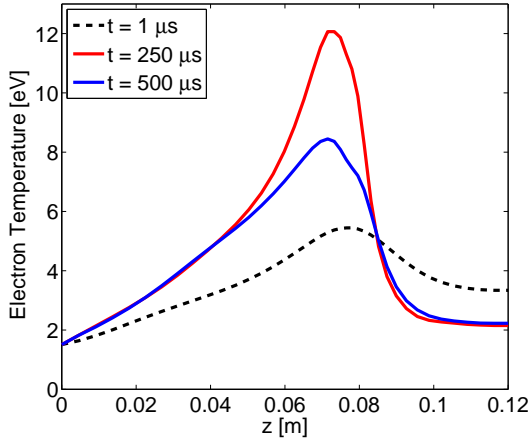


Figure 7.2: Electron temperature $T_e(z)$ at various times t .

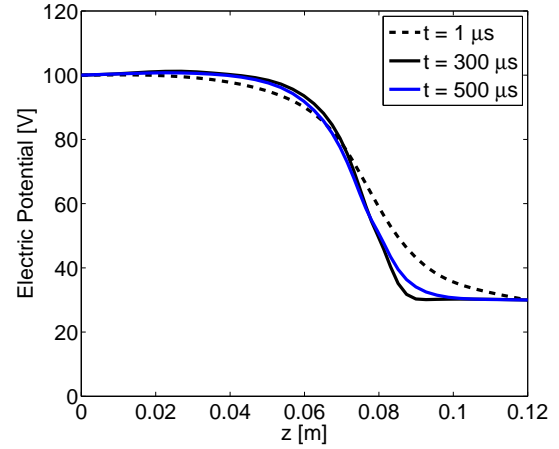


Figure 7.3: Electric potential $\phi(z)$ at various times t . (Shown relative to experimentally-measured potential $\phi(z = 0.12) = 30\text{V}$.)

profile of the property variation with z , e.g., $T_e(z)$; the respective figures show the time evolution of these axial property profiles by providing a comparison of the property profiles at various times, e.g., $T_e(z, t)$.

Overall, the plasma property profiles stabilize quickly, within the first $\sim 500 \mu\text{s}$ of the simulation. There is an initial surge in the electron temperature $T_e(z)$, as illustrated in Fig. 7.2. The electron temperature quickly reaches a maximum value of approximately 12 eV; at $t \simeq 250 \mu\text{s}$, the peak value (at the axial location $z \simeq 0.705 \text{ m}$) starts to decrease, eventually stabilizing to its quasi-steady value of approximately 8 eV by $t \simeq 500 \mu\text{s}$. Figure 7.3 shows the time evolution of the electric potential profile $\phi(z)$. The electric potential profile $\phi(z)$ stabilizes quickly, with the shape of the electric potential profile $\phi(z)$ – most notably, the slope and axial location potential fall region – mostly stabilized by $t \simeq 300 \mu\text{s}$. The time evolution of the axial electric field $E_z(z)$ and axial ion velocity $u_{iz}(z)$ is shown in Figs. 5.3a and 5.3c, respectively. The axial profile of the population average axial ion velocity $u_i(z)$, which is governed by the axial electric field $E_z = -\frac{\partial \phi}{\partial z}$, is mostly stabilized by $t \simeq 300 \mu\text{s}$ (i.e., when the electric potential profile $\phi(z)$ has stabilized). However, as before, there is a population of slow-moving (low velocity) ions, created by the ionization of slow-moving

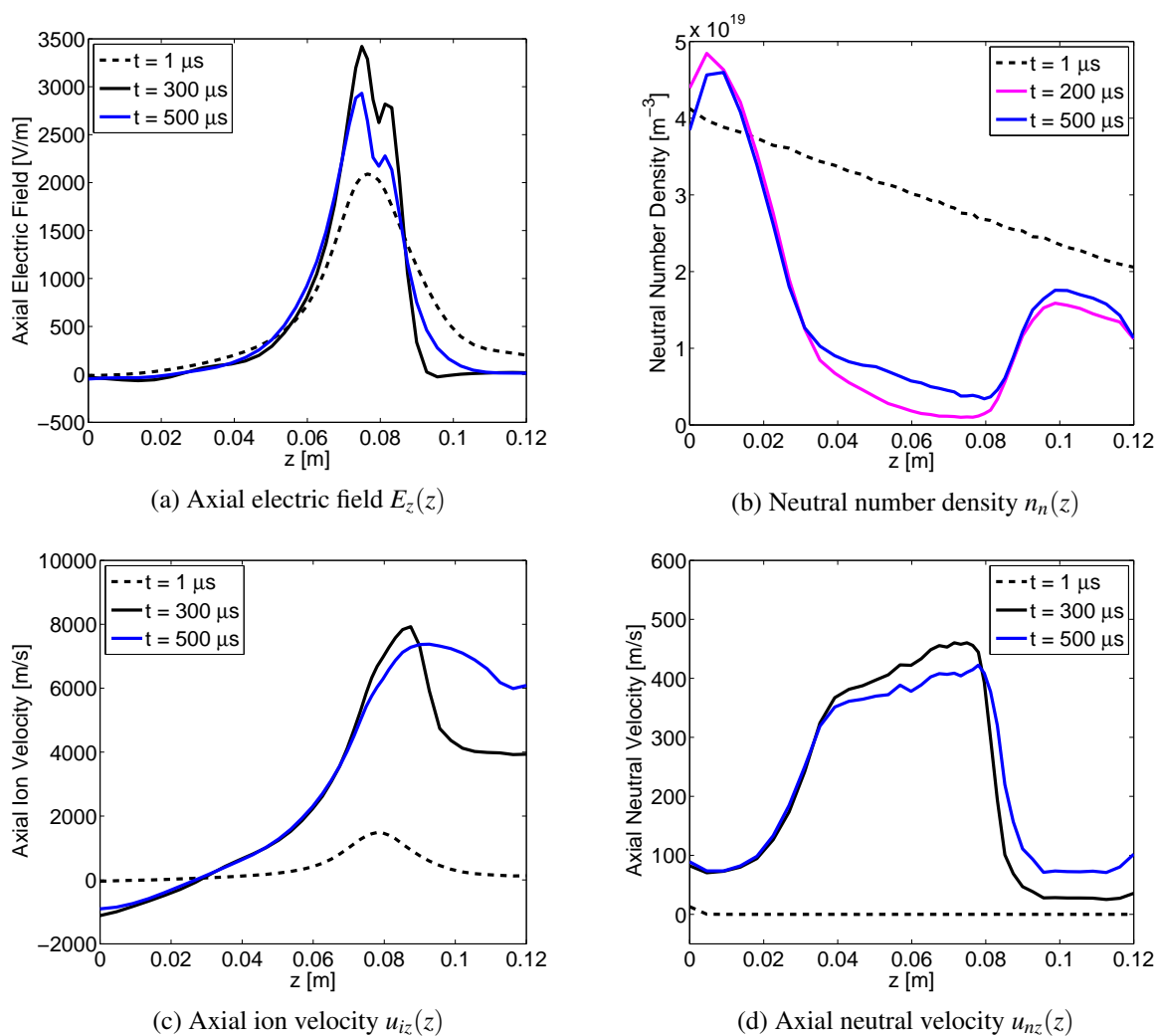


Figure 7.4: Axial electric field, axial ion velocity, neutral number density, and axial neutral velocity at various times t .

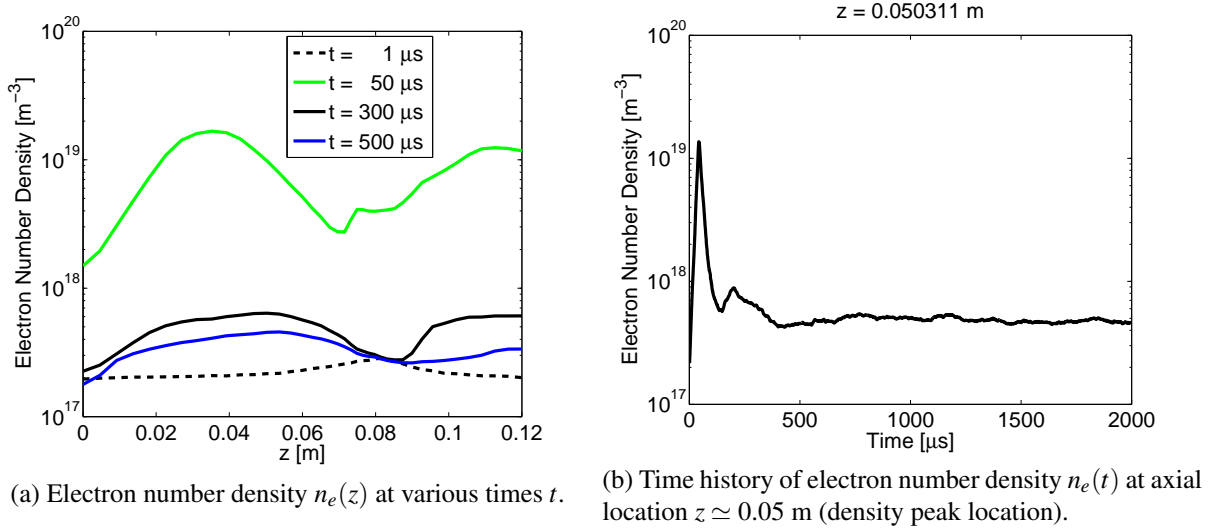


Figure 7.5: Electron number density profile and time history, shown on logarithmic scale.

(low velocity) neutrals, outside the channel exit ($z \gtrsim 0.1 \text{ m}$); the results is the observed dip in the tail of the population average ion velocity $u_i(z)$ for $z \gtrsim 0.1 \text{ m}$. By $t \simeq 500 \mu\text{s}$, the axial ion velocity has stabilized to its quasi-steady-state; for $t \geq 500 \mu\text{s}$, a shallow dip in the axial ion velocity tail persists. We attribute the decreased axial ion velocity in this region to the continuing preferential ionization of low velocity neutrals in this region.

Figures 7.4b and 7.4d show the time evolution of the neutral number density n_n and population average axial neutral velocity u_{nz} , respectively. In both cases, the general shape and profile features stabilize by $t \simeq 300 \mu\text{s}$; however, the extremum values (peak and minimum values) continue to evolve until they reach the quasi-steady-state shown for $t \simeq 500 \mu\text{s}$.

There is an initial surge in the plasma density (i.e., the electron density or ion density) $n_e = n_i$ during the first $\sim 50 \mu\text{s}$ of the simulation, as shown in Fig. 7.5; during this time, the magnitude of the plasma density rapidly increases as the axial profile shape develops, reaching its maximum value at $t \simeq 50 \mu\text{s}$. For $50 \mu\text{s} \lesssim t \lesssim 400 \mu\text{s}$, the magnitude of the plasma density steadily falls, decreasing by nearly two orders of magnitude, until it stabilizes to the quasi-steady-state profile shown for $t \simeq 400 \mu\text{s}$ in Fig. 7.5a; during this time, the profile shape $n_e(z)$ changes slightly as the axial location of the density peak shifts slightly downstream (from the initial peak location $z \simeq 0.03 \text{ m}$ shown for $t = 50 \mu\text{s}$ in Fig.

7.5a), resulting in the quasi-steady-state plasma density peak location $z \simeq 0.05$ m. Figure 7.5a shows the plasma density profile as it evolves to the eventual quasi-steady-state, and Fig. 7.5b shows the time history of the plasma density at the axial peak location $z \simeq 0.05$ m; note that, in both figures, the plasma density values $n_e(z, t)$ are shown on a logarithmic scale.

7.3.2.2 Quasi-steady Operation

By $t = 500 \mu\text{s}$, the simulated discharge has settled to its quasi-steady-state. For $t \geq 500 \mu\text{s}$, the remaining $1500 \mu\text{s}$ ($t = 500 \mu\text{s} - 2000 \mu\text{s}$) of simulated time represents quasi-steady thruster operation.

We can compare the time-averaged simulated axial property profiles to those for the $v_{add} = 0$ simulation and to the experimentally-measured values. Figures 7.6 - 7.8 show the time-averaged simulated axial property profiles for the $v_{add} = 0$ and $v_{add} = 10^7 \text{ s}^{-1}$ simulations, compared with the experimentally measured values. As before, the simulated properties are first averaged over θ to obtain the θ -averaged axial property profiles, e.g., $T_e(z, t)$, which are then time-averaged to obtain the time-averaged axial profiles, e.g., $\bar{T}_e(z)$; the $v_{add} = 10^7 \text{ s}^{-1}$ simulation results are time-averaged over the interval $t = 1000 \mu\text{s} - 2000 \mu\text{s}$, while the $v_{add} = 0$ results are time-averaged over the interval $t = 1300 \mu\text{s} - 1900 \mu\text{s}$.

In most cases, the $v_{add} = 10^7 \text{ s}^{-1}$ time-averaged profiles show improved agreement with the experimentally-measured values, compared to the $v_{add} = 0$ case. The electric potential profile $\bar{\phi}(z)$, shown in Fig. 7.6a, exhibits excellent agreement with the experimentally-measured values, especially in the acceleration region $0.07 \text{ m} \lesssim z \lesssim 0.08 \text{ m}$ where most of the potential fall and maximum axial electric field E_z occur; the potential fall region is shifted downstream, compared to that in the $v_{add} = 0$ case, and the slope and values of the time-averaged electric potential $\bar{\phi}$ align closely with the experimentally-measured values in this region. The simulated electron temperature profile $\bar{T}_e(z)$, shown in Fig. 7.6b, also shows good agreement with the experimentally-measured values; the peak temperature value of approximately 8.5 eV is comparable to the experimentally-measured peak of ~ 7 eV, and the axial location of the simulated temperature peak at $z \simeq 0.07$ m aligns well with the experimentally-measured peak location.

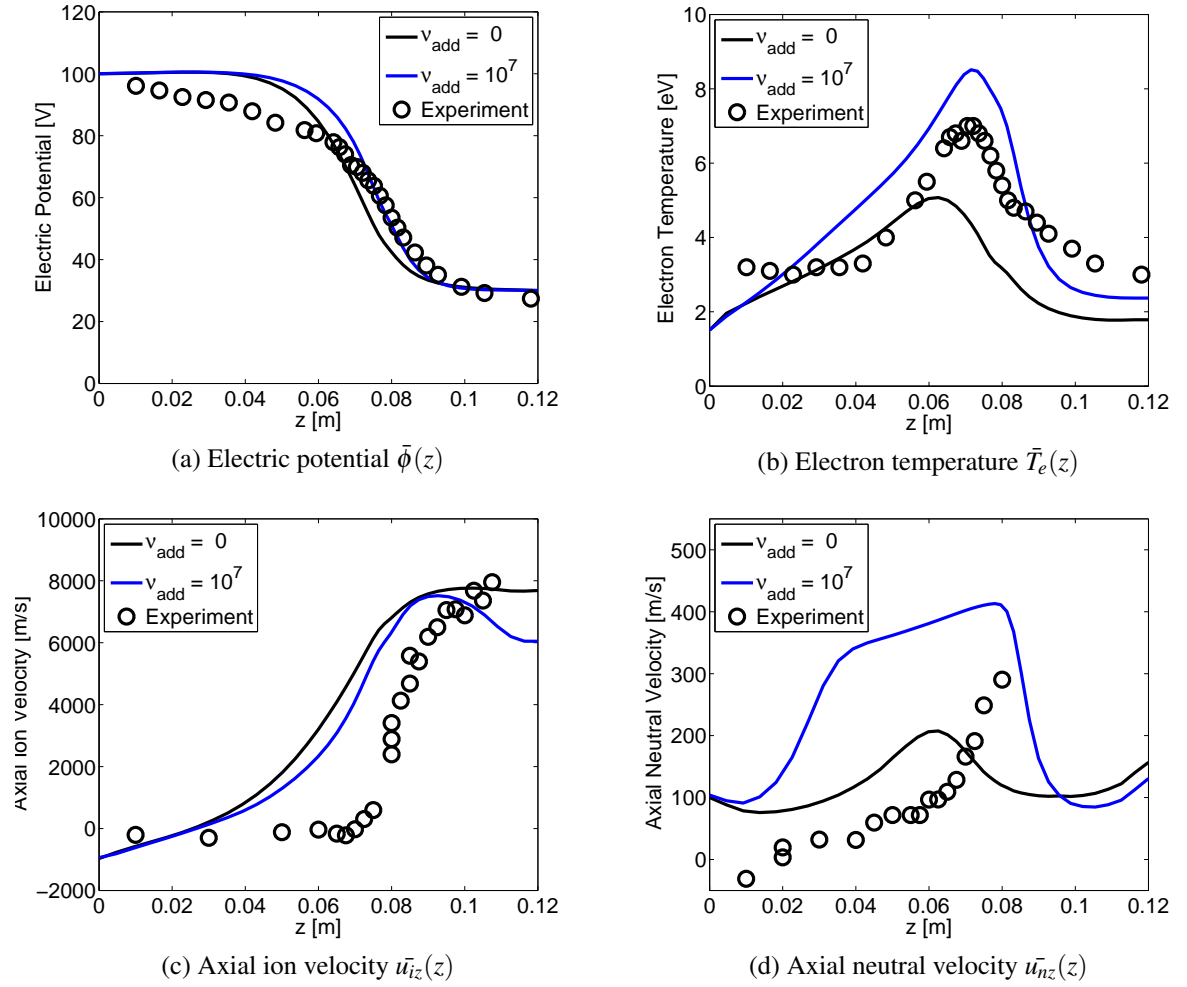
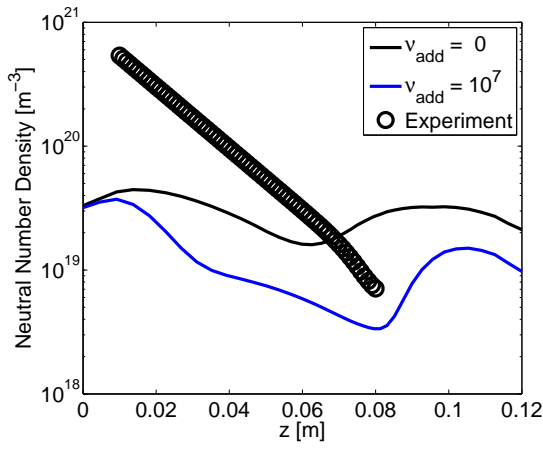
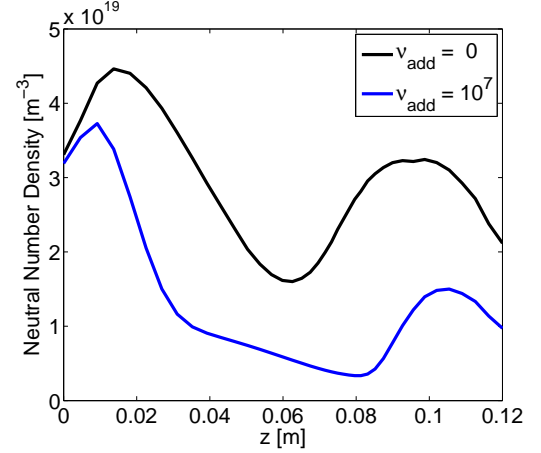


Figure 7.6: Time-averaged electric potential, electron temperature, axial ion velocity and axial neutral velocity profiles, compared with experimentally-measured values.

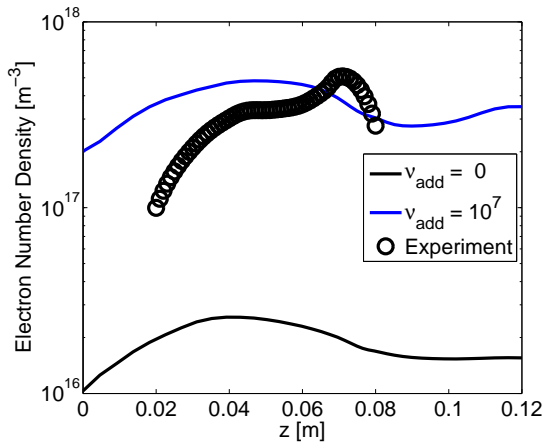


(a) Simulated and experimentally-measured values, shown on logarithmic scale.

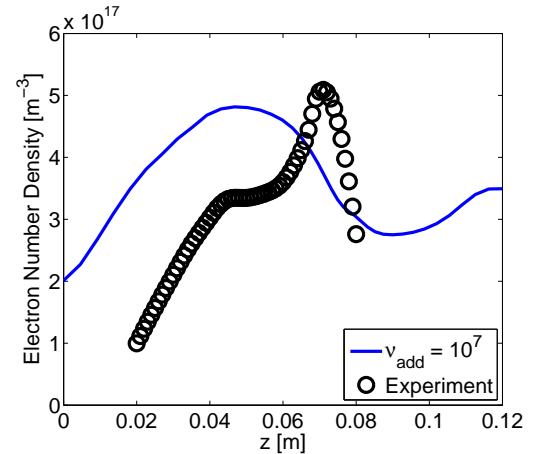


(b) Simulated profile shown on linear scale.

Figure 7.7: Time-averaged neutral number density profile $\bar{n}_n(z)$ compared with experimentally-measured values.



(a) Simulated and experimentally-measured values, shown on logarithmic scale.



(b) Simulated and experimentally-measured values, shown on linear scale.

Figure 7.8: Time-averaged electron number density profile $\bar{n}_e(z)$ compared with experimentally-measured values.

The simulated axial ion velocity profile $\bar{u}_{iz}(z)$, shown in Fig. 7.6c, is similar, if not slightly improved, compared to that for the $v_{add} = 0$ case. The acceleration region is shifted slightly downstream and the $\bar{u}_{iz}(z)$ profile in this region exhibits a slightly steeper slope, compared to the $v_{add} = 0$ case; however, there is a discrepancy, when compared to the experimentally-measured values which indicate a narrower acceleration near the exit plane at $z = 0.08$ m. Throughout the rest of the domain, the simulated values show reasonable agreement with the experimentally-measured values, with the exception of the dip in the simulated $\bar{u}_{iz}(z)$ profile tail for $z \gtrsim 0.01$ m. For $z \gtrsim 0.01$ m, the simulated \bar{u}_{iz} values are noticeably lower than both the experimentally-measured values and those for the $v_{add} = 0$ case; we attribute this decreased axial ion velocity to the continuing ionization of low velocity neutrals in this region. In general, we expect that low velocity neutrals will be preferentially ionized, compared to higher velocity ions which can move through this region and exit the domain more quickly. As shown in Fig. 7.6d, the axial neutral velocity values in this region are similar for the $v_{add} = 0$ and $v_{add} = 10^7 \text{ s}^{-1}$ cases; however, due to a slightly higher electron temperature and higher electron number density in the $v_{add} = 10^7 \text{ s}^{-1}$ case, we expect that the ionization rate in this region (given by Eqn. 3.8) is higher for the $v_{add} = 10^7 \text{ s}^{-1}$ case.

The simulated axial neutral velocity profile $\bar{u}_{nz}(z)$, shown in Fig. 7.6d, differs somewhat from the experimentally-measured values; however, it exhibits a similar general trend of increasing velocity values \bar{u}_{nz} with increasing z inside the channel ($z < 0.08$ m), as does the $v_{add} = 0$ case. For most of the domain, the simulated neutral density profile $\bar{n}_n(z)$, shown in Fig. 7.7, is slightly smaller in magnitude than that for the $v_{add} = 0$ case. For both simulated cases ($v_{add} = 10^7 \text{ s}^{-1}$ and $v_{add} = 0$), the simulated values are significantly lower than the experimentally-measured values; however, as discussed previously in Sect. 5.2.2, there is significant uncertainty in the experimentally-measured values.

Figure 7.8 shows the simulated electron number density, profile $\bar{n}_e(z)$. The simulated electron density profile exhibits good magnitude agreement with the experimentally-measured values and represents a significant improvement, compared to the $v_{add} = 0$ case. While the peak values of the simulated and experimentally-measured profiles are comparable, there is a discrepancy in the axial location of the density peak; the simulated profile $\bar{n}_e(z)$ exhibits a broad peak centered at $z \simeq 0.05$ m, while the experimental measurements

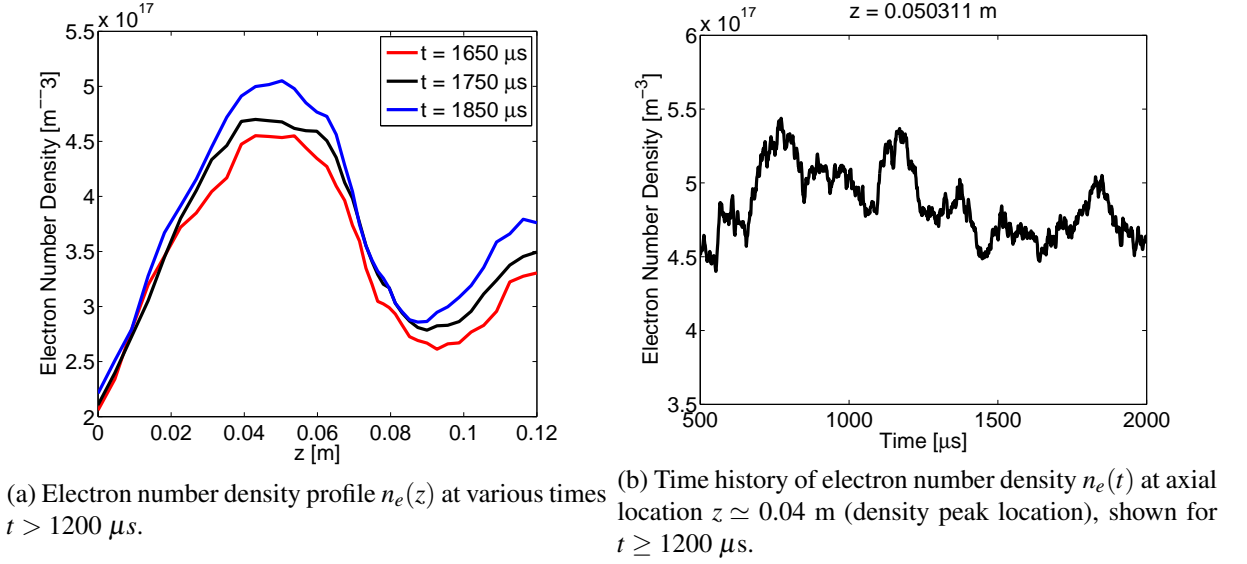


Figure 7.9: Fluctuating nature of electron number density during quasi-steady-state operation.

indicate a narrower peak farther downstream at $z \simeq 0.705$ m. Even so, the simulated profile represents an improvement compared to the $v_{add} = 0$ case; the peak location is shifted downstream, closer to the experimental peak location, compared to the $v_{add} = 0$ peak location at $z \simeq 0.04$ m, and the improved magnitude agreement with the experimental values is encouraging.

As before, the simulated quasi-steady-state is non-stationary; Fig. 7.9 illustrates the fluctuating nature of the electron number density. Similar sustained fluctuations, which can be characterized as small signal oscillations about a steady-state or time-averaged value, can be observed in most of the other plasma properties, including the electric potential ϕ and electron velocities u_{ez} and $u_{e\theta}$.

7.3.3 Discharge Current

As before, we are interested in the various contributions to the discharge current $I_D = I_e + I_i$. Figure 7.10 illustrates the time-fluctuating nature of the discharge current I_D . The early peak in the discharge current I_D , shown in Fig. 7.10a, corresponds to the initial surge in the

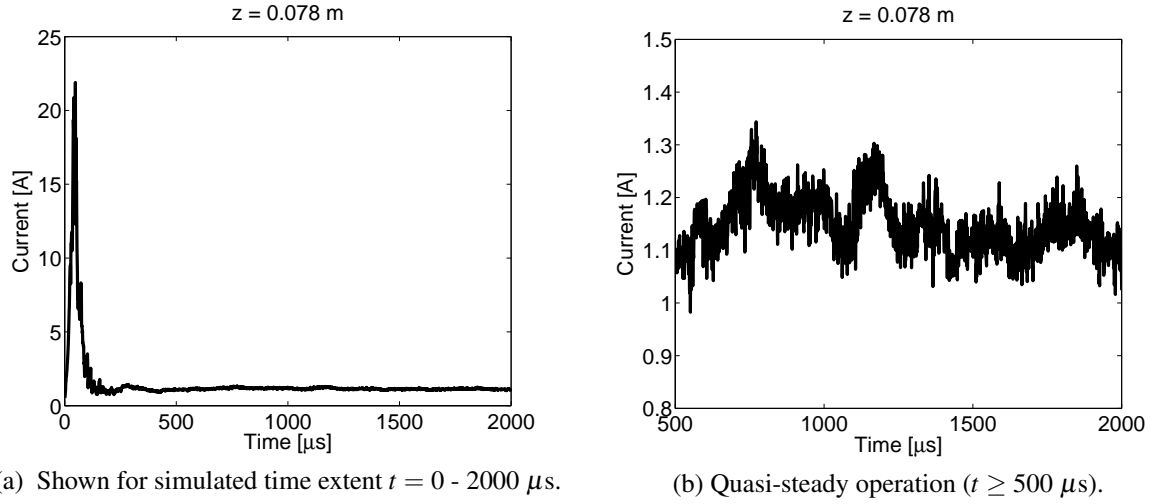


Figure 7.10: Time history of discharge current $I_D(t)$ at axial location $z = 0.078$ m (just upstream of the exit plane).

electron number density n_e . There appears to be a semi-periodic, or time repeating, structure in the quasi-steady discharge current, shown for $t > 500 \mu\text{s}$ in Fig. 7.10b; a similar periodicity can be observed in the time history of the plasma density, shown in Fig. 7.9b. The observed time period is approximately $T = 400 \mu\text{s} - 500 \mu\text{s}$, which corresponds to a linear oscillation frequency of approximately $f = 2$ kHz; we believe this oscillation may be related to the neutral depletion and replenishment cycle, i.e., the neutral injection flow and neutral depletion by ionization, and to the experimentally-observed breathing mode frequency $f = 15 - 20$ kHz (which is a consequence of the ionization process and the respective depletion and replenishment time scales for the neutral and electron/ion populations).

Figure 7.11 shows the time-averaged ion and electron current contributions to the total time-averaged discharge current, time averaged over the interval $t = 1000 \mu\text{s} - 2000 \mu\text{s}$. From the time-average profile shown in Fig. 7.11 and the time-fluctuating profiles and time histories shown in Figs. 7.10b and 7.12, we see that the discharge current fluctuates within the approximate range 1 A - 1.8 A for most of the domain; in SHT laboratory experiments at the same operating voltage, the measured discharge current was approximately 1.8 A (Meezan, 2002). The simulated discharge current is thus comparable to the experimentally-measured quasi-steady value.

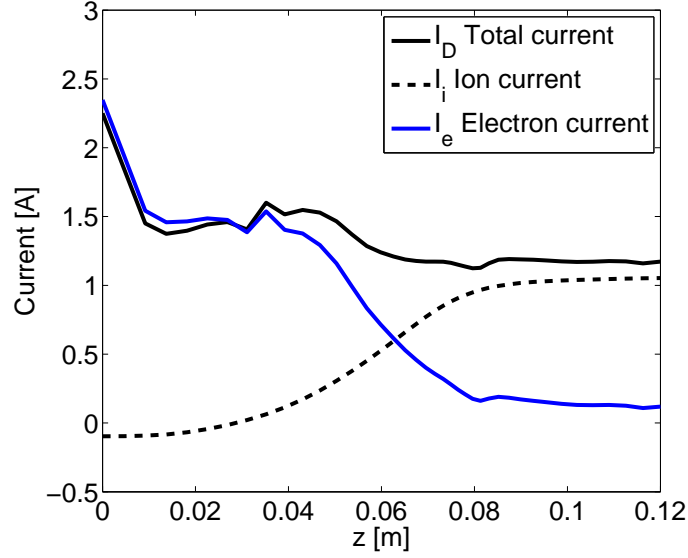
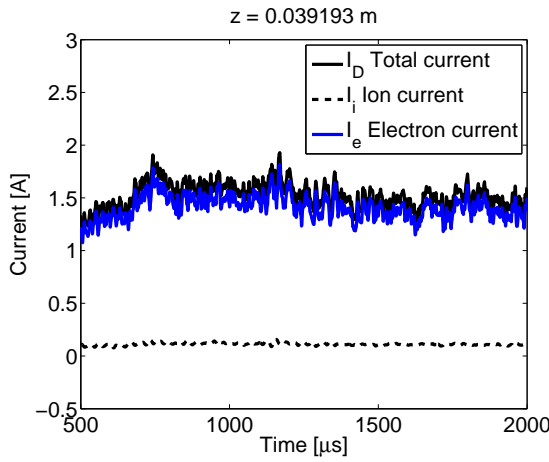
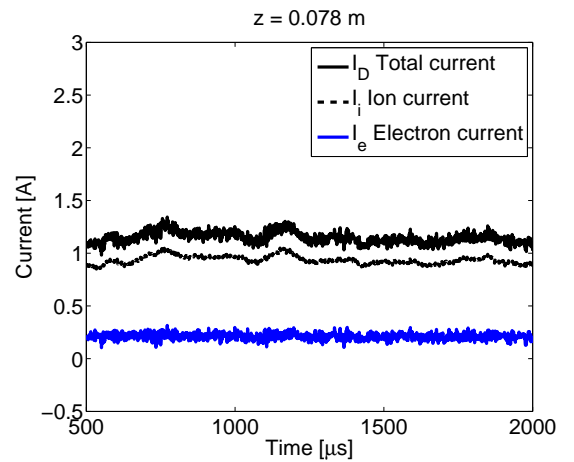


Figure 7.11: Comparison of time-averaged ion and electron current contributions to total discharge current.



(a) At axial location $z \simeq 0.04$ m (mid-channel).



(b) At axial location $z = 0.078$ m (just upstream of the exit plane).

Figure 7.12: Time history of ion and electron current contributions to total discharge current during quasi-steady operation ($t \geq 500 \mu s$).

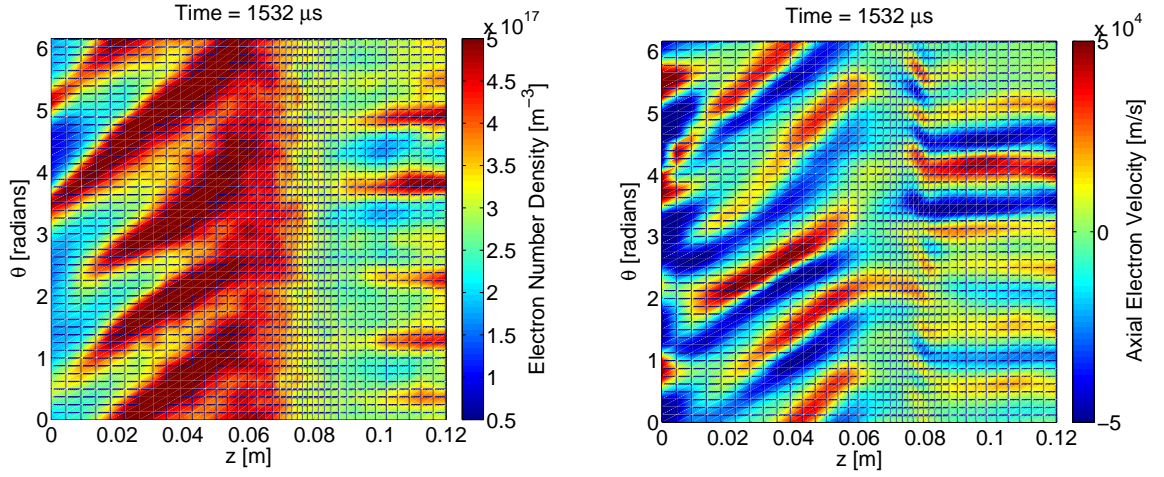
The relative contributions of the respective electron and ion currents, I_e and I_i , to the total discharge current I_D vary with z , as shown in Fig. 7.11; Fig. 7.11 provides a comparison of the relative ion and electron contributions to the total discharge current, time-averaged over the interval $t = 1000 \mu\text{s} - 2000 \mu\text{s}$. For $z \lesssim 0.06 \text{ m}$, the electron current dominates; in this region, the electron current comprises most of the discharge current and the ion current contribution is small or, in some cases (i.e., for $z \lesssim 0.02 \text{ m}$ near the anode), negative. For $z \gtrsim 0.07 \text{ m}$, the electron current contribution is extremely small and the ion current dominates; for most of this region, the electron current is an extremely small positive current. Figure 7.12 shows the time history of the current at representative z -locations within the two distinct regions in which the respective electron and ion current contributions dominate; in all cases (i.e., for all z), the ion and electron current contributions and the resulting total current fluctuate with time.

7.3.4 Electron Transport

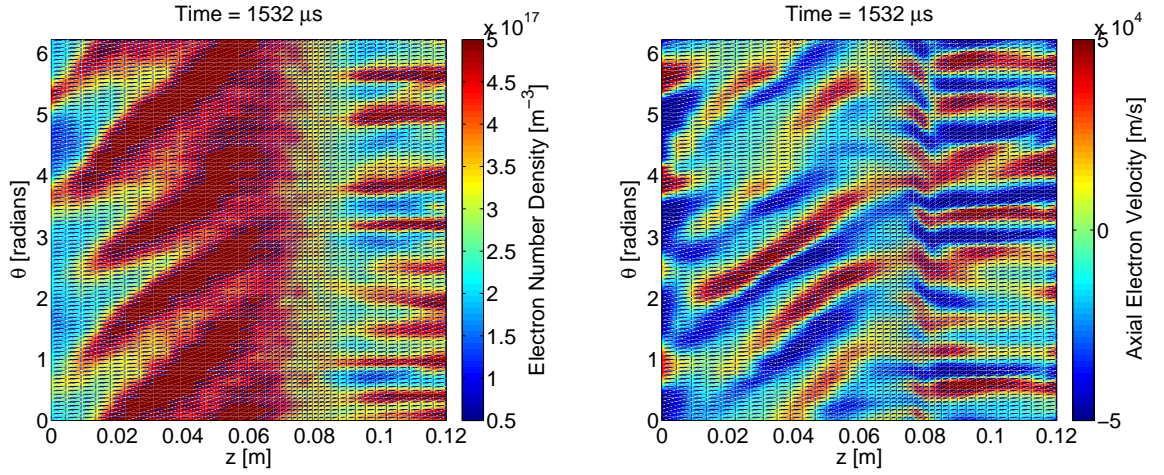
We observe wave structure similar to that described in Chap. 6; as before, fluctuations in the electron number density and axial electron velocity appear to, in some cases, enhance and, in other cases, inhibit cross-field axial electron transport. As shown in Fig. 7.13, the spatial wave structure varies distinctly with axial location; we can observe four distinct axial regions in the spatial (and corresponding temporal) wave structure, similar to and consistent with that described in Sect. 6.2.

Figure 7.14 shows the relative ion, electron, and anomalous electron contributions to the total discharge current, time-averaged over the interval $t = 1000 \mu\text{s} - 2000 \mu\text{s}$. As before, the anomalous contribution to the electron current varies significantly with axial location. In the mid-channel region ($0.02 \text{ m} \lesssim z \lesssim 0.05 \text{ m}$), the anomalous contribution comprises a significant portion of the electron current. Near the anode ($z \lesssim 0.01 \text{ m}$) and toward the channel exit plane ($z \gtrsim 0.06 \text{ m}$), however, the anomalous contribution comprises a small positive current or, in some case, a negative (i.e., opposite flowing) current contribution.

We can see the effect of the anomalous contribution more clearly from a representative time snapshot of the respective current contributions, as shown in Fig. 7.15. For 0.02 m



(a) Electron number density $n_e(z, \theta)$ for grid with 40 points in $z \times 50$ points in θ ($\Delta\theta = 2\pi/50$). (b) Axial electron velocity $u_{ez}(z, \theta)$ for grid with 40 points in $z \times 50$ points in θ ($\Delta\theta = 2\pi/50$).



(c) Electron number density $n_e(z, \theta)$ for grid with 40 points in $z \times 100$ points in θ ($\Delta\theta = 2\pi/100$). (d) Axial electron velocity $u_{ez}(z, \theta)$ for grid with 40 points in $z \times 100$ points in θ ($\Delta\theta = 2\pi/100$).

Figure 7.13: Comparison of representative time snapshots of electron number density $n_e(z, \theta)$ and axial electron velocity $u_{ez}(z, \theta)$ with azimuthal grid refinement.

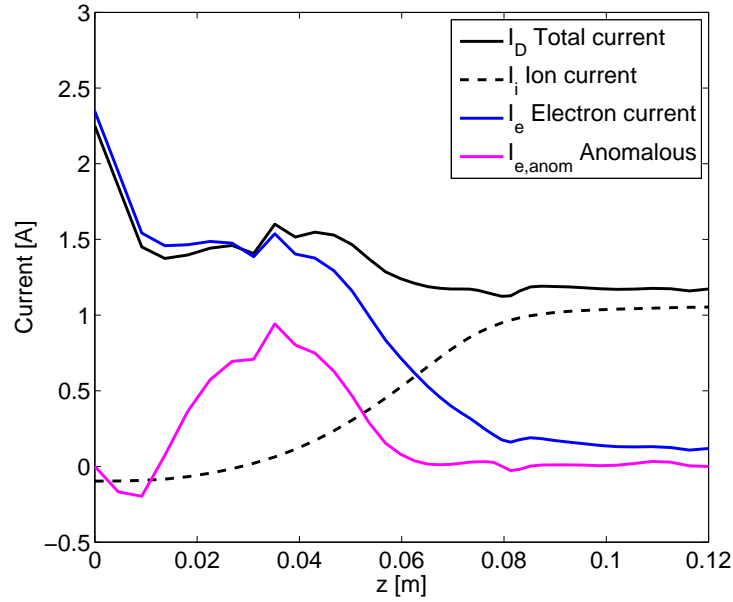


Figure 7.14: Comparison of time-averaged ion, electron, and anomalous electron current contributions to total discharge current.

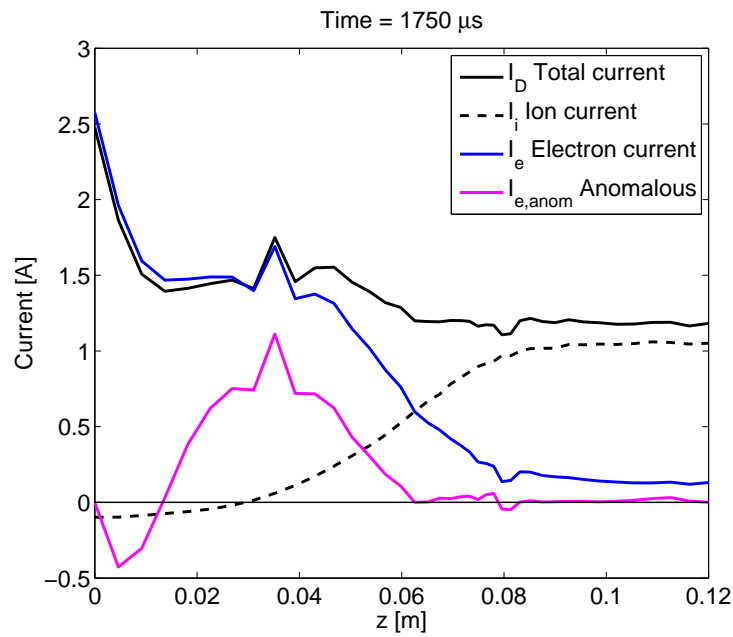


Figure 7.15: Time snapshot of ion, electron, and anomalous electron current contributions to total discharge current.

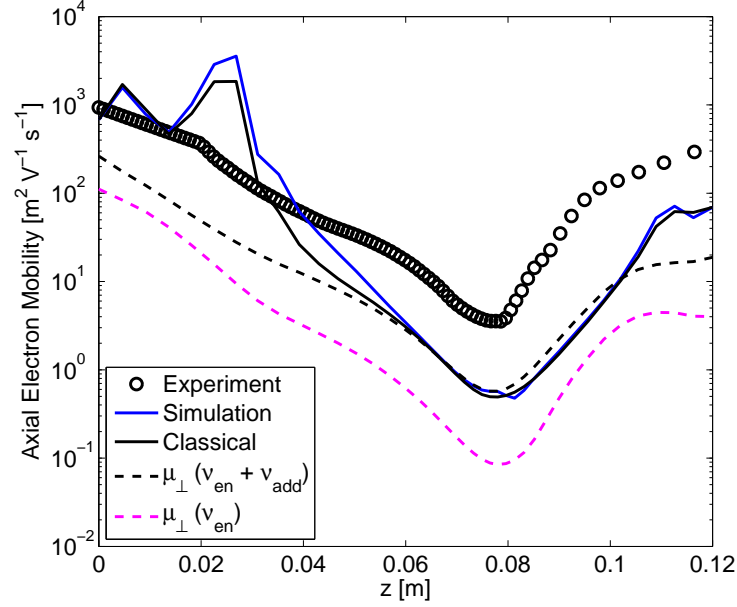


Figure 7.16: Time-averaged simulated axial electron mobility $\bar{\mu}(z)$ compared to experimentally-measured values. Simulated classical mobility terms $\bar{\mu}_{classical}$ and $\bar{\mu}_{\perp}$ are shown for reference.

$\lesssim z \lesssim 0.05$ m, the anomalous fluctuation-induced contribution comprises a significant portion of the positive electron current; the simulated waves in this region somewhat resemble the gradient-driven drift wave suggested by Frias et al. (2012), and the anomalous current serves to enhance the classical electron transport. Near the anode ($z \lesssim 0.01$ m), the simulated structure resembles a rotating spoke; near the exit plane ($z \simeq 0.08$ m), we observe simulated wave structure similar to the azimuthally counter-propagating streaming instabilities predicted by Thomas (2006). In both these regions ($z \lesssim 0.01$ m and $z \simeq 0.08$ m), the anomalous current contribution is negative; the anomalous current serves to reduce or oppose the (positive-flowing) classical electron current. Outside the channel ($z \geq 0.08$ m), the anomalous contribution is minimal; however, the total electron current in this region is likewise minimal.

Figure 7.16 provides a comparison of the time-averaged total effective simulated electron mobility $\bar{\mu}(z)$ and the classical electron mobility $\bar{\mu}_{classical}(z)$; the experimentally-measured values and the classical cross-field electron mobility term $\bar{\mu}_{\perp}$ are also shown for

reference. Note that $\mu_{\perp}(v_{en} + v_{add}) = \mu_{\perp}(v_{eff})$ refers the classical cross-field mobility μ_{\perp} based on the enhanced effective collision frequency $v_{eff} = v_{en} + v_{add}$; by contrast, $\mu_{\perp}(v_{en})$ is the classical cross-field mobility calculated using only on v_{en} , i.e., without the collision frequency enhancement. The profiles shown in Fig. 7.16 have all been time-averaged over the interval $t = 1000 \mu\text{s} - 2000 \mu\text{s}$.

In the region $0.02 \text{ m} \lesssim z \lesssim 0.05 \text{ m}$, where the anomalous contribution is significant, the anomalous fluctuation-induced transport serves to enhance electron transport; the result is a total effective electron mobility that is greater than the classical mobility. As before, the anomalous transport appears to contribute to the transport barrier, or reduced electron mobility, near the channel exit plane at $z = 0.08 \text{ m}$. It appears that the anomalous transport may also contribute to some mobility reduction near the anode ($z \lesssim 0.01 \text{ m}$) and far outside the channel ($z \gtrsim 0.115 \text{ m}$).

7.4 Summary

With the collision frequency enhancement $v_{add} = 10^7 \text{ s}^{-1}$, the simulation results generally provide a good match to experimentally-measured values. Compared to the $v_{add} = 0$ case, the agreement with the experimentally-measured property profiles is, in some cases, significantly improved; most notably, the axial location of the electron temperature peak and the ion acceleration region have both shifted downstream (relative to the $v_{add} = 0$ case), to more closely align with the corresponding experimentally-measured profiles. The magnitudes of both the simulated plasma density n_e and the simulated discharge current I_D are comparable to the experimentally-measured values, enabling analysis of realistic quasi-steady-operation similar to that observed in laboratory experiments.

The improved agreement with the experimental data is encouraging, as it indicates that the collision frequency enhancement $v_{add} = 10^7 \text{ s}^{-1}$ is of the appropriate magnitude to account for the near wall conductivity and other transport-enhancing effects not explicitly included in the model. With only a minimal change to our model implementation, we achieve significantly improved results which validate the use of our model as an effective tool for predicting quasi-steady plasma properties.

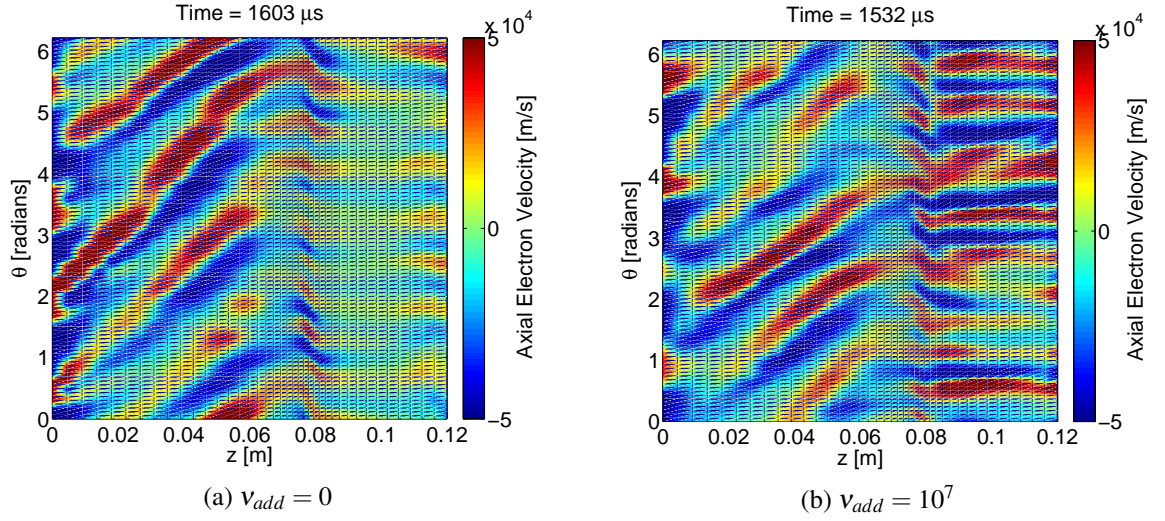


Figure 7.17: Comparison of simulated wave structure in axial electron velocity $u_{ez}(z, \theta)$, shown for grid with 40 points in $z \times 100$ points in θ .

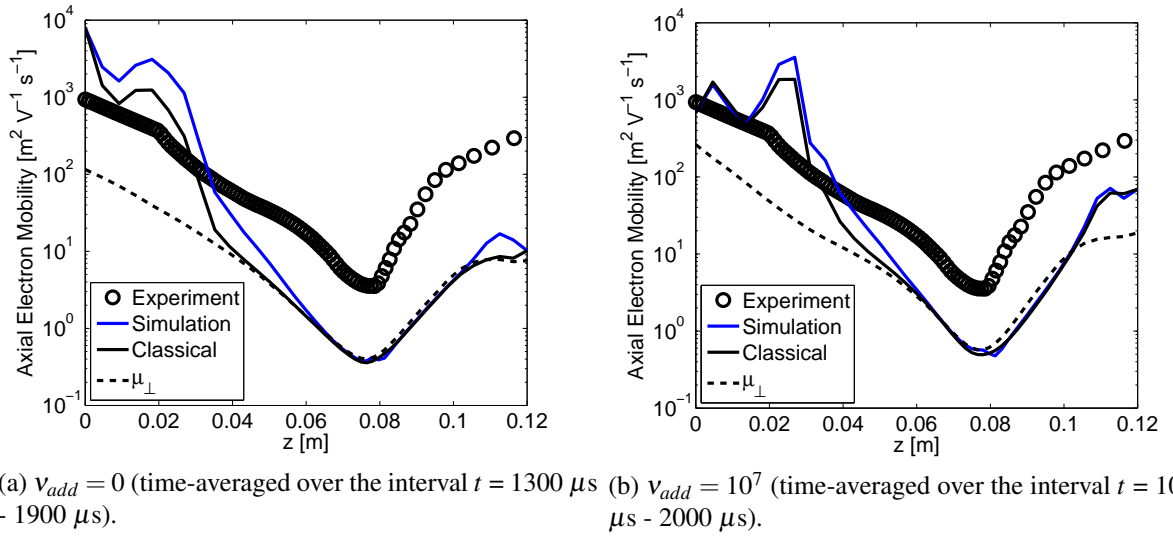


Figure 7.18: Comparison of time-averaged simulated axial electron mobility $\bar{\mu}(z)$. Experimentally-measured values and simulated classical mobility terms $\bar{\mu}_{classical}$ and $\bar{\mu}_{\perp}$ are shown for reference.

As before, our primary objective is to characterize the role of fluctuations and quantify their impact on the electron transport process. As shown in Fig. 7.17, we observe similar dispersive wave structure in both the $v_{add} = 0$ and $v_{add} = 10^7 \text{ s}^{-1}$ simulations. For the most part, the wave characteristics (i.e., wave number, frequency, and propagation direction) and the axial variation of the wave structure are similar; however, in the $v_{add} = 10^7 \text{ s}^{-1}$ case, the mid-channel waves appear to be shifted slightly downstream, extending through $z \simeq 0.07 \text{ m}$. In both cases, as shown in Fig. 7.18, the fluctuation-induced anomalous transport serves to enhance electron transport in the mid-channel region and reduce transport, leading to a distinct transport barrier, near the exit plane ($z = 0.08 \text{ m}$). In the $v_{add} = 10^7 \text{ s}^{-1}$ case, the effective total electron mobility that results from the collision frequency enhancement and the fluctuation-induced anomalous transport appears to largely account for, i.e., roughly match, the experimentally-observed mobility; however, due to the increased classical mobility that results from the enhanced collision frequency, the significance of the fluctuation-driven anomalous transport (relative the classical contribution and the total effective mobility) is diminished, compared to the $v_{add} = 0$ case. While the collision frequency enhancement improves the model's viability as a general-purpose tool for predicting plasma properties, the effect of the enhanced collision frequency somewhat obscures the role and quantitative impact of the fluctuations; overall, this seems a reasonable trade to make for improved predictive model performance.

Chapter 8

Conclusion

8.1 Research Summary

We use the described 2D axial-azimuthal (z - θ) hybrid fluid-PIC simulation as a tool to investigate the role of fluctuations in generating cross-field electron transport in a simulated Hall thruster discharge. The simulated results are compared to experimental measurements of a similar laboratory discharge (the Stanford Hall Thruster); with the inclusion of an enhanced collision frequency, the simulated results show improved agreement with the experimental measurements.

It appears that azimuthal fluctuations do indeed impact cross-field axial electron transport. The fluctuation-induced anomalous transport contributes to axial electron mobility enhancement in some regions, primarily in the thruster mid-channel region; near the exit plane, the anomalous transport contributes to a marked electron transport barrier, consistent with that observed in laboratory experiments.

The time and spatial resolution of our simulations limit the spatial and temporal characteristics of the observable simulated phenomena. For the time resolution and simulated time extent presented here, the observable frequency range is approximately 1 kHz to 10 MHz. Based on the non-uniform axial grid spacing, the minimum observable axial wavelength range is $\lambda_{z,min} \simeq 3$ mm - 9 mm; in the azimuthal direction, the minimal observable wavelength is $\lambda_{\theta,min} \simeq 5$ mm (for the azimuthally-refined grid with 100 points uniformly spaced in θ). The observed simulated fluctuations fall well within these frequency and wavelength

limits, with maximum observed frequencies up to approximately 200 kHz and minimum axial and azimuthal wavelengths $\lambda_z \simeq 3$ cm and $\lambda_\theta \simeq 1.5$ cm ($m_\theta \simeq 16$), respectively.

Overall, the simulated fluctuation-induced transport appears to account for some mobility enhancement; however, the simulated anomalous transport does not fully account for all of the experimentally-measured super-classical electron mobility. Additional simulations with a constant collision frequency enhancement $\nu_{add} = 10^7 \text{ s}^{-1}$ indicate that an additional transport mechanism is needed to generate a simulated mobility profile of comparable magnitude to that measured experimentally; the required level of collision frequency enhancement is consistent with that due to wall scattering, or the so-called near wall conductivity. It is also possible that higher-frequency, shorter-wavelength fluctuations, which we do not simulate here, are responsible for additional mobility enhancement.

8.2 Suggestions for Future Work

We propose two future endeavors to address the discrepancy between the anomalous electron transport simulated here and the experimentally-measured effective electron mobility.

Additional z - θ simulations, using this same hybrid model, with finer grid spacing and shorter time step would enable the investigation of higher-frequency and shorter-wavelength fluctuations which may contribute to additional transport enhancement. Such simulations could be significantly computationally expensive and would perhaps require further modification to the numerical solution approach; however, they could provide further insight into fluctuation-induced anomalous transport processes and improved predictions of the effective electron mobility.

It is clear that the inclusion of wall effects, i.e., wall conductivity, may be critical to accurately predicting the the cross-field axial electron mobility. We suggest either an augmented z - θ model with an improved model for plasma interactions with the wall or, alternatively, a 2D r - z model with an anomalous transport model (e.g., based on a z - θ model similar to that presented here). A 3D r - z - θ (or x - y - z) model would address both the radial dynamics, i.e., wall interactions, and the azimuthal fluctuation-induced transport; if the computational expense can be made sufficiently tractable to enable simulations with both a small time step (to capture high frequency oscillations) and a long simulated time extent (to

address slowly-evolving phenomena, e.g, the thruster breathing mode), this may be the best approach. Recent advances in efficient numerical solution methods and increased computational capability, based on modern parallelized computing architectures, can reduce the computational expense associated with 3D simulations. For improved simulation of the near plume region outside the thruster channel where turbulence at small spatial scales may affect electron transport, we suggest a modified treatment outside the channel to more accurately model the plume expansion and cathode electron flow.

Appendix A

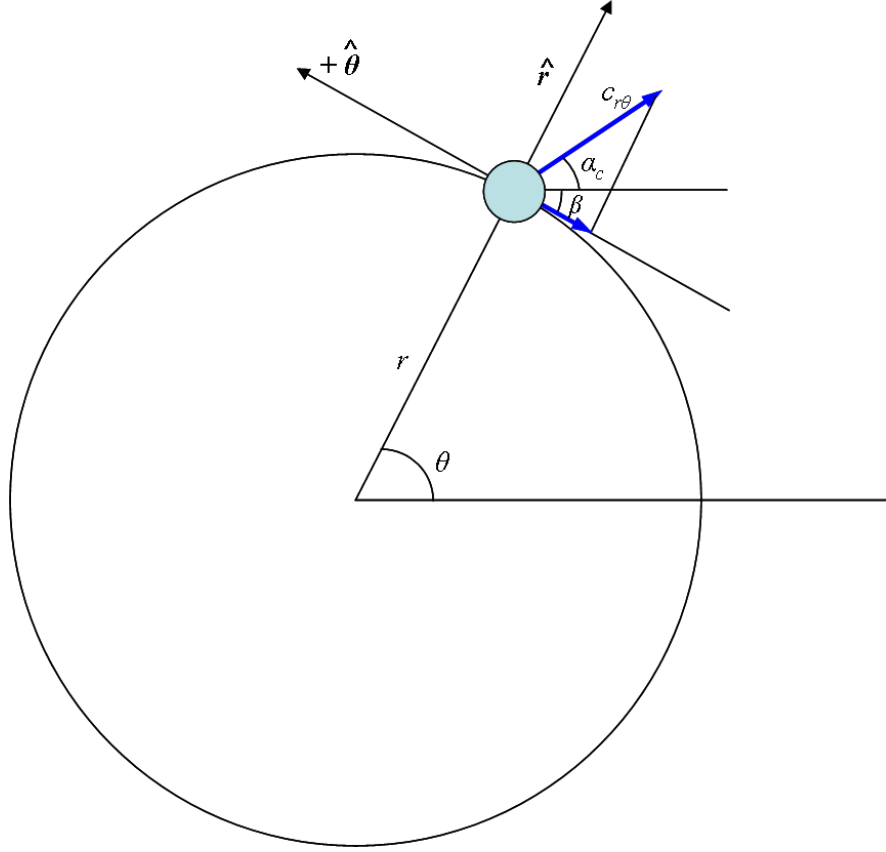
Particle Velocity Distribution Sampling

A.1 Implementation

In order to initialize the ion and neutral particle velocities, either for the simulation initial conditions or neutral injection at the anode, we sample the particle velocities from specified velocity distributions. In this appendix, we describe the particle velocity sampling implementation.

A.1.1 Distribution Inversion (Sampling)

We use the distribution inversion, or sampling, method described by Scharfe (2009) and Birdsall and Langdon (2005). The process involves using a uniformly-distributed random variable, generated by a pseudo-random number generator algorithm, to sample the appropriate distribution function. Often, the sampling process, i.e., the pseudo-random number generation and associated sampling of the velocity distribution is performed on-the-fly as part of the simulation calculation; however, in our case, we perform the velocity distribution sampling a priori and store the sampled values in a simulation input file. The sampled values are then read in from the file, as needed, during the simulation. We perform this a priori distribution sampling for the various velocity distributions described below.

Figure A.1: Velocity projection in r - θ plane.

A.1.2 Projection onto z - θ Plane

The z -velocities are sampled directly from the appropriate axial velocity distribution, e.g., $f_{Maxwellian}(v_z)$. For the θ -velocity sampling, however, the process is more complicated.

To determine a particle's θ -velocity, we sample its speed $c_{r\theta}$ in the r - θ plane. The particle is also given a random velocity direction within the r - θ plane, determined by the velocity orientation angle α_c . The speed $c_{r\theta}$ is sampled from the appropriate 2D Maxwellian speed distribution (which accounts for the cylindrical z - r - θ , or circular r - θ , coordinate system), specified for the various species in Sect. A.2. The orientation α_c of the velocity vector is sampled from a uniform distribution over the interval 0 to 2π radians.

A particle's initial θ -velocity can be positive or negative; it is determined by projecting the particle's sampled speed $c_{r\theta}$ in the r - θ plane onto the $\hat{\theta}$ -direction, accounting for the

particle's θ -position, as shown in Fig. A.1. The vector $\vec{c}_{r\theta}$ has a magnitude determined by the sampled value $c_{r\theta}$ and the orientation angle α_c , defined as shown in Fig. A.1. Accounting for the azimuthal position θ , we can project the velocity vector $\vec{c}_{r\theta}$ onto the particle's $\hat{\theta}$ -direction to determine its θ -velocity:

$$v_\theta = \vec{c}_{r\theta} \cdot \hat{\theta} \quad (\text{A.1})$$

$$\begin{aligned} &= -c_{r\theta} \cos(\beta + \alpha_c) \\ &= -c_{r\theta} \cos\left(\frac{\pi}{2} - \theta + \alpha_c\right) \\ &= c_{r\theta} \sin \alpha_c \cos \theta - c_{r\theta} \cos \alpha_c \sin \theta \end{aligned} \quad (\text{A.2})$$

A.2 Velocity Distributions

A.2.1 Initial Conditions

For the simulation initial conditions, the ion and neutral velocities are sampled from the distinct velocity distributions shown in Figs. A.2 and A.3, respectively. In each case, the z -velocities are sampled from a Maxwellian velocity distribution at the specified temperature, and the speed values $c_{r\theta}$ are sampled from a Maxwellian speed distribution. The orientation angle α_c is sampled from a uniform distribution over the interval 0 to 2π radians.

Figures A.2 and A.3 are histograms of the sampled velocity values contained in the respective simulation input files. For the ions, both the velocity distribution for v_{iz} and the speed distribution for $c_{r\theta}$, shown in Figs. A.2a and A.2b, respectively, are based on an initial equilibrium temperature $T_i = 650$ K. For the neutrals, we sample a distribution identical to that used for the ions for the speed $c_{r\theta}$; however, for the axial neutral velocity v_{nz} , we use a Maxwellian distribution, shown in Fig. A.3a, based on an extremely low initial temperature $T_n < 1$ K. Using a low velocity (low temperature) distribution for the neutral initialization ensures that a sufficient population of neutrals will remain within the computational domain to provide a background (population source) for ionization, as required to sustain the simulated discharge.

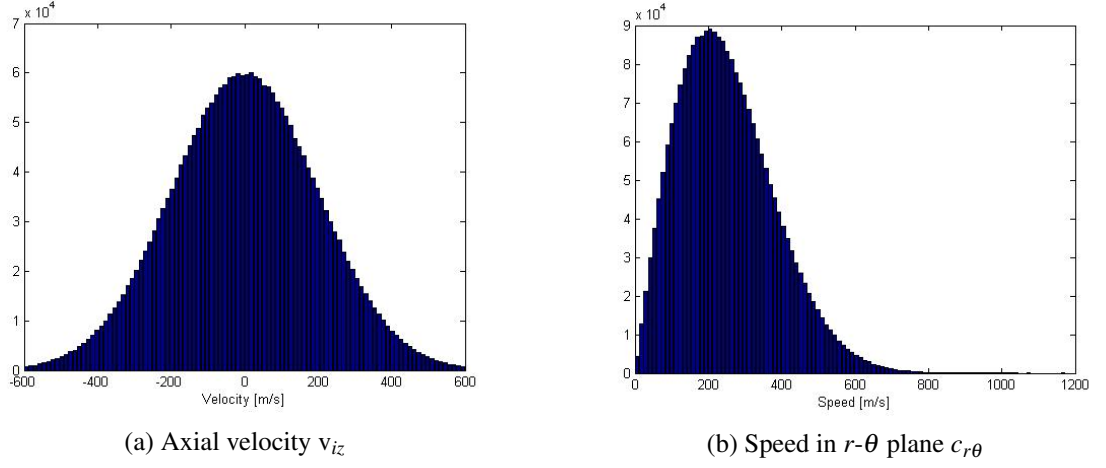


Figure A.2: Sampled velocity distributions for ion particle initial conditions.

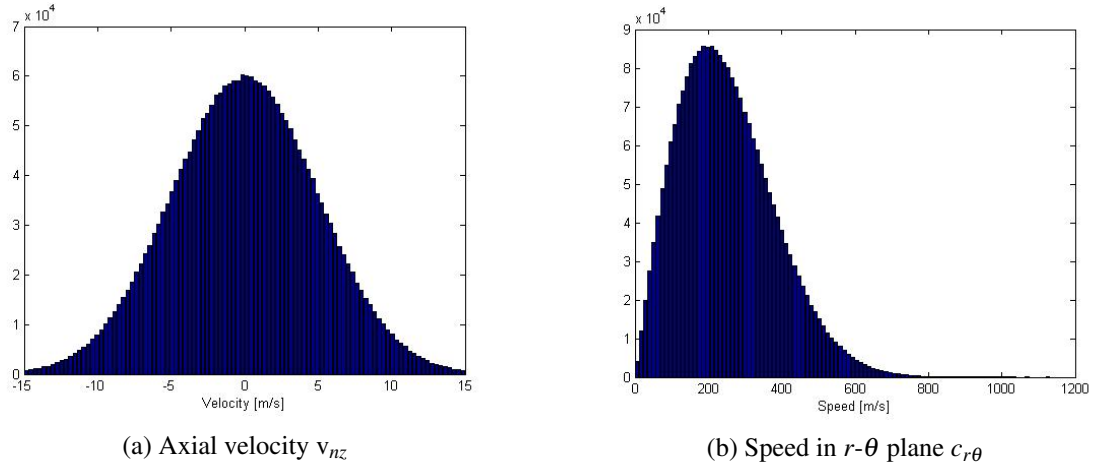


Figure A.3: Sampled velocity distributions for neutral particle initial conditions.

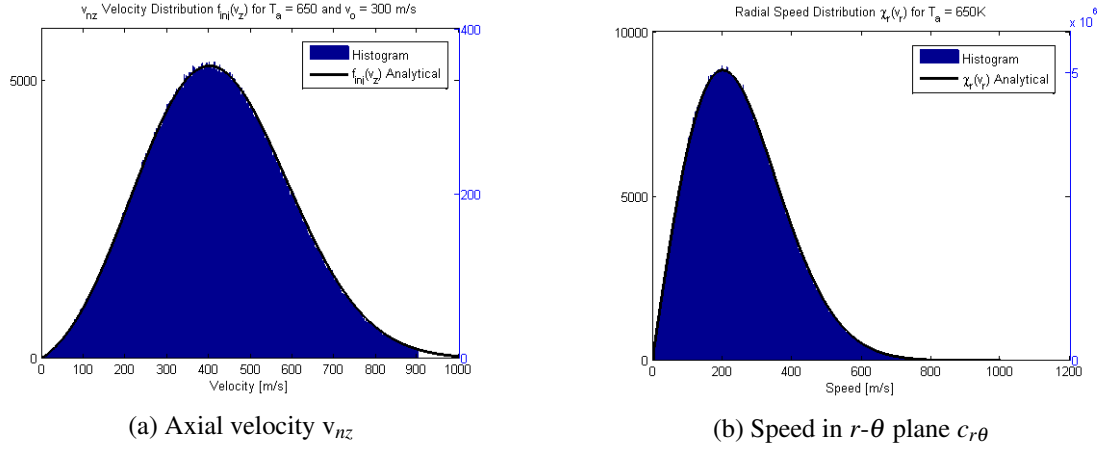


Figure A.4: Sampled velocity distribution functions for injected neutral particles.

A.2.2 Neutral Injection

Injected neutral particles are introduced into the computational domain at the anode plane. The injected particles can assume either positive or negative values of $v_{n\theta}$; however, their initial axial velocities v_{nz} must be positive. The z -velocities v_{nz} are sampled from a one-way Maxwellian flux distribution, shown in Fig. A.4a, based on an anode temperature $T_{anode} = 650\text{K}$ with a mean (bulk) neutral injection velocity $v_0 = 300\text{ m/s}$. The particle speed values $c_{r\theta}$, used to determine $v_{n\theta}$, are sampled from a Maxwellian speed distribution at the same temperature $T_{anode} = 650\text{K}$; the peak value of this speed distribution, shown in Fig. A.4b, occurs at the most probably speed $c_{r\theta} \simeq 200\text{ m/s}$. While these parameters for the velocity distribution were not directly experimentally measured, the discharge does not appear to be particularly sensitive to the anode temperature T_{anode} which governs the distribution.

Appendix B

Analysis of Dispersive Wave Behavior

In Chap. 6, we describe spatially and temporally-varying fluctuations in the plasma properties. In this appendix, we further describe the analysis process used to mine the simulated wave data and discuss comparisons to linearized fluid theory models for dispersive wave propagation.

As in Chap. 6, we consider fluctuations in the electron density, axial electron velocity, and electric potential of the form

$$\tilde{n}_e(z, \theta, t) = n_o \cos(k_z z + k_\theta \theta - \omega t) \quad (\text{B.1a})$$

$$\tilde{u}_{ez}(z, \theta, t) = u_o \cos(k_z z + k_\theta \theta - \omega t + \psi) \quad (\text{B.1b})$$

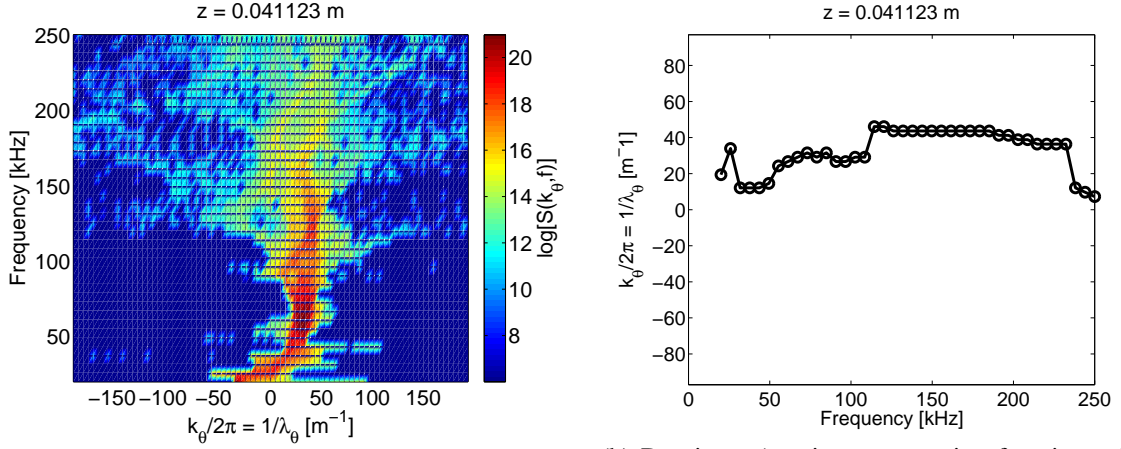
$$\tilde{\phi}(z, \theta, t) = \phi_o \cos(k_z z + k_\theta \theta - \omega t + \xi) \quad (\text{B.1c})$$

where each wave propagation mode is characterized by its axial and azimuthal wavenumbers $k_z = 2\pi/\lambda_z$ and $k_\theta = 2\pi/\lambda_\theta$, respectively, and temporal frequency $f = \omega/2\pi$. We are interested in the dispersion relation $\omega(k_z, k_\theta)$ between the propagation frequencies and wavenumbers. Note that multiple propagation modes, i.e., multiple frequency and wavenumber combinations, can exist simultaneously; in fact, we expect, and the linearized theory predicts, that multiple propagation modes will exist, each with distinct wave characteristics (frequency and wavenumber) and a corresponding unstable growth or decay rate.

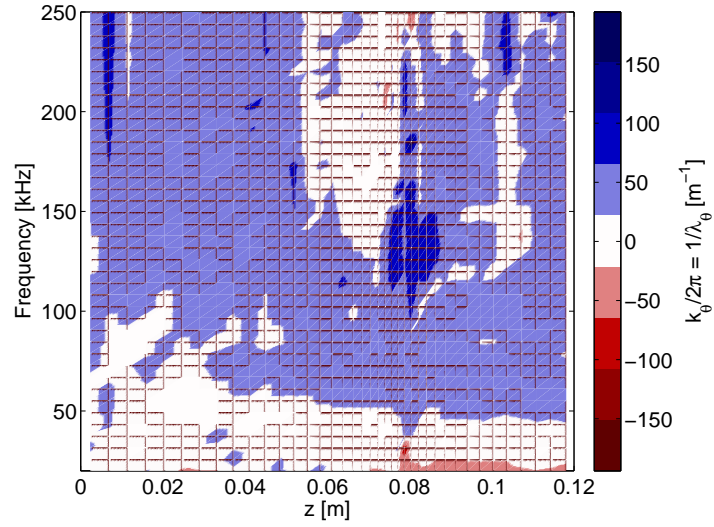
B.1 Analysis of Simulated Data

In order to characterize the wavenumber and frequency content of the simulated data, we use a Morlet wavelet decomposition analysis described in detail by Thomas (2006) and Scharfe (2009), based on the approach described by Beall et al. (1982). We consider the time history of a particular plasma property at pairs of probes, separated in either z or θ ; based on the wavelet decomposition analysis, we can obtain a scattering function $S(k, f)$, similar to a power spectral density, which indicates the strength (or power) associated with correlated frequencies f and wavenumbers k along the propagation direction between the two probes. The range of resolvable frequencies and wavenumbers is determined by the time sampling resolution of the time history at each probe and the probe separation distance. In the case of simulated data, we consider the plasma property data at the computational grid points. The limiting probe separation distance, and corresponding wavenumber range, is thus determined by the spatial resolution of the computation grid; likewise, the frequency range is determined by the time resolution of the simulated data, or the outer loop simulation time step. Fig. B.1a is an example of the scattering function $S(k_\theta, f)$ for two grid points, or probe locations, azimuthally separated by $\Delta\theta = 2\pi/50$, at the axial location $z \simeq 0.04$ m.

We perform this analysis across the axial extent the computational domain, considering simulated data at a pair of axially-adjacent grid points and a pair of azimuthally-adjacent grid point for each axial location z . In order to develop the dispersion map shown for k_θ in Fig. B.1c (and the corresponding dispersion map for k_z), we consider the scattering functions $S(k_z, f)$ and $S(k_\theta, f)$ for all axial locations z . At each axial location z , we identify the dominant wavenumbers k_z and k_θ at each frequency f . For a given frequency, we find the wavenumber k associated with the maximum scattering function value; by doing so for each frequency f at a given axial location z we can find the dominant dispersion relation $f(k/2\pi)$, or $\omega(k)$, shown in Fig. B.1b for the azimuthal wavenumber (based on a pair of azimuthally-adjacent probe points) at axial location $z \simeq 0.04$ m. We perform this analysis, identifying the dominant wavenumbers $k_z(f)$ and $k_\theta(f)$ at each frequency, for each axial location z ; we can then aggregate this data (e.g., Fig. B.1b) to create the



(a) Scattering function $S(k_\theta, f)$ for azimuthal probe (grid point) pair with separation $r_{mid}\Delta\theta \simeq 5.1$ mm at $z \simeq 0.04$ m
 (b) Dominant (maximum scattering function value) azimuthal wavenumbers $k_\theta(f)$ at $z \simeq 0.04$ m (obtained from a)



(c) Dispersion map for $k_\theta(f)$ assembled for all z

Figure B.1: Dispersion map (c) is assembled from individual probe pair analyses (shown in a and b) at axial locations z .

dispersion map shown in Fig. B.1c, which illustrates the axial variation in the simulated dominant dispersive wavenumber $k_\theta(f)$.

We are interested in characterizing dispersive wave fluctuations in the electron number density n_e , axial electron velocity u_{ez} , and electric potential ϕ . As described in Chap. 6, we find that the wave characteristics vary with axial location.

B.2 Comparison to Linearized Fluid Theory

We attempt to relate the simulated fluctuations and the resulting fluctuation-induced anomalous electron current to wave propagation modes described by linearized fluid theory models. Specifically, we consider the mid-channel region ($0.02 \text{ m} \lesssim z \lesssim 0.06 \text{ m}$) waves and resulting electron mobility enhancement in the context of gradient-driven drift waves described by Kapulkin and Guelman (2008) and Frias et al. (2012). For the waves observed near the exit plane ($0.07 \text{ m} \leq z \leq 0.08 \text{ m}$), we seek qualitative comparisons to the dispersion relations and fluctuation-induced transport described by Thomas (2006). Here, we describe the dispersive wave characteristics and resulting fluctuation-induced electron current predicted by the respective linearized fluid theory models for the relevant discharge conditions.

B.2.1 Linearized Model Approach

The various linearized fluid theory models are based on the same general approach. In each case, we begin by considering the relevant fluid equations for the electron (and, as relevant, other plasma) species. Each fluctuating quantity can be written in terms of a constant steady-state component and a small-amplitude fluctuation or perturbation, e.g., in the case of the electron number density,

$$n_e(z, \theta, t) = n_{SS}(z, \theta) + \tilde{n}_e(z, \theta, t) \quad (\text{B.2})$$

where the fluctuating component $\tilde{n}_e(z, \theta, t)$ is of the form shown in Eqn. B.1a. We can represent the small-amplitude fluctuation in terms of the exponential function:

$$\begin{aligned}
\tilde{n}_e(z, \theta, t) &= n_o \cos(k_z z + k_\theta \theta - \omega t) \\
&= n_o \operatorname{Re} \{ \exp [i(k_z z + k_\theta \theta - \omega t)] \}
\end{aligned} \tag{B.3}$$

We can represent each fluctuating quantity, e.g., ϕ , u_{ez} , $u_{e\theta}$, E_z , in a similar manner; we then introduce the fluctuating quantities into the appropriate fluid equations. Next, we linearize the resulting fluid equations about the steady state solution, neglecting any higher-order derivatives and small amplitude quantities (i.e., the products of any fluctuation amplitudes, e.g., $n_o \phi_o$). Once the equations have been linearized, we can typically solve for a dispersion relation $\omega(k_z, k_\theta)$. Often, the dispersion relation will give complex values of $\omega(k_z, k_\theta)$, which can be written in the form

$$\omega = \omega_R + i\omega_I \tag{B.4}$$

In such cases, the real component ω_R determines the propagation frequency, and we can find the associated growth or decay rate for that frequency mode ω_R by considering the corresponding imaginary component ω_I .

$$\begin{aligned}
\tilde{n}_e(z, \theta, t) &= n_o \operatorname{Re} \{ \exp [i(k_z z + k_\theta \theta - \omega t)] \} \\
&= n_o \operatorname{Re} \{ \exp [i(k_z z + k_\theta \theta - \omega_R t) + \omega_I t] \}
\end{aligned} \tag{B.5}$$

$$= n_o \cos(k_z z + k_\theta \theta - \omega t) \exp(\omega_I t) \tag{B.6}$$

From Eqn. B.6, we see that the sign of ω_I determines whether the frequency mode grows or decays. For $\omega_I > 0$, the instability will grow; for $\omega_I < 0$, the instability will decay. From the linearized equations, we can also calculate the fluctuation-induced current

$$I_{ez,anom} = A_{sect} e \langle \tilde{n}_e \tilde{u}_{ez} \rangle \tag{B.7}$$

associated with propagation mode $\omega(k_z, k_\theta)$.

The linearized fluid theory models discussed below are based on the same general linearized small-amplitude fluctuation (i.e., perturbation analysis) approach described here.

However, in each case, varying assumptions and approximations in the derivation of the fluid equations and the linearization process result in distinct dispersion relations, with corresponding growth/decay rates and associated fluctuation-induced current predictions.

B.2.2 Frias Model ($0.02 \text{ m} \leq z \leq 0.06 \text{ m}$)

We consider the gradient-driven waves described by Frias et al. (2012). In the Frias model, which is an extension of the model originally described by Kapulkin and Guelman (2008), axial gradients in the magnetic field strength and the electron number density can drive unstable oscillations in the plasma properties which generate electron current. The predicted dispersion relation $\omega(k_z, k_\theta)$ is particularly sensitive to the relationship between the respective gradients, or gradient length scales, of the axially-varying magnetic field strength and the electron density.

For the mid-channel region ($0.02 \text{ m} \leq z \leq 0.06 \text{ m}$), we compare the simulated wave characteristics to those predicted by the Frias model. Table B.1 lists the plasma properties required by the Frias model; we report the approximate nominal values for a representative axial location $z = 0.04 \text{ m}$ within the mid-channel region $0.02 \text{ m} \leq z \leq 0.06 \text{ m}$. Table B.2 describes the resulting dispersive wave modes predicated by the Frias model for the range of inverse azimuthal wavelengths (or azimuthal wavenumbers) $-50 \text{ m}^{-1} \leq k_\theta/2\pi \leq 50 \text{ m}^{-1}$. The wavenumbers predicted by the Frias model are consistent with those observed in the simulated data for this mid-channel region. According to the Frias model, both modes result in positive current of extremely small magnitude. Furthermore, due to the small magnitudes of their growth rates, it is unclear whether these modes can grow or persist over any significant length or time scale. As such, it is unclear whether these gradient-driven waves are significant contributors to the electron transport enhancement in this region.

B.2.3 Thomas Model ($0.07 \text{ m} \leq z \leq 0.08 \text{ m}$)

For the region just upstream of the channel exit plane ($0.07 \text{ m} \leq z \leq 0.08 \text{ m}$), we consider the linearized fluid theory model for a streaming (two stream) instability described by Thomas (2006). Thomas' model includes the effect of the axial shear $s = \partial u_{e\theta}/\partial z$; based on the simulated data, we believe that the strong axial shear in this region may impact axial

Table B.1: Summary of relevant plasma property values at $z \simeq 0.04$ m

Property	Nominal Value	Description
$\lambda_z^{-1} = k_z/2\pi$	-30 m^{-1}	Inverse axial wavelength
B_r	0.002 T	Magnetic field strength
T_e	3.5 eV	Electron temperature
n_e	$3 \times 10^{16} \text{ m}^{-3}$	Electron number density
u_{iz}	-500 m/s	Axial ion velocity
E_z	-100 V/m	Axial electric field
l_B	0.029 m	Length scale for axial gradient of magnetic field, defined by
$l_B^{-1} = \frac{1}{B} \frac{\partial B}{\partial z}$		
l_N	-0.015 m	Length scale for axial gradient of electron density, defined by
$l_N^{-1} = \frac{1}{n_e} \frac{\partial n_e}{\partial z}$		

Table B.2: Summary of dispersive wave modes predicted by Frias model for $-50 \text{ m}^{-1} \leq k_\theta/2\pi \leq 50 \text{ m}^{-1}$

Root	Approximate Frequency Range	Growth or Decay	Current Contribution
1	50 kHz to 320 kHz	Indeterminate	Positive
2	-160 kHz to -450 kHz	Indeterminate	Positive

Table B.3: Summary of relevant plasma property values at $z \simeq 0.078$ m

Property	Nominal Value	Description
$\lambda_z^{-1} = k_z/2\pi$	15 m^{-1}	Inverse axial wavelength
B_r	0.0105 T	Magnetic field strength
T_e	5 eV	Electron temperature
n_e	$3 \times 10^{16} \text{ m}^{-3}$	Electron number density
u_{iz}	6500 m/s	Axial ion velocity
$u_{i\theta}$	100 m/s	Azimuthal ion velocity
$\partial u_{iz}/\partial z$	$2 \times 10^5 \text{ s}^{-1}$	Axial gradient of axial ion velocity
$\partial u_{i\theta}/\partial \theta$	0	Neglect azimuthal variation in azimuthal ion velocity
u_{ez}	-50,000 m/s	Axial electron velocity
$u_{e\theta}$	100,000 m/s	Azimuthal electron velocity
$\partial u_{ez}/\partial z$	-10^7 s^{-1}	Axial gradient of axial electron velocity
$\partial u_{e\theta}/\partial \theta$	0	Neglect azimuthal variation in azimuthal electron velocity
$s = \partial u_{e\theta}/\partial z$	$2 \times 10^7 \text{ s}^{-1}$	Axial shear (axial gradient of azimuthal electron velocity)

Table B.4: Summary of dispersive wave modes predicted by Thomas model for $-50 \text{ m}^{-1} \leq k_\theta/2\pi \leq 50 \text{ m}^{-1}$

Root	Approximate Frequency Range	Growth or Decay	Current Contribution
1	100 kHz to 800 kHz	Growth	Positive/Negative
2	-500 kHz to -800 kHz	Decay	Positive
3	1 MHz to 6 MHz	Growth/Decay	Positive/Negative
4	1 GHz to 2 GHz	Growth	Negative
5	-1 GHz to -2 GHz	Growth	Positive

electron transport. Table B.3 lists the plasma properties required by the Thomas model, with nominal values reported for the axial location $z = 0.78$ m just upstream of the channel exit plane.

Table B.4 describes the resulting dispersive wave modes predicted by the Thomas model for the range of inverse azimuthal wavelengths (or azimuthal wavenumbers) $-50 \text{ m}^{-1} \leq k_\theta/2\pi \leq 50 \text{ m}^{-1}$; the numbers [1-5] in the leftmost column refer to the five distinct roots of the dispersion relation $\omega(k_z, k_\theta)$. For all 5 roots, the magnitude of the current contribution is extremely small for negative k_θ ($k_\theta < 0$), but there is significant predicted current for positive k_θ ($k_\theta > 0$).

For certain azimuthal wavenumbers k_θ , roots 1 and 2 assume similar frequency values (~ 100 kHz - 800 kHz) of opposite sign, indicating a pair of azimuthally counter-propagating modes. The negative frequency root [2] decays while the positive frequency root [1] has a positive growth rate; the negative frequency root [2] results in a positive electron current, while the negative frequency root [1] generates positive current for $5 \text{ m}^{-1} \lesssim k_\theta/2\pi \lesssim 25 \text{ m}^{-1}$ and negative current otherwise.

Likewise, roots 4 and 5 comprise a second pair of azimuthally counter-propagating modes at $f \simeq 1.5$ GHz. In this case, both counter propagating modes have a positive growth rate; however, one results in a positive current contribution while the other generates negative current. The predicted frequencies are beyond the time step resolution of our simulated data. Simulations at finer time step would enable comparison to these predicted high frequency modes.

Root 3 represents a single (unpaired) propagation mode at $f \simeq 1$ MHz - 6 MHz. For $5 \text{ m}^{-1} \lesssim k_\theta/2\pi \lesssim 25 \text{ m}^{-1}$, this is a decaying mode which generates positive current. For all other computed values of k_θ , this mode has a positive growth rate and generates negative current.

We can estimate the impact of the axial shear by considering the resulting predicted modes for various shear values. We compare the nominal $s = 2 \times 10^7 \text{ s}^{-1}$ to a case with $s = 0$. For the $s = 0$ case, the predicted modes $\omega(k_z, k_\theta)$ are similar; however, the relative growth rates of the respective modes change. The nominal $s = 2 \times 10^7 \text{ s}^{-1}$ case and the $s = 0$ case predict different maximal growth rate modes. For the plasma conditions simulated here, the shear magnitude clearly affects the relative growth rates of the various modes and

can determine which propagation mode will dominate, or grow most quickly; this, in turn, can determine whether the associated fluctuation-induced electron current serves to enhance or reduce the effective bulk axial electron mobility.

B.3 Summary

We consider the Frias and Thomas linearized fluid models for the respective discharge conditions inside the thruster channel. The wavenumbers and frequencies predicted by the Frias and Thomas models for the mid-channel ($0.02 \text{ m} \leq z \leq 0.06 \text{ m}$) and near exit plane ($0.07 \text{ m} \leq z \leq 0.08 \text{ m}$) regions, respectively, appear to be consistent with those observed in the simulated data. However, there is not a clear correspondence between the effective electron mobility variation in the simulated data and the growth rates and electron current contributions predicted by the linearized models.

It is possible that complicated non-linear interactions contribute to the growth of certain unstable modes and their corresponding current contributions; the linearized models cannot be expected to capture such phenomena which may affect instability growth or contribute to the electron transport. Other mechanisms may also be responsible for the fluctuations and resulting electron transport observed in the simulated data; corresponding investigation of other theoretical models may be warranted.

Bibliography

- J. Adam, A. Héron, and G. Laval. Study of stationary plasma thrusters using two-dimensional fully kinetic simulations. *Physics of Plasmas (1994-present)*, 11(1):295–305, 2004.
- J. Adam, J. Boeuf, N. Dubuit, M. Dudeck, L. Garrigues, D. Gresillon, A. Heron, G. Hagelaar, V. Kulaev, N. Lemoine, et al. Physics, simulation and diagnostics of hall effect thrusters. *Plasma Physics and Controlled Fusion*, 50(12):124041, 2008.
- E. Ahedo, P. Martinez-Cerezo, and M. Martinez-Sanchez. One-dimensional model of the plasma flow in a hall thruster. *Physics of Plasmas*, 8(6), 2001.
- J. Bareilles, G. Hagelaar, L. Garrigues, C. Boniface, J. Boeuf, and N. Gascon. Critical assessment of a two-dimensional hybrid hall thruster model: Comparisons with experiments. *Physics of Plasmas (1994-present)*, 11(6):3035–3046, 2004.
- S. Barral, K. Makowski, Z. Peradzyński, N. Gascon, and M. Dudeck. Wall material effects in stationary plasma thrusters. ii. near-wall and in-wall conductivity. *Physics of Plasmas (1994-present)*, 10(10):4137–4152, 2003.
- J. Beall, Y. Kim, and E. Powers. Estimation of wavenumber and frequency spectra using fixed probe pairs. *Journal of Applied Physics*, 53(6):3933–3940, 1982.
- C. K. Birdsall and B. A. Langdon. *Plasma Physics via Computer Simulation*. Taylor & Francis Group, 2005.
- J. A. Bittencourt. *Fundamentals of Plasma Physics*. Springer, 3rd edition, 2004.

- J. Boeuf and L. Garrigues. Low frequency oscillations in a stationary plasma thruster. *Journal of Applied Physics*, 84(7):3541–3554, 1998.
- A. Bouchoule, J. Boeuf, A. Heron, and O. Duchemin. Physical investigations and developments of hall plasma thrusters. *Plasma Physics and Controlled Fusion*, 46(12B):B407, 2004.
- A. I. Bugrova, A. V. Desyatkov, and A. I. Morozov. *Sov. J. Plasma Phys*, 18, 1992.
- O. Buneman. Dissipation of currents in ionized media. *Physical Review*, 115(3):503, 1959.
- E. Cha. *Dynamic Models of Electron Transport in Hall Thruster Simulations*. PhD thesis, Stanford University, August 2015.
- E. Cha, M. Cappelli, and E. Fernandez. Hybrid simulations of hall thrusters operating on various propellants. In *31st International Electric Propulsion Conference*, pages 2009–075, 2009.
- E. Cha, M. A. Cappelli, and E. Fernandez. Implementation of an entropy closure model for 2-d hybrid hall thruster simulations. *IEEE Transactions of Plasma Science*, 43(1), 2015.
- E. Y. Choueiri. A critical history of electric propulsion: The first 50 years (1906-1956). *Journal of Propulsion and Power*, 20(2):193–203, 2004.
- E. Choueiri. Plasma oscillations in hall thrusters. *Physics of Plasmas*, 8, 2001.
- J. M. Dawson. One-dimensional plasma model. *Physics of Fluids*, 5:445–459, 1962.
- J. M. Dawson. Particle simulation of plasmas. *Reviews of modern physics*, 55(2):403, 1983.
- J. V. Dugan and R. J. Sovie. Volume ion production costs in tenuous plasmas: A general atom theory and detailed results for helium, argon and cesium. Technical Report D-4150, NASA, 1967.
- C. Ellison, Y. Raitses, and N. Fisch. Cross-field electron transport induced by a rotating spoke in a cylindrical hall thruster. *Physics of Plasmas*, 19(1):013503, 2012.

- E. Fernandez, M. A. Cappelli, and K. Mahesh. 2d simulations of hall thrusters. *Center for Turbulence Research, Annual Research Briefs, Stanford University*, pages 81–90, 1998.
- E. Fernandez, A. Knoll, and M. Cappelli. A two-dimensional (z - θ) fluid/pic simulation of coaxial hall thrusters. 2005.
- J. M. Fife. Two-dimensional hybrid particle-in-cell modeling of hall thrusters. Master's thesis, Massachusetts Institute of Technology, May 1995.
- J. M. Fife. *Hybrid-PIC modeling and electrostatic probe survey of Hall thrusters*. PhD thesis, Massachusetts Institute of Technology, 1999.
- C. A. J. Fletcher. *Computational Techniques for Fluid Dynamics*, volume 1. Springer-Verlag, New York, NY, USA, 2 edition, 1991.
- W. Frias, A. I. Smolyakov, I. D. Kaganovich, and Y. Raitses. Long wavelength gradient drift instability in hall plasma devices. i. fluid theory. *Physics of Plasmas*, 19(7):072112, 2012.
- L. Garrigues and P. Coche. A two-dimensional (azimuthal-axial) particle-in-cell of a hall thruster. In *Proceedings of 33rd International Electric Propulsion Conference*, 2013.
- N. Gascon and M. Cappelli. Plasma instabilities in the ionization regime of a hall thruster. In *Proceedings of the 39th Joint Propulsion Conference (American Institute of Aeronautics and Astronautics, 2003)*, AIAA-2003-4857, 2003.
- N. Gascon, M. Dudeck, and S. Barral. Wall material effects in stationary plasma thrusters. i. parametric studies of an spt-100. *Physics of Plasmas (1994-present)*, 10(10):4123–4136, 2003.
- D. M. Goebel and I. Katz. *Fundamentals of Electric Propulsion: Ion and Hall Thrusters*. Jet Propulsion Laboratory, California Institute of Technology, 2008.
- G. Hagelaar, J. Bareilles, L. Garrigues, and J.-P. Boeuf. Two-dimensional model of a stationary plasma thruster. *Journal of Applied Physics*, 91(9):5592–5598, 2002.

- W. A. Hargus. *Investigation of the plasma acceleration mechanism within a coaxial Hall thruster*. PhD thesis, Stanford University, 2001.
- C. Hirsch. *Numerical Computation of Internal and External Flows*, volume 1. John Wiley & Sons, 1988.
- R. R. Hofer, I. Katz, I. G. Mikellides, and M. Gamero-Castano. Heavy particle velocity and electron mobility modeling in hybrid-pic hall thruster simulations. In *Proceedings of 42nd Joint Propulsion Conference*, volume 4658, pages 9–12, Sacramento, CA, July 2006.
- R. R. Hofer, I. Katz, I. G. Mikellides, and M. Gamero-Castano. Hybrid-pic computer simulation of the plasma and erosion processes in hall thrusters. 2010.
- G. S. Janes and R. S. Lowder. Anomalous electron diffusion and ion acceleration in a low-density plasma. *Physics of Fluids*, 9(6):1115–1123, 1966.
- A. Kapulkin and M. M. Guelman. Low-frequency instability in near-anode region of hall thruster. *Plasma Science, IEEE Transactions on*, 36(5):2082–2087, 2008.
- A. K. Knoll. *Plasma Oscillations and Associated Electron Transport within Hall Thrusters*. PhD thesis, Stanford University, 2010.
- J. W. Koo and I. D. Boyd. Computational model of a hall thruster. *Computer Physics Communications*, 164(1):442–447, 2004.
- C. M. Lam, A. K. Knoll, M. A. Cappelli, and E. Fernandez. Two-dimensional (z - θ) simulations of hall thruster anomalous transport. In *Proceedings of the 31st International Electric Propulsion Conference*, 2009.
- C. A. Lentz. Transient one dimensional numerical simulation of hall thrusters. Master's thesis, Massachusetts Institute of Technology, 1990.
- D. Mathur and C. Badrinathan. Ionization of xenon by electrons: Partial cross sections for single, double, and triple ionization. *Physical Review A*, 35(3):1033–1042, Feb 1987.

- K. Matyash, R. Schneider, S. Mazouffre, S. Tsikata, Y. Raitses, and A. Diallo. 3d simulation of the rotating spoke in a hall thruster. In *33rd International Electric Propulsion Conference*, 2013.
- N. B. Meezan. *Electron transport in a coaxial Hall discharge*. PhD thesis, Stanford University, 2002.
- N. B. Meezan, W. A. Hargus, and M. A. Cappelli. Anomalous electron mobility in a coaxial hall discharge plasma. *Physical Review*, 63(2):026410, 2001.
- P. Moin. *Fundamentals of Engineering Numerical Analysis*. Cambridge University Press, 2001.
- A. Morozov and V. Savelyev. Fundamentals of stationary plasma thruster theory. In *Reviews of Plasma Physics*, pages 203–391. Springer, 2000.
- A. I. Morozov. *J. Appl. Mech. Tech. Phys* [originally in Russian, in *Zh. Prikl. Mekh. Tekh. Fiz.*], 9, 1968.
- N. Oudini, F. Taccogna, and P. Minelli. 3d fully kinetic simulation of near-field plume region. 2013.
- F. Parra, E. Ahedo, J. Fife, and M. Martinez-Sanchez. A two-dimensional hybrid model of the hall thruster discharge. *Journal of Applied Physics*, 100(2):023304, 2006.
- D. Rapp and P. Englander-Golden. Total cross sections for ionization and attachment in gases by electron impact. i. positive ionization. *Journal of Chemical Physics*, 43(5): 1464–1479, 1965.
- M. K. Scharfe. *Electron Cross Field Transport in Radial-Axial Hybrid Hall Thruster Simulations*. PhD thesis, Stanford University, May 2009.
- M. K. Scharfe, N. Gascon, M. A. Cappelli, and E. Fernandez. Comparison of hybrid hall thruster model to experimental measurements. *Physics of Plasmas*, 13, 2006.

- M. K. Scharfe, C. A. Thomas, D. B. Scharfe, N. Gascon, M. A. Cappelli, and E. Fernandez. Shear-based model for electron transport in hybrid hall thruster simulations. *Plasma Science, IEEE Transactions on*, 36(5):2058–2068, 2008.
- E. V. Shikin and A. I. Plis. *Handbook on Splines for the User*. CRC Press, 1995.
- A. W. Smith and M. A. Cappelli. Time and space-correlated plasma potential measurements in the near field of a coaxial hall plasma discharge. *Physics of Plasmas (1994-present)*, 16(7):073504, 2009.
- E. Sommier, M. K. Scharfe, N. Gascon, M. A. Cappelli, and E. Fernandez. Simulating plasma-induced hall thruster wall erosion with a two-dimensional hybrid model. *Plasma Science, IEEE Transactions on*, 35(5):1379–1387, 2007.
- D. Sydorenko, A. Smolyakov, I. Kaganovich, and Y. Raitses. Plasma-sheath instability in hall thrusters due to periodic modulation of the energy of secondary electrons in cyclotron motion. *Physics of Plasmas (1994-present)*, 15(5):053506, 2008.
- F. Taccogna, P. Minelli, and N. Oudini. Physics of hall-effect discharge by particle. In *Proceedings of 33rd International Electric Propulsion Conference*, 2013.
- C. A. Thomas. *Anomalous Electron Transport in the Hall-Effect Thruster*. PhD thesis, Stanford University, 2006.
- W. G. Vicenti and C. H. Kruger. *Introduction to Physical Gas Dynamics*. Krieger Publishing Company, 1965.
- S. Yoshikawa and D. J. Rose. Anomalous diffusion of a plasma across a magnetic field. *Physics of Fluids*, 5(3):334–340, 1962.